Wave Dynamics of the Stratosphere and Mesosphere

Moss, Andrew

Award date:
2017

Awarding institution:
University of Bath

Wave Dynamics of the Stratosphere and Mesosphere

submitted by

Andrew Moss

for the degree of Doctor of Philosophy

University of Bath

Department of Electronic and Electrical Engineering

April 2016

Abstract

Gravity waves play a fundamental role in driving the large-scale circulation of the atmosphere. They are influenced both by the variation in their sources and the filtering effects of the winds they encounter as they ascend through the atmosphere. In this thesis we present new evidence that gravity waves play a key role in coupling the troposphere, stratosphere and mesosphere. In particular, we examine the connection of gravity waves to two important large-scale oscillations that occur in the atmosphere, namely the Madden-Julian Oscillation (MJO) in the troposphere and the Mesospheric Semi-Annual Oscillation (MSAO).

We present the first ever demonstration that the MJO acts to modulate the global field of gravity waves ascending into the tropical stratosphere. We discover a significant correlation with the MJO zonal-wind anomalies and so suggest that the MJO modulates the stratospheric gravity-wave field through a critical-level wave-filtering mechanism. Strong evidence for this mechanism is provided by consideration of the winds encountered by ascending waves.

The Ascension Island meteor radar is used for the first time to measure momentum fluxes over the Island. These measurements are then used to investigate the role of gravity-wave in driving a dramatic and anomalous wind event that was observed to occur during the first westward phase of the MSAO in 2002. Gravity waves are shown to play an important role in driving this event, but the observations presented here also suggest that the current theory of the mechanism describing these anomalous mesospheric wind events is not valid.

Both of these studies highlight the critical importance of gravity waves to the dynamics of the atmosphere and highlight the need for further work to truly understand these waves, their processes and their variability.

Acknowledgements

I am very fortunate for the great experiences I have had during my time as a PhD student. These have largely resulted from the enthusiasm and encouragement of my supervisor, Nick, whose help and guidance has been invaluable throughout. I also extend my thanks to all the staff and postgraduate students I have met over this time and who have helped contribute to this experience.

I thank all those I have shared an office with, especially Corwin for all of his assistance, time and patience, and Neil, for all his help and also for making the research schools on the Isle of Arran and in Grenoble so memorable. I also thank Sarah, who has become a great friend over these past years, Lucy, for your support over the past months, and Zhongjian, for positively distracting me with so much sport.

I thank the organisations who have provided funding during my PhD studies. In particular, the U.K. National Environment Research Council for providing my PhD studentship. This has helped to support my attendance at the National Centre for Atmospheric Science research schools on the Isle of Arran and in Edinburgh, and at the European Research Course on Atmospheres in Grenoble. I extend my thanks to the fantastic work the organisers of these courses do, and to the network of friends who have made these experiences so special. In addition, I thank the Royal Meteorological Society for providing additional financial support to my studentship that helped me to participate in fieldwork on South Georgia island in January 2015.

Finally, I thank all my extended family for their support throughout my life. In particular, thank you Mum, Dad and Laura for all your encouragement, love and support, and Grandad, for some of my fondest memories; I can assure you that this is as good as can be expected under the circumstances, although I have to admit, I was never quite sure what those circumstances were.

Contents

List of Figures

List of Tables

List of Acronyms

AIM	Aeronomy of Ice in the Mesosphere
AIRS	Atmospheric InfraRed Sounder
CDAAC	COSMIC Data Analysis and Archive Center
CHAMP	Challenging Mini-Satellite Payload
CIPS	Cloud Imaging and Particle Size
CIRA-86	COSPAR International Reference Atmosphere
CLIVAR	Climate Variability and Prediction Programme (U.S.)
COSMIC	Constellation Observing System for Meteorology, Ionosphere and Climate
ECMWF	European Centre for Medium Range Weather Forecasting
EISCAT	European Incoherent Scatter Scientific Association
ENSO	El Niño Southern Oscillation
EP	Eliassen-Palm flux divergence
GOES	Geostationary Operational Environmental Satellite
GPM	Global Precipitation Measurement mission
GPS	Global Positioning System
GPS/Met	GPS Meteorology experiment
GWPE	Gravity-Wave Potential Energy
IGOR	Integrated GPS Occultation Receiver
IHC	Inter-Hemispheric Coupling
ISO	Intra-Seasonal Oscillation
HIRDLS	HIgh Resolution Dynamics Limb Sounder
JAXA	Japan Aerospace eXploration Agency
MF	Medium-Frequency radar
MLS	Microwave Limb Sounder
MLT	Mesosphere and Lower Thermosphere
MSAO	Mesospheric Semi-Annual Oscillation
MST	Mesosphere-Stratosphere-Troposphere radar
MJO	Madden Julian Oscillation
MPD	Meteor Position Data
MU	Middle and Upper atmosphere radar
NASA	National Aeronautics and Space Administration (U.S.)
NLC	Noctilucent Clouds
NOAA	National Oceanic and Atmospheric Administration (U.S.)
OLR	Outgoing Long-wave Radiation
PMC	Polar Mesospheric Clouds
PRF	Pulse Repetition Frequency

QBO	Quasi Biennial Oscillation
RO	Radio Occultation
RMM	Real-time Multivariate MJO index
SAAMER	Southern Andes Agile MEteor Radar
SABER	Sounding of the Atmosphere using Broadband Emission Radiometry
SAC-C	Satellite de Aplicaciones Cientificas-C
SG-WEX	South Georgia Wave EXperiment
SSAO	Stratospheric Semi-Annual Oscillation
ST	Stockwell Transform
TBB	Tri-Band Beacon
TIP	Tiny Ionospheric Photometer
TRMM	Tropical Rainfall Measuring Mission
TMI	TRMM Microwave Imager
UCAR	University Corporation for Atmospheric Research (U.S.)
UTC	Coordinated Universal Time
VIRS	Visible and Infra-Red Scanner instrument

List of Mathematical Symbols

α	Adjusted zenith angle
γ	Ratio of specific heats for constant pressure and volume
ρ	Atmospheric density
σ_e	Scattering cross-section of a free electron
ω	Wave frequency
ω_a	Acoustic wave frequency
Ω	Earth's rotational velocity
ϕ	Latitude or zenith angle dependent on use
θ	Azimuth angle
λ	Wavelength
A	Wave amplitude
a_{GW}	Gravity-wave acceleration
c	Gravity-wave phase speed with respect to the ground
C	Speed of sound
$\hat{c}$	Intrinsic phase speed for a gravity wave
D	Ambipolar diffusion coefficient
d	Drift distance of meteor trail
E_k	Kinetic energy

E_p	Potential energy
f	Inertial frequency
F_T	Transmitter frequency
G	Antenna gain
g	Acceleration due to gravity
H	Scale height
h	True height of meteor
K	Complex wavenumbers
k	Real wavenumbers
k_B	Boltzmann constant
m	Mean molecular mass
n_e	Electron number density
N	Brunt-Väisälä frequency
N_{ref}	Atmospheric refractivity
P_R	Received power
P_T	Transmitted power
p	Pressure
p_w	Water vapour partial pressure
q	Number of electrons per meter in meteor trail
R_i	Richardson number
R	Slant range of meteor
R_E	Earth's radius
T	Temperature
t	Time
U	Wave perturbation velocity
u	Zonal wind
u'^2	Zonal variance
$u'v'$	Vertical component of horizontal momentum flux
$u'w'$	Zonal component of vertical momentum flux
v	Meridional wind
v'^2	Meridional variance
$v'w'$	Meridional component of vertical momentum flux
v_h	Horizontal velocity
v_{rad}	Radial velocity
v_{radm}	Modelled radial velocity
w	Vertical wind
w'^2	Vertical variance
W	Liquid water content
x	Horizontal distance
z	Height

Thesis Outline

This thesis aims to further the understanding of gravity waves in the equatorial stratosphere and mesosphere. Specifically, in Chapter 3 we discuss whether the MJO modulates the fluxes of gravity waves in the equatorial stratosphere and in Chapter 4 we assess the contributions of gravity waves in the driving of anomalous events in the equatorial mesosphere. The presentation of this thesis is summarised below.

Chapter 1 introduces the predicted structure of the atmosphere under radiative equilibrium and the importance of atmospheric waves in explaining its observed structure. These waves are introduced and their influence on the dynamics of the atmosphere is discussed. Finally, the large-scale variability in the atmosphere, which can influence the generation and propagation of these waves, is discussed.

Chapter 2 introduces the observations and analysis methods used in this thesis. Both the calculation of winds and gravity-wave properties from meteor measurements, and the calculation of gravity-wave properties from radio occultation temperature profiles, are discussed. The other supporting observations used in this thesis are also presented at the end of this chapter.

In Chapter 3 we use COSMIC radio occultation temperature measurements to determine gravity-wave fluxes in the tropical stratosphere. The contribution of the MJO to these fluxes is assessed by the separation of these fluxes by MJO phase. Observations of the convective and dynamic component of the MJO are used to assess the mechanism of this modulation. The results from this chapter present the first evidence of large-scale modulation of stratospheric gravity-wave fluxes by the MJO in the tropical stratosphere.

In Chapter 4 we use meteor measurements from the Ascension Island meteor radar (8° S, 14° W) to calculate winds and gravity-wave momentum fluxes. These are the first measurements of gravity-wave momentum flux made using the Ascension Island meteor radar. These are used to assess the contribution of gravity waves to the MSAO, and in particular an anomalous westward phase event that occurred in 2002.

Chapter 5 summarises the results from this thesis, highlights the other research contributions from the author and suggests a number of future studies of interest.

Chapter 1

Introduction to the Atmosphere

This chapter provides an introduction to the theoretical and observed structure of the atmosphere. The importance of atmospheric waves in describing the observed atmospheric structure will be discussed and the wave phenomena that exist in the equatorial atmosphere will be introduced. We then introduce some of the large-scale variability in the equatorial atmosphere that is either driven by these waves, or influences the variability of their sources.

1.1 The Thermal and Dynamical Structure of the Earth's Atmosphere

1.1.1 Introduction to the Earth's Atmosphere

The Earth's atmosphere is a thin envelope of gas that surrounds the planet. It can be described by concentric layers, the vertical boundaries of which are defined by the temperature gradient as shown in Figure 1.1. Each of these concentric layers or spheres, namely the *troposphere*, *stratosphere* and *mesosphere*, are characterised by either an increasing or decreasing temperature gradient with altitude. The upper boundary of each sphere is defined as the height where the temperature gradient reverses and is known as a pause, namely the *tropopause*, *stratopause* and *mesopause*.

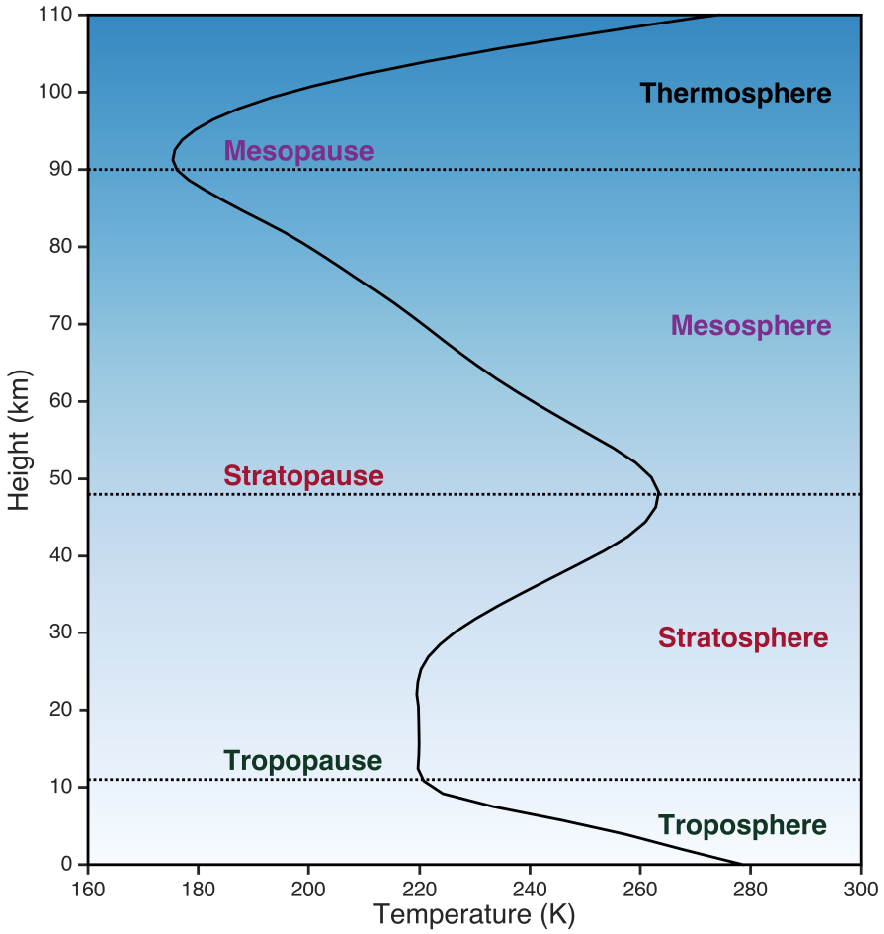

Figure 1.1: *Temperature structure of the atmosphere from the CIRA-86 model at 55° N. The figure shows a typical mid-latitude vertical temperature profile. Note the atmospheric layers, or spheres, which are characterised by their temperature gradients and have an upper boundary defined by the reversal in this gradient, known as a pause.*

The differing temperature gradients arise primarily due to the varying concentrations of different chemical species with height. These chemical species heat the local atmosphere by either absorbing radiation (e.g. the absorption of ultraviolet radiation by ozone molecules) or cool the local atmosphere through the emission of radiation (e.g. the emission of infrared radiation by carbon dioxide molecules and water vapour). The heating and cooling rates for several molecular species that exist in the atmosphere are shown in Figure 1.2.

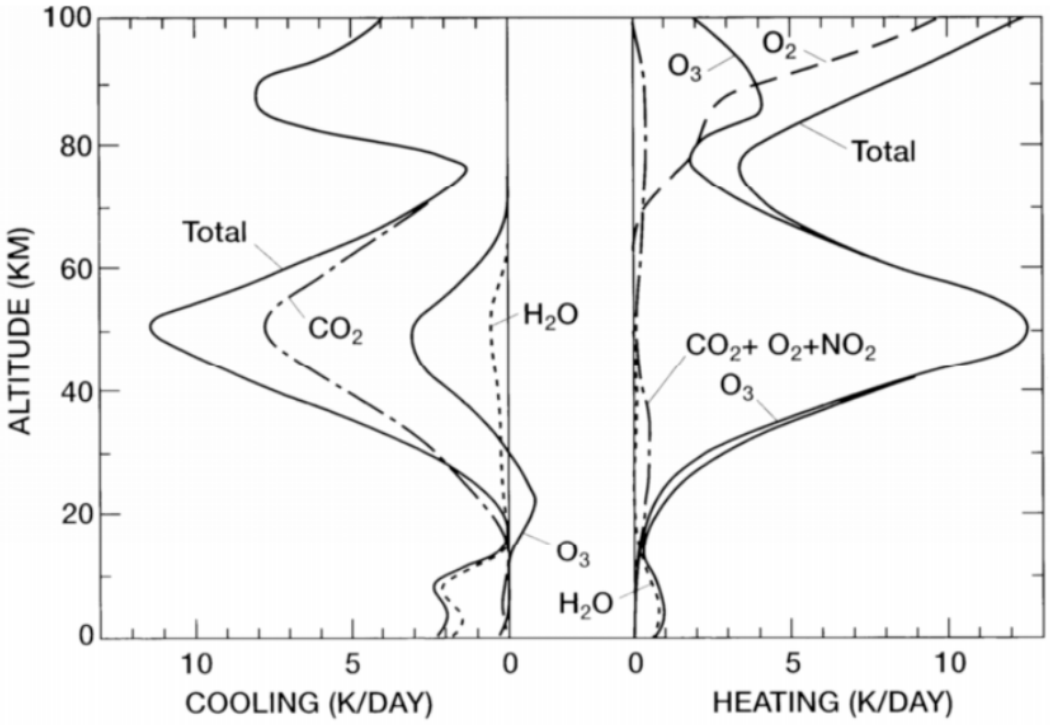

Figure 1.2: *The globally-averaged short-wave heating and long-wave cooling rates (K day^{-1}) as a function of height for the dominant chemical constituents of the atmosphere at different heights, reproduced from London (1980).*

In Figure 1.2, it can be seen that the emission of long-wave radiation by oxygen compounds dominate the heating rates above the tropopause; ozone in the stratosphere and oxygen in the thermosphere. The cooling rates above the tropopause are a result of the short-wave absorption of radiation particularly by carbon dioxide. The balance of these heating and cooling rates cause the positive temperature gradient with increasing height in the stratosphere and thermosphere, and the negative temperature gradient with increasing height in the mesosphere. The presence of water vapour in troposphere causes both cooling due to the absorption of long-wave radiation and heating due to the emission of short-wave radiation at a rate of approximately 2 K day^{-1} and 1 K day^{-1}, respectively.

The troposphere describes the region of the atmosphere from the surface to heights of around 10 km at high latitudes to around 16 km at the equator. In the troposphere, temperature decreases at a rate of approximately $\sim$7 K km^{-1} and is a result of solar radiation heating the surface of the Earth more strongly than the air above. The reversal in temperature gradient, which is the upper bound of the troposphere and named the tropopause, varies with season and latitude, and is higher in the summer and in the tropics. The troposphere contains nearly all of the water vapour in the atmosphere and is where weather occurs. Most water vapour condenses out at the tropopause due to the minimum in temperature, which can be seen by the characteristic anvil shaped cumulonimbus clouds that flatten out at the tropopause.

Between the tropopause and about 50 km lies the stratosphere. The stratosphere is a region of increasing temperature with increasing height, which reaches a local maximum at the stratopause of approximately 270 K. This positive temperature gradient is due to the absorption of ultraviolet radiation in the ozone cycle, which heats the surrounding atmosphere, as shown in Figure 1.2. The stratosphere is very dry as a consequence of the cold-point tropopause, which acts as a cold trap for moisture and strongly inhibits vertical motion, and thus mixing, as a result of the positive temperature gradient. An important and interesting dynamical feature of the stratosphere is the Quasi-Biennial Oscillation (QBO), which will be discussed in Section 1.3.

Above the stratopause lies the mesosphere, where the temperature again decreases with increasing height. At heights between approximately 50–100 km, the concentration of ozone decreases enough that cooling due to carbon dioxide begins to dominate. This temperature decrease occurs up to the mesopause, which marks the coldest point in the atmosphere and where temperatures can fall below 130 K. Above this lies the thermosphere. There the dissociation of nitrogen and oxygen molecules causes a rapid increase in temperature, which can exceed 1000 K above 120 km. The mesosphere and lower thermosphere (MLT) region contains some interesting phenomena such as polar mesospheric clouds, which occur at high latitudes around the summer solstice when the region reaches its coldest temperatures. It is also where meteoroids ablate and form meteor trails, which can be seen by the eye and are colloquially known as shooting stars. Radar measurements of meteors are one of the few possible methods of measuring the MLT region.

1.1.2 The Predicted Thermal and Dynamical Structure of the Atmosphere in Radiative Equilibrium

A simple hypothetical model of the atmosphere can be obtained by considering it to be in *radiative equilibrium*, i.e. to have no net heating or cooling. The heating and cooling rates presented in Figure 1.2 can be used to calculate the hypothetical zonal average temperature structure of the atmosphere under the conditions of radiative equilibrium. This is presented in Figure 1.3.

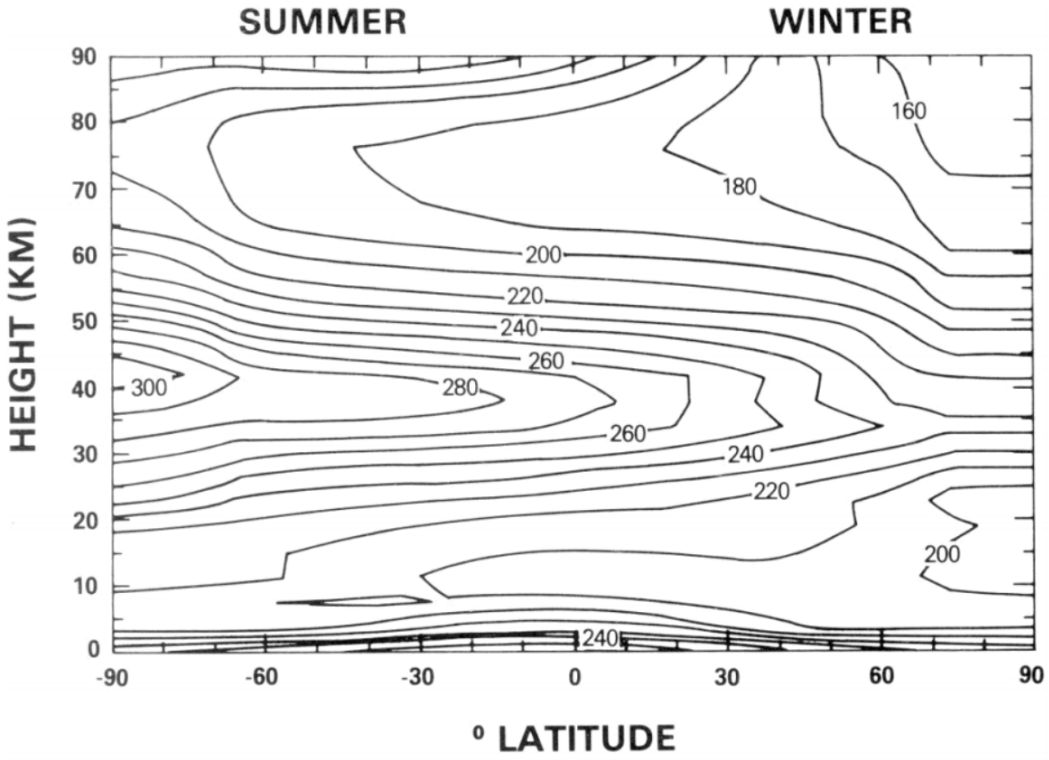

Figure 1.3: *A prediction of solstitial atmospheric zonal-mean temperature as a function of height and latitude, from Geller (1983). Note the gradient in temperature from the warmer summer pole to the cooler winter pole at all heights.*

Figure 1.3 shows the horizontal temperature gradient to be from the warmer summer pole to the cooler winter pole. This is unsurprising given the summer pole will be in continuous daylight, and thus continually heated, whereas the winter pole will be in continuous darkness. A maximum temperature of approximately 300 K is predicted to occur at a height of around 40 km due to the high concentration of ozone. At similar heights over the winter pole the temperature drops to around 220 K. The coldest temperatures of less than 160 K are predicted to occur in the winter mesosphere, at heights above 70 km.

The structure of large-scale zonal winds that are predicted under radiative equilibrium can be deduced from consideration of the forces acting on an air parcel and the *thermal wind equation*, which describes the influence a horizontal temperature gradient has on the vertical structure of the wind. The meridional temperature gradient that results from differential heating at the poles causes high pressure at the summer pole and low pressure at the winter pole. This meridional pressure gradient initiates an atmospheric flow towards the winter pole. As the Earth is a rotating system, moving air parcels will experience a *Coriolis force*, which acts perpendicular to the direction of the air parcel's motion. The balance between the Coriolis and *pressure-gradient force* results in a steady-state zonal circulation, the *geostrophic wind*, as illustrated by Figure 1.4.

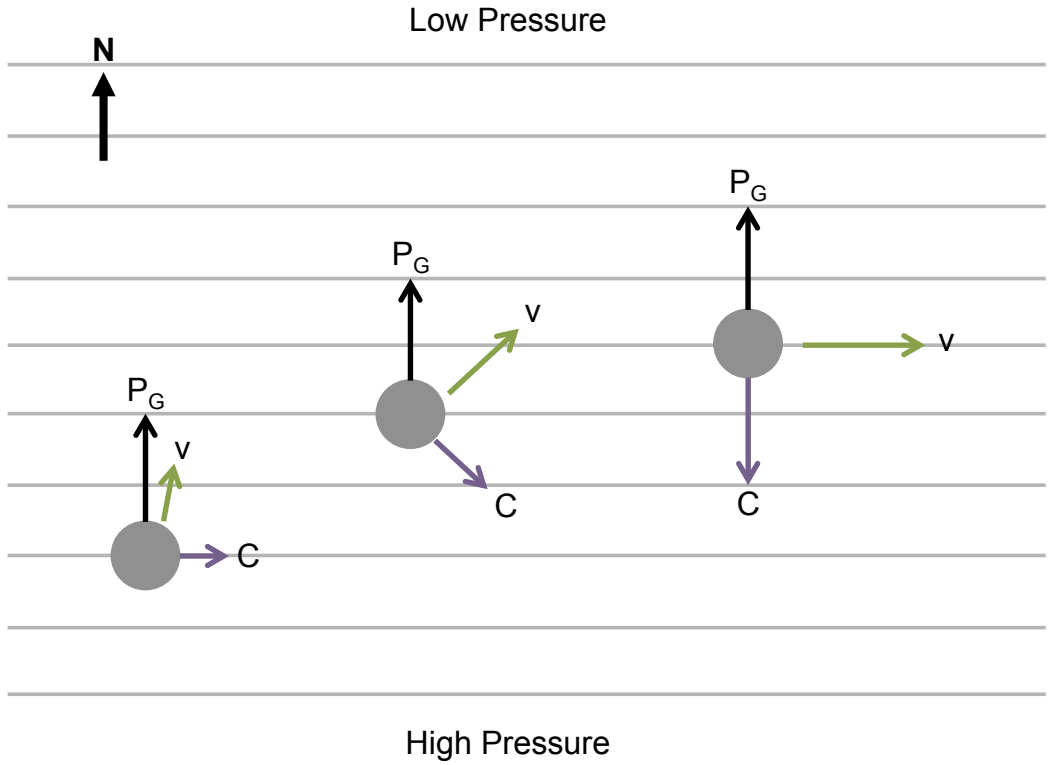

Figure 1.4: *A schematic diagram illustrating the geostrophic balance of forces on an air parcel in the northern winter hemisphere. The thin horizontal grey lines are isobars (contours of constant pressure). An air parcel moving northward under a north-south pressure gradient force, P_G (black), will experience a force, perpendicular to its motion, due to the Coriolis force, C (purple). This adds a zonal component to the air parcels velocity, v (green), which increases. The increase in velocity increases the Coriolis force, which always acts perpendicular to the motion of the air parcel, and thus rotates. Consequently, we achieve purely zonal motion, the geostrophic wind, where the pressure-gradient and Coriolis forces are balanced.*

The Coriolis force acts to push poleward flow to the right in the northern hemisphere

and to the left in the southern hemisphere. The resulting geostrophic winds are thus eastward in the winter hemisphere and westward in the summer hemisphere. The horizontal temperature gradient creates a vertical wind shear through the thermal wind equation. The radiative equilibrium temperature structure (Figure 1.3) and the thermal wind equation, result in the geostrophic winds presented in Figure 1.5. Note that it is not possible to calculate the geostrophic winds at the equator since the Coriolis force tends to zero and thus geostrophic balance does not apply.

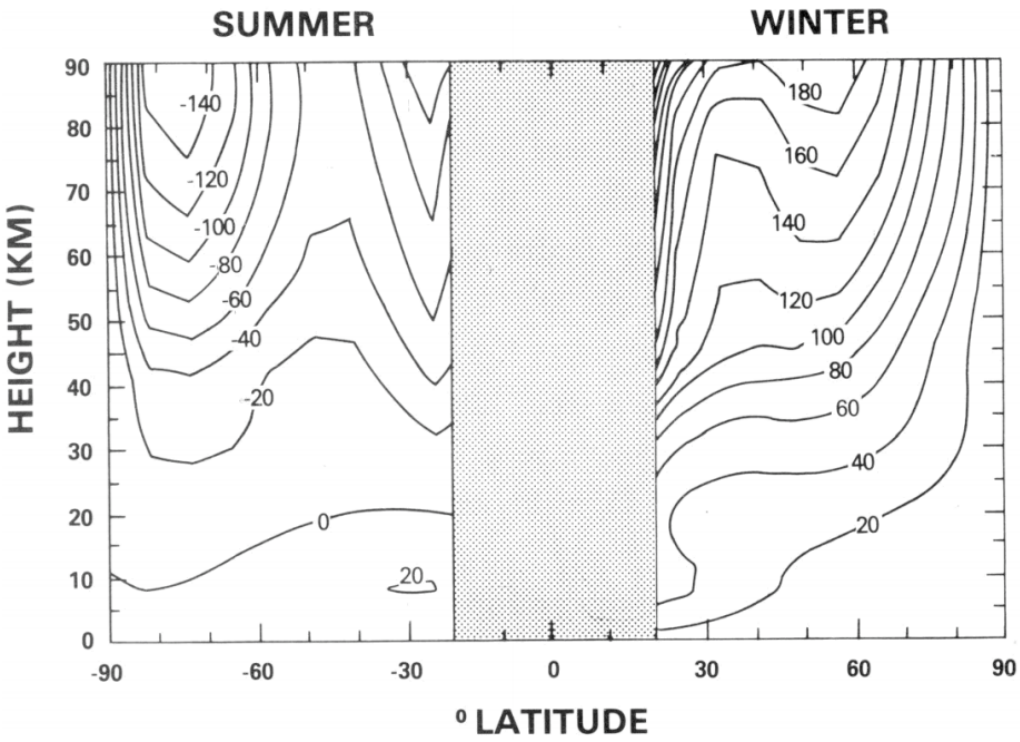

Figure 1.5: *A prediction of solstitial atmospheric zonal-mean wind (ms^{-1}) as a function of height and latitude. Eastward winds are given by positive values and westward winds are given by negative values. No predictions are made at the equator due to the near-zero Coriolis force. Reproduced from Geller (1983).*

The zonal winds presented in Figure 1.5 are stronger with increasing height. Two open zonal jets occur, where wind speeds increase with height, which are centred at high latitudes in the summer hemisphere and mid-latitudes in the winter hemisphere, and reach speeds of up to 180 ms^{-1} in the winter mesosphere. Critically, under the conditions of pure radiative equilibrium considered thus far, no vertical or meridional flows are predicted.

The key properties of the atmosphere in a hypothetical state of pure radiative equilibrium are summarised below.

1. Horizontal temperature gradient from the warmer summer pole to the cooler winter pole.

2. Zonal winds increase with height.

3. Two open zonal jets are present at high latitudes in the summer hemisphere and mid-latitudes in the winter hemisphere.

4. No vertical or meridional flow.

We will now consider how the observed atmospheric structure compares to the simple radiative equilibrium model.

1.1.3 The Observed Thermal and Dynamical Structure of the Atmosphere

The Earth's atmosphere is actually observed to be very different to that predicted by the radiative equilibrium model considered in Section 1.1.2. Figures 1.6 and 1.7 present more realistic representations of zonal-mean temperature and zonal-mean wind as a function of latitude and height for both northern and southern hemisphere summer solstice conditions, using the COSPAR International Reference Atmosphere (CIRA-86). The CIRA-86 model provides global climatologies of zonal-mean winds and temperatures up to 120 km derived from combined ground-based and satellite-borne measurements, and accurately reproduces the characteristic features of the atmosphere (Fleming et al., 1990).

The radiative equilibrium model zonal-mean temperatures shown in Figure 1.3 compare well with the temperatures observed in CIRA-86 (Figure 1.6) in the stratosphere, but elsewhere there are major differences. Firstly, the summer mesopause is much colder than the winter mesopause. This reversal in temperature gradient in the real atmosphere is the opposite of what is predicted by the radiative equilibrium model. Secondly, in the real atmosphere there is a temperature minimum at the equatorial tropopause. This is at odds with the radiative equilibrium model, which predicts a gradual increase in temperature from the winter to summer pole.

Significant differences between zonal-mean winds from the radiative equilibrium model (Figure 1.5) and the real atmosphere (Figure 1.7) are also apparent. Two pairs of zonal jets are observed up to heights of 90 km. The lower pair of jets, which occur

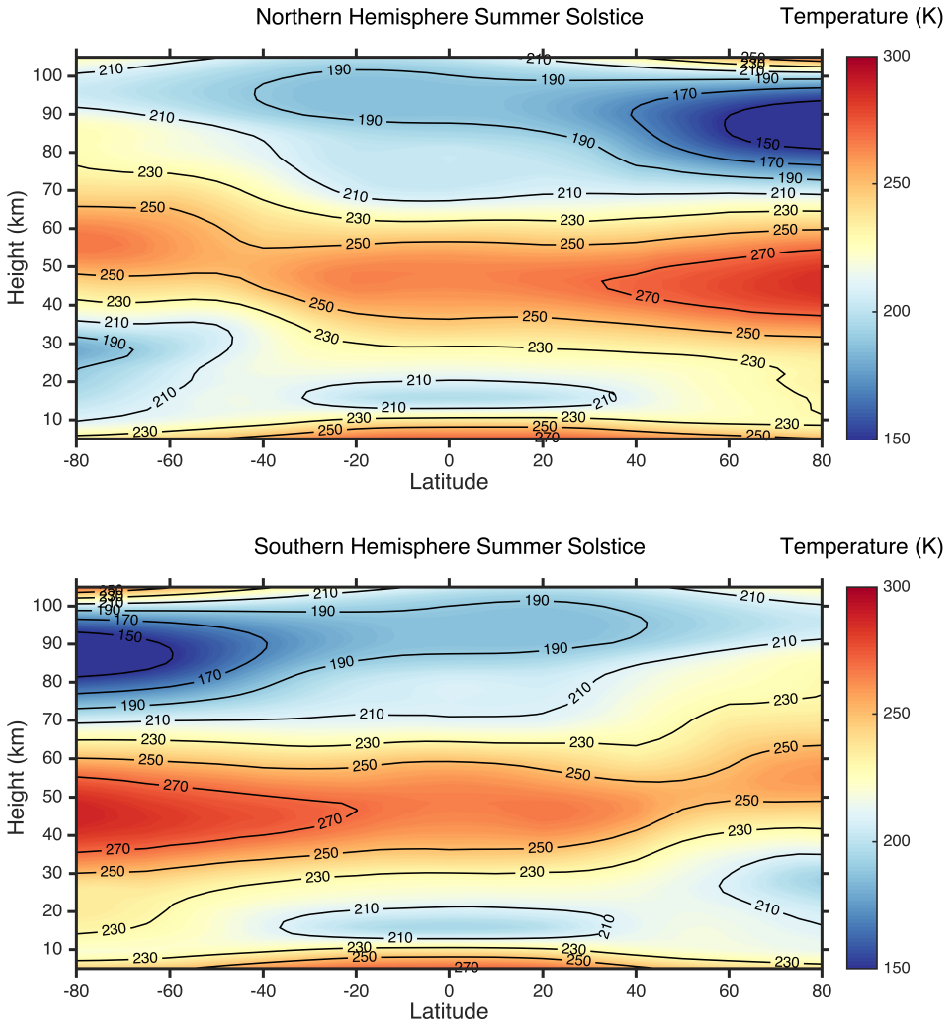

Figure 1.6: *Zonal-mean temperature from CIRA-86 as a function of latitude and height during the northern (top) and southern (bottom) hemisphere summer solstice. Note that the mesopause is much colder near the summer pole than the winter pole. Contours are in 20 K intervals.*

in the upper troposphere and are eastward in both hemispheres, were not observed in the radiative equilibrium model. An upper pair of jets are observed in the stratosphere/mesosphere and are eastward in the winter hemisphere and westward in the summer hemisphere. While these jets are observed in the radiative equilibrium model, the mesospheric jets in the real atmosphere are closed, i.e. decrease in strength with height, and actually reverse in direction at heights of approximately 90 km. This is in contrast to the radiative equilibrium predictions, where the winds continue to increase with height. The wind speeds of the jets observed in the real atmosphere are also slower than those in the radiative equilibrium model, reaching magnitudes of order 100 ms^{-1} as opposed to 180 ms^{-1}.

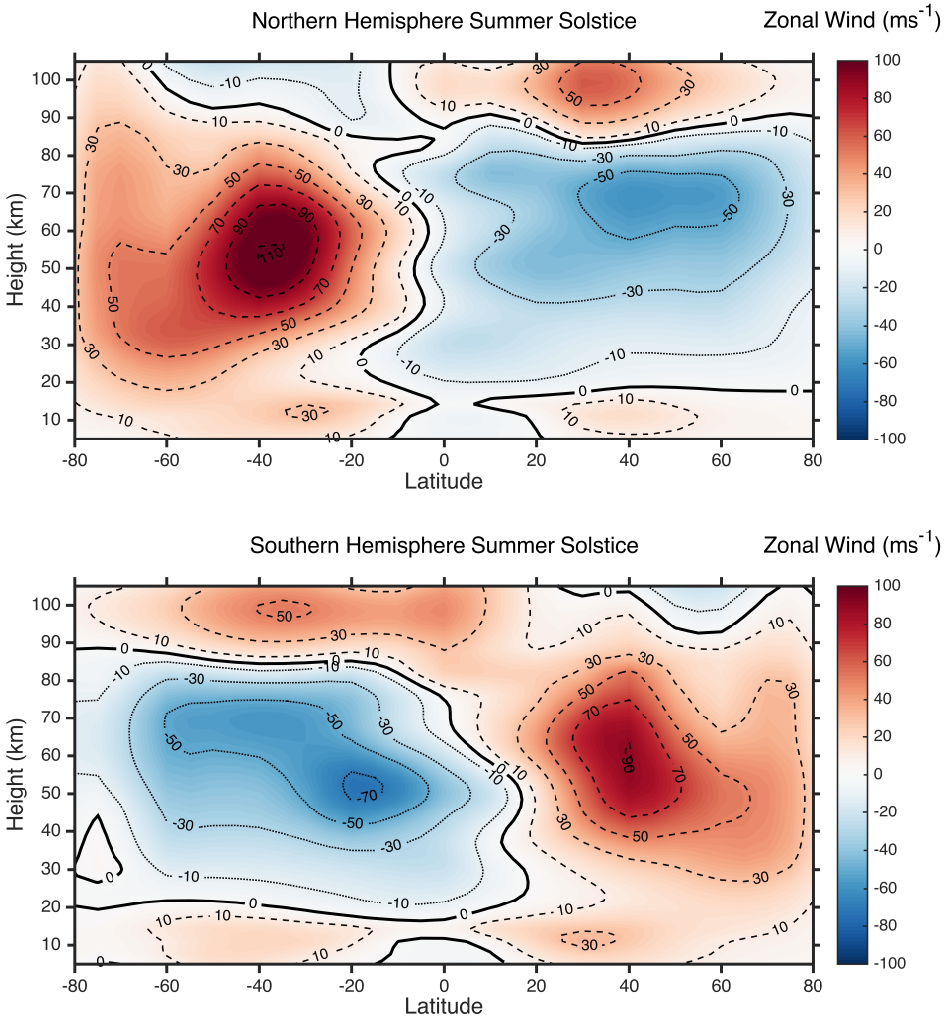

Figure 1.7: *Zonal-mean winds from CIRA-86 as a function of latitude and height during the northern (top) and southern (bottom) hemisphere summer solstice. The thick black line represents the zero-wind line, and eastward (dashed) and westward (dotted) wind contours are in 20 ms^{-1} intervals.*

The observed atmosphere is thus much more complex than that described by radiative equilibrium. This added complexity arises from additional forces, which act in an opposite direction to an air parcel's motion, as shown in Figure 1.8. In the troposphere, this force results mainly from friction due to topography, but in the stratosphere and particularly the mesosphere, this force results from the body force acting on the atmosphere due to the horizontal momentum deposition of breaking atmospheric waves.

The addition of a drag force, D, which opposes the air parcel's motion, now, with the Coriolis force, balances the pressure-gradient force. This allows a meridional component of the flow to develop, such that the wind is no longer parallel to the

isobars (contours of constant pressure), as presented in Figure 1.8. We should note that the name "drag force" is actually a misnomer, as the momentum deposited in the atmosphere by breaking waves does not necessarily apply a force that opposes the motion of the mean-flow (e.g. Fritts and Alexander, 2003). This is demonstrated in the zonal wind reversal at approximately 90 km in Figure 1.7, the momentum deposition by breaking waves actually acts to accelerate the mean-flow to large values in the opposite direction, whereas a true drag force would have actually acted to slow the mean-flow to a stationary state.

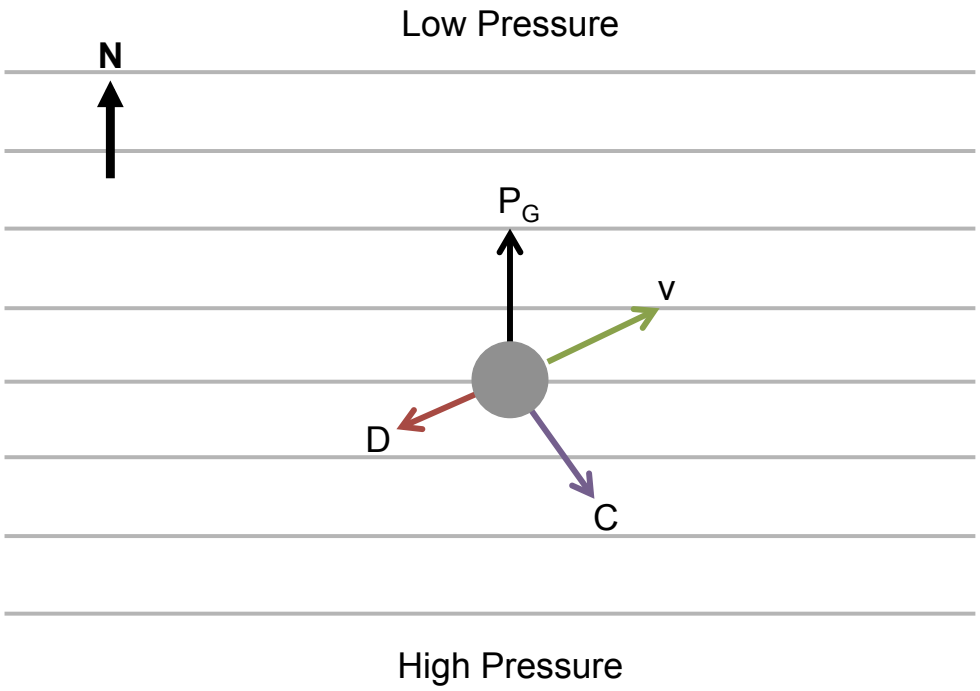

Figure 1.8: *A schematic diagram illustrating the addition of a drag force, D, to the geostrophic case shown in Figure 1.4, which acts on an air parcel in an opposite direction to its motion. This force, which allows meridional flow, results from topography in the troposphere and from the body force acting on the atmosphere as a result of the deposition of horizontal momentum in the stratosphere and mesosphere by breaking atmospheric waves.*

Figures 1.4 and 1.8 show that atmospheric winds will tend to flow from high pressure to low pressure. This flow results in a divergence and convergence of air over the summer and winter poles, respectively. To maintain continuity, this requires a circulation that replaces the air lost at the summer pole and removes air from the winter pole. This is achieved by vertical motion, whereby air is drawn up over the summer pole and dragged down over the winter pole, as shown in Figure 1.9. This circulation is known as the *Brewer-Dobson circulation.*

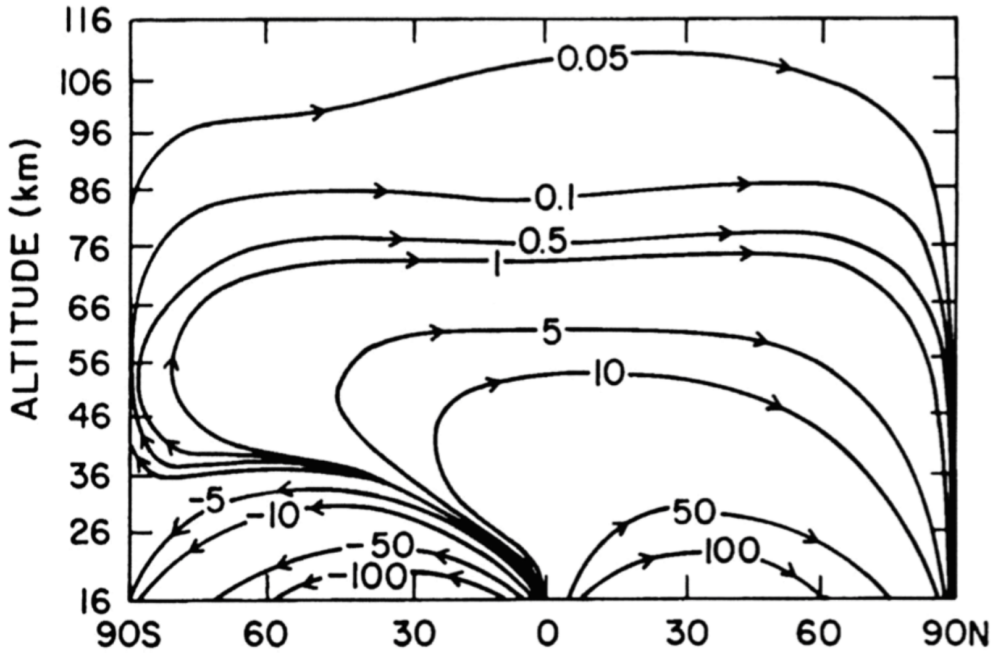

Figure 1.9: *Schematic diagram of the Brewer-Dobson circulation. The figure presents the mass meridional stream function ($kgm^{-1}s^{-1}$) for the northern hemisphere winter solstice. The summer pole upwelling results in the cold summer mesopause caused by adiabatic cooling. Reproduced from Garcia and Solomon (1983).*

The cold summer mesopause is thus explained by the adiabatic cooling of rising air over the summer pole, while sinking air over the winter pole is heated adiabatically. The resulting reversal of the temperature gradient impacts the thermal wind equation, which results in the closing of the jets around the mesopause.

The key differences between the observed atmosphere and the atmosphere in pure radiative equilibrium are summarised below.

1. The summer mesopause ($\sim$ 150 K) is much colder than the winter mesopause ($\sim$ 210 K), whereas the radiative equilibrium model predicted a warmer summer mesopause ($\sim$ 200 K) compared to the winter mesopause ($\sim$ 160 K).

2. The zonal jets in the stratosphere/mesosphere are closed around 90 km and are overall slower, with peak amplitudes of approximately 100 ms^{-1} compared to approximately 180 ms^{-1} in the radiative equilibrium predictions .

3. Meridional flow is observed and is measured to have an order of magnitude of 10 ms^{-1}.

4. Vertical motions of approximately a few cms^{-1} are inferred.

1.1.4 Summary

This section has presented the atmosphere to be organised in layers that are defined by the temperature structure. A simple hypothetical model of the atmosphere under radiative equilibrium conditions was considered and was found to differ significantly to the observed atmosphere. These differences are explained by an additional force, which is provided by the momentum deposition of breaking waves and allows meridional flow. The atmospheric waves that provide this additional force are the subject of the following section.

1.2 Atmospheric Waves

1.2.1 Introduction to Atmospheric Waves

Waves are ubiquitous throughout the atmosphere and the structure of the atmosphere is strongly influenced by the force they exert when they break. They occur on a large range of spatial and temporal scales. These wave phenomena include global-scale oscillations, such as *planetary waves*, which are coherent around a circle of latitude and have periods of a few days to a few weeks, and *atmospheric tides*, which are mostly generated through the solar heating of chemical species and have periods related to the solar day. Another important wave phenomena in the atmosphere are *gravity waves*, which exist on smaller spatial scales and typically have periods of order hours.

These wave phenomena are responsible for the driving of a number of large-scale features of the atmospheres dynamics. We will now introduce these waves, and in particular gravity waves, which are the main focus of this thesis.

1.2.2 Wave Growth in the Atmosphere

The dynamics of the atmosphere can be described as a mean flow on which are superimposed smaller scale perturbations. These perturbations include tides, planetary waves and gravity waves. As waves ascend in the atmosphere they increase in amplitude as a result of the exponential decrease in density with height. This results in wave amplitudes of order of a few ms^{-1} in the stratosphere and of tens of ms^{-1} in the MLT region, where they dominate the dynamics.

This increase in amplitude with height, z, as a result of the exponential decrease of density, ρ, is described by Equation 1.1, where H is the scale height, and ρ_0 is the atmospheric density at sea level.

$$\rho = \rho_0 \, e^{\frac{-z}{H}} \tag{1.1}$$

The *scale height* is the distance over which pressure deceases by a factor of e and is given by $H = \frac{k_B T}{mg}$, where k_B is the Boltzmann constant, T is the temperature, m is the mean molecular mass, and g is the acceleration due to gravity. The scale height is typically between 7–8 km in the lowest 100 km of the Earth's atmosphere.

The atmosphere supports waves that can propagate both horizontally and vertically. This contrasts, for example, to the waves that occur on the ocean surface, which are trapped at the sharp discontinuity in density and are thus *evanescent* (non-propagating) in the vertical. In the atmosphere, as waves propagate vertically they increase in amplitude, A, to conserve the kinetic energy per unit volume, E_k, as shown in Equation 1.2.

$$E_k = \frac{1}{2}\rho A^2 \tag{1.2}$$

Equations 1.1 and 1.2 imply an exponential increase in wave amplitude with increasing height, such that

$$A = A_0 \, e^{\frac{z}{2H}} \tag{1.3}$$

where A_0 is the amplitude at the source. While this exponential growth in wave amplitude is limited by instability, waves do reach large amplitudes as they ascend. This results in amplitudes of order of a few ms^{-1} in the stratosphere and of tens of ms^{-1} in the MLT region.

1.2.3 Internal Atmospheric Gravity Waves

1.2.3.1 Introduction to Internal Atmospheric Gravity Waves

Internal atmospheric gravity waves, more commonly known as just gravity waves, play an important role in vertical transport of energy and momentum in the atmosphere (e.g. Fritts and Alexander, 2003; Alexander et al., 2010). In particular, this transport of energy and momentum acts to close the mid-latitude zonal jets, force a pole-to-pole meridional circulation and reverse the solstitial meridional temperature gradients, such that the summer polar mesosphere is the coldest place on Earth, and drives a number of planetary-scale oscillations such as the quasi-biennial oscillation (QBO) (e.g. Lindzen, 1981; Holton, 1983; Baldwin et al., 2001; Fritts and Alexander, 2003). Gravity waves can also be observed visually in phenomena such as lenticular clouds as presented in Figure 1.10. The observed wave-like stack of clouds are a result of the temperature fluctuations from atmospheric gravity waves generated by the strong winds flowing over the mountains below. They can also be observed in a

number of other atmospheric phenomena, such as polar mesospheric clouds (known as noctilucent clouds when viewed from the ground), which are visible in the mesosphere close to the summer solstices.

Figure 1.10: *Lenticular clouds over South Georgia island. The image was taken by the author from the British Antarctic Survey King Edward Point research station in January 2015, on a fieldwork campaign to study gravity waves in the vicinity of the island using radiosondes.*

Observations of gravity waves are important for the accuracy of numerical weather prediction and global climate models. However, gravity waves are poorly represented in these models due to their small spatial scales, which are sub-grid scale. As a result gravity waves are parameterised in these models and their accurate representation thus relies on accurate observations of the momentum flux associated with these waves, their intermittency and their origins (Alexander et al., 2010).

Gravity waves first appeared in the literature during the nineteenth century but their importance for the middle atmosphere only started to be recognised following the classic paper by Hines (1960), which showed that wave-like disturbances in the middle and upper atmosphere could be described primarily by internal atmospheric gravity waves. The understanding that the amplitude of the waves would grow exponentially with height suggested that the wave sources would be located much lower in the atmosphere where the waves would be less prominent. A large increase in the number of gravity-wave studies, both observational and theoretical, in the following years exposed the importance of gravity waves to many phenomena in the atmosphere (Hines, 1972).

A surrealist representation of gravity waves, taken from Hines (1974), is shown in Figure 1.11. The figure, while very simplified, visually represents the ubiquitous and complex nature of atmospheric gravity waves, which as shown, occur on a broad range of scales. For example, the figure shows that the waves are generated mostly from the lowest part of the atmosphere, although some generation is possible at greater heights. The increase in wave amplitude with increasing height and the broad nature of the vertical and horizontal scales of waves can be seen. The figure also captures the thinning out of the wave field, as the waves dissipate at different heights as they ascend.

Studies of gravity waves have been undertaken in the past decades utilising a wide variety of observational techniques (e.g. see reviews of McLandress, 1998; Fritts and Alexander, 2003; Alexander et al., 2010). In situ observations have provided information on the seasonal variability in stratospheric gravity-wave activity using rocket soundings (e.g. Eckermann et al., 1995) and radiosonde observations (e.g. Moffat-Griffin et al., 2011, 2013). Super-pressure balloons have also been used to study gravity-wave properties in the polar regions (Vincent et al., 2007) and around Antarctica (Hertzog et al., 2008). However, the majority of observations from the middle atmosphere are from both ground-based and space-borne remote sensing instruments.

Ground-based techniques have been used to study gravity waves throughout the at-

Figure 1.11: *A surrealistic representation of atmospheric gravity waves, reproduced from Hines (1974).*

mosphere. These techniques include observations made by lidar (e.g. Mitchell et al., 1994; Hertzog et al., 2001; Rauthe et al., 2006; Lu et al., 2009; Bossert et al., 2014; Gong et al., 2015; Baumgarten et al., 2015) and optical imagers (e.g. Gardner et al., 1999; Hecht et al., 2004; Espy et al., 2006; Takahashi et al., 2009; Suzuki et al., 2013; Xu et al., 2015). In addition, radar observations have been used for a number of gravity-wave studies. This has included the use of Medium-Frequency (MF) radars (e.g. Manson and Meek, 1988; Nakamura et al., 1996; Manson et al., 1998; Hibbins et al., 2007; Rao et al., 2011; Wilms et al., 2013; Kinoshita et al., 2015), Mesosphere-Stratosphere-Troposphere (MST) radars (e.g. Riggin et al., 1997; Vaughan and Worthington, 2007; Ratnam et al., 2008a; Das et al., 2012; Sato et al., 2014) and the Middle and Upper atmosphere (MU) radar (e.g. Sato et al., 1997; Dhaka et al., 2003; Lue et al., 2013; Tsuda, 2014). Further studies have also used observations from incoherent scatter radars, such as the European Incoherent Scatter Scientific Association (EISCAT) systems, to measure gravity waves (e.g. Williams et al., 1988; Mitchell and Howells, 1998; Vlasov et al., 2011; Nygrén et al., 2015). A new EISCAT_3D incoherent scatter radar system is currently under development, which when realised, will provide an exciting opportunity to make high-resolution measurements of gravity waves

in the MLT region (McCrea et al., 2015). The production of a new generation of commercially produced meteor radars (i.e. Genesis Software and ATRAD) combined with the development of a new analysis technique has also made it possible to measure gravity waves using the global-network of meteor radar systems (Hocking, 2005). This technique has been used to observe gravity-wave properties in the mesosphere at a number of sites across the globe (e.g. Hocking, 2005; Antonita et al., 2008; Fritts et al., 2010, 2012; Andrioli et al., 2013a,b, 2015; de Wit et al., 2014, 2016; Andrioli et al., 2015; Placke et al., 2015; Moss et al., 2016a).

Improvements in the resolution of both space-borne limb and nadir sounding instruments on board satellites have helped to develop a greater understanding of the global distribution of gravity-wave variability (e.g. Fritts and Alexander, 2003; Alexander et al., 2010, and references therein). For example, nadir-sounding instruments such as the Atmospheric InfraRed Sounder (AIRS) have been used for observations of stratospheric gravity waves (e.g. Alexander et al., 2009; Hoffmann and Alexander, 2009; Yue et al., 2013; Hoffmann et al., 2014; Wu et al., 2015; Wright et al., 2016). Also, gravity-waves have been studied using limb-sounding instruments. For example, this includes observations made by the Sounding of the Atmosphere using Broadband Emission Radiometry (SABER) instrument (e.g. Preusse et al., 2006; Ern et al., 2008; Preusse et al., 2009; Ern et al., 2011; Wright et al., 2011; Ern et al., 2014, 2015), the HIgh Resolution Dynamics Limb Sounder (HIRDLS) instrument (e.g. Alexander et al., 2008a; Wright et al., 2011; Wright and Gille, 2011; Hertzog et al., 2012; France et al., 2012; Ern et al., 2014, 2015), and radio occultation measurements from the Constellation Observing System for Meteorology, Ionosphere and Climate (COSMIC) instrument (e.g. Alexander et al., 2008b, 2013; Wang and Alexander, 2010; Tsuda et al., 2011; Wright et al., 2011; McDonald, 2012; Hindley et al., 2015).

The large number of studies undertaken over these past decades have helped to significantly advance the understanding of atmospheric gravity waves. However, a number of questions still remain, including the characterisation and quantification of wave sources and the propagation conditions that lead to the large-scale dynamical features present in the atmosphere (e.g. Fritts and Alexander, 2003). We will now go on to discuss the physics of these waves in more detail.

1.2.3.2 The Gravity-Wave Dispersion Relation

A dispersion relation describes the relationship between a wave's spatial characteristics and its frequency. A number of derivations can be found for the gravity-wave dispersion relation, for example in Hines (1960), Houghton (1977), Holton (1979), Fritts and Alexander (2003), Lynch and Cassano (2006), Vallis (2006) and Nappo (2013).

Here we will derive the dispersion relation following the classic treatment of Hines (1960). This treatment assumes an idealised atmosphere, which is uniform in both temperature (i.e. isothermal) and composition, and where waves are the only superimposed perturbations. The waves themselves are assumed to occur adiabatically and the gravitational field is assumed to be constant in both magnitude and direction (Hines, 1960).

Under these assumptions, the waves are governed by Equations 1.4, 1.5 and 1.6, which are the linearised equations of motion, adiabatic state and continuous mass conservation, respectively.

$$\rho_0\left(\frac{\partial \mathbf{U}}{\partial t}\right) = \rho g - \nabla p \tag{1.4}$$

$$\frac{\partial p}{\partial t} + \mathbf{U}\cdot\nabla p_0 = C^2\left[\frac{\partial \rho}{\partial t}\mathbf{U}\cdot\nabla\rho_0\right] \tag{1.5}$$

$$\frac{\partial \rho}{\partial t} + \mathbf{U}\cdot\nabla\rho_0 + \rho_0\nabla\cdot\mathbf{U} = 0 \tag{1.6}$$

Equations 1.4, 1.5 and 1.6 relate the perturbation velocity, $\mathbf{U}$, the perturbed atmospheric pressure, p, and density, ρ, where the unperturbed values are noted by p_0 and ρ_0, respectively, and the gravitational acceleration, g, and the speed of sound, C. The speed of sound is related to the unperturbed pressure and density, and the ratio of specific heats for constant pressure and volume, γ, by Equation 1.7. Under the idealised atmosphere assumptions, γ, C and g are all constant.

$$C^2 = \frac{\gamma p_0}{\rho_0} \tag{1.7}$$

The static condition for Equation 1.4, such that $\left(\frac{\partial \mathbf{U}}{\partial t}\right) = 0$, is given by Equation 1.8.

$$0 = \rho g - \nabla p \tag{1.8}$$

Combining Equations 1.7 and 1.8 shows that $p_0, \rho_0 \propto e^{(\frac{-z}{H})}$, where the scale height, $H \equiv \frac{C^2}{\gamma g}$, and z is the cartesian coordinate in the direction opposed to gravity (upward).

Wave solutions of Equations 1.4, 1.5 and 1.6 can be found in the complex Fourier form, such that

$$\frac{(p - p_0)}{p_0 P} = \frac{(p - p_0)}{\rho_0 R} = \frac{U_x}{X} = \frac{U_Z}{Z} = A e^{i(wt - K_x x - K_z z)} \tag{1.9}$$

where P, R, X, Z and A are all constant, ω is a real constant and K_x, K_z are complex wavenumbers, where x is a horizontal cartesian co-ordinate perpendicular to the z-axis. The wavenumbers in Equation 1.9 are related to the wave frequency by the dispersion relation, which can be derived as a necessary condition for 1.9 and is shown in Equation 1.10.

$$\omega^4 - \omega^2 C^2 (K_x + K_z)^2 + (\gamma - 1) g^2 K_x^2 + i\gamma g \omega^2 K_z = 0 \tag{1.10}$$

The polarisation relations in Equations 1.11, 1.12, 1.13 and 1.14 provide further conditions, which determine the relative magnitudes and phases due to pressure variations, density variations, horizontal motion and vertical motion, respectively.

$$P = \gamma \omega^2 K_z - \frac{i\gamma g \omega^2}{C^2} \tag{1.11}$$

$$R = \omega^2 K_z + i(\gamma - 1) g K_x^2 - \frac{i\gamma g \omega^2}{C^2} \tag{1.12}$$

$$X = \omega K_x K_z C^2 - i\gamma g \omega K_x \tag{1.13}$$

$$Z = \omega^3 - \omega K_x^2 C^2 \tag{1.14}$$

In the absence of gravity the dispersion relation in Equation 1.10 reduces to the simple form shown in Equation 1.15, which describes sound propagation.

$$\omega^2 = C^2(K_x^2 + K_z^2) \tag{1.15}$$

However, in the presence of gravity, no solutions exist in Equation 1.10 where both K_x and K_z are purely real and not equal to 0. It is thus appropriate to seek a solution where K_x is real ($k_x = \Re(K_x)$) and then determine the resulting K_z. This is appropriate if we assume that the amplitude does not decay exponentially with horizontal distance, which is the case for a horizontally propagating wave.

This leads to two possibilities. If K_z is purely imaginary then the vertical propagation is inhibited. These 'evanescent' waves (non-propagating) are external waves that may only propagate along a stratified fluid boundary (e.g. the ocean surface), and so are not relevant to the case of the atmosphere. The other possibility is that shown in Equation 1.16, where $k_z = \Re(K_z)$.

$$\begin{aligned} K_z &= k_z + \frac{i\gamma g}{2C^2} \\ &= k_z + \frac{i}{2H} \end{aligned} \tag{1.16}$$

Equation 1.16 does permit vertical propagation. Thus, these waves are characterised as 'internal'. In the case of internal waves the dispersion relation can be expressed in terms of just the real wavenumbers k_x and k_z by extracting the common term $\frac{i}{2H}$ from the complex vertical wavenumber of all modes, as in Equation 1.17.

$$\omega^4 - \omega^2 C^2(k_x + k_z)^2 + (\gamma - 1)g^2 k_x^2 - \omega^2 \frac{\gamma^2 g^2}{4C^2} = 0 \tag{1.17}$$

This can be solved as a quadratic equation in ω^2, where the two positive roots for ω reveal that internal gravity waves can exist with frequencies above the acoustic frequency, ω_a (Equation 1.18), and below the Brunt-Väisälä frequency, N (Equation 1.19), for all gases where $1 < \gamma < 2$ and $N < \omega_a$.

$$\omega_a \equiv \frac{\gamma g}{2C} \tag{1.18}$$

$$N \equiv (\gamma - 1)\frac{g}{C} \tag{1.19}$$

Thus, two distinct types of internal waves can occur. One type occurs at high frequencies, $\omega > \omega_a$, are longitudinal, and are described as *acoustic waves*. The other occurs at low frequencies, $\omega < N$, are transverse, and are described as *internal atmospheric gravity waves*. No internal waves can propagate with frequencies in the range, $N \leqslant \omega \leqslant \omega_a$. Gravity waves are the type of internal wave with $\omega < N$. The Brunt-Väisäilä frequency corresponds to a period of approximately 5 minutes in much of the atmosphere.

A gravity wave that has a frequency equal to the Brunt-Väisäilä frequency corresponds to an air parcel that is undergoing purely vertical displacement, where the balance of force is purely between the buoyancy of the air parcel and the influence of gravity upon it. An air parcel that is displaced vertically, but also with a horizontal displacement component, will oscillate at a lower frequency, which depends on the angle of displacement. The Coriolis force becomes increasingly significant as the angle of the air parcel's motion becomes increasingly horizontal. This imposes a lower limit on the gravity-wave frequency spectrum, which is given by the inertial frequency, f, shown in Equation 1.20, where, ϕ, is the latitude and, Ω, is the Earths rotational velocity.

$$f = 2\Omega \sin \phi \tag{1.20}$$

The inertial frequency is dependent on latitude, such that it is greater at the poles and tends towards zero at the equator. Thus, the inertial frequency corresponds to a period that is 12 hours at the poles, approximately 15 hours at Bath and approaches infinity at the equator. The actual spectrum of gravity waves will thus be in the range $N < \omega < f$.

1.2.3.3 The Sources of Internal Atmospheric Gravity Waves

Gravity waves have a number of sources, but predominantly propagate upwards from the troposphere (e.g. Thompson, 1978). The sources are generally split into two classes; orographic and non-orographic. Orographic source mechanisms are due to topography. Non-orographic sources are primarily attributed to convective generation. However, other mechanisms can also include jet instabilities, body forcing by

wave dissipation and wave-wave interactions, and at greater altitudes auroral heating and eclipse cooling can also act as sources (e.g. Fritts and Alexander, 2003).

Orographic gravity waves, otherwise known as lee waves or mountain waves, occur when flow is forced over topography. The image of lenticular clouds presented in Figure 1.10 are formed from mountain waves. These waves are generated from stationary sources, and as a result are generated with zero horizontal phase speed and have source locations that are inherently predictable. The combination of strong winds and large mountains aligned perpendicular to the flow can generate gravity waves of very large amplitude, which may then be advected downwind (e.g. Hindley et al., 2015) in a process that is notably strong over the southern Andes.

Convection is the most prominent non-orographic source of gravity waves. Convectively generated waves have non-stationary sources. This results in waves with a broad spectrum of horizontal phase speeds and makes it much more difficult to identify their specific sources. Convective generation is the dominant source of gravity waves in the tropics (Fritts and Alexander, 2003) and the focus of this thesis.

Convective generation, in comparison, is poorly understood, but it is thought to result from one or more of the following mechanisms. The first proposed mechanism for convective generation relates to the pure thermal forcing from the latent heat released in clouds. While the horizontal spectrum of gravity waves is broad in this case, the vertical wavelength is closely related to the depth of the thermal forcing (Pandya and Alexander, 1999). Convection has also been proposed to act as an obstacle to the flow (Clark et al., 1986). Clark et al. (1986) concluded from simulations that gravity waves were generated by both thermal forcing and due to the obstacle effect, but that the obstacle effect was a more efficient generator of gravity waves. The other proposed mechanism is a mechanical oscillator effect caused by oscillatory updrafts which generate waves with equivalent frequencies (Fovell et al., 1992; Fritts and Alexander, 2003). Gravity-wave parameterisation schemes have been developed especially for waves generated by convection (e.g. Beres et al., 2005; Lott and Guez, 2013) but perform poorly as they are inadequately constrained by observations (e.g. Vincent et al., 2013).

1.2.3.4 Critical Level Filtering of Gravity Waves

Critical levels occur when the phase speed of the wave is equal to the background flow. Critical level filtering controls the amount of waves that ascend through the

atmosphere from tropospheric sources. At a critical level the wave will either be absorbed or reflected. This coupling between the wave and the background flow results in the transfer of energy and momentum to the mean-flow, and prevents the wave from ascending further.

The intrinsic phase speed for gravity waves is given by $\hat{c_x} = c - u$, where $\hat{c_x}$ is the intrinsic phase speed, c, is the phase speed with respect to the ground, and $\bar{u}$ is the horizontal wind speed. Here, intrinsic refers to the phase speed of the wave relative to the flow. When the wave encounters a level where $c = \bar{u}$, the intrinsic phase speed will be zero. Since the vertical wavenumber, $k_z = \frac{N}{\hat{c_x}}$, the vertical wavelength shrinks to zero and the wave becomes evanescent. In the real atmosphere this point is never reached as instability and dissipation mechanisms become increasingly likely as $\bar{u}$ tends towards c (Fritts and Alexander, 2003).

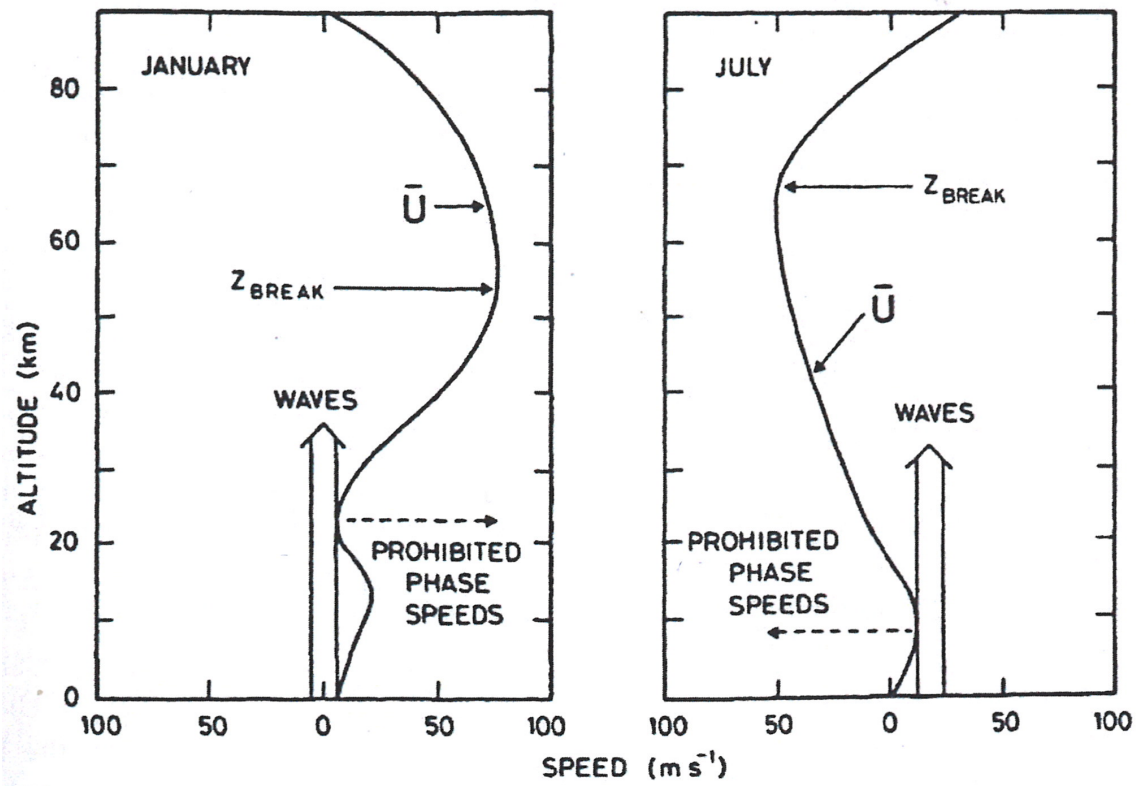

Figure 1.12: *An illustration of critical level filtering of ascending gravity waves, reproduced from Brasseur and Solomon (2005).*

Waves may encounter critical levels at different heights, the precise height being determined by the phase speed of the wave and the profile of horizontal winds it encounters. This results in the transfer of wave energy to the background atmosphere, which limits the growth in wave amplitude and causes the wave to become unstable

and dissipate its energy and momentum into the background flow. This is illustrated by Figure 1.12. Thus, the critical level filtering of gravity waves plays a crucial role in controlling the dynamics of the stratosphere and mesosphere regions.

1.2.3.5 The Breaking of Gravity Waves in the Atmosphere

Wave amplitude grows exponentially as waves propagate vertically (see Section 1.2.2). In the real atmosphere, wave amplitude will actually grow exponentially until the wave encounters a height where it becomes unstable and 'breaks', known as the breaking level. When the breaking level is reached the wave will deposit its energy and momentum into the background flow, and thus gravity waves act as an important dynamical coupling mechanism between different atmospheric layers.

The two primary instabilities that result in wave breaking are convective instabilities and shear instabilities. Convective instabilities occur when the wave drives temperature gradients to be superadiabatic (i.e. > 9.8 K km^{-1}) and cause local instabilities. Shear instabilities are caused by a vertical shear in the horizontal winds. Flow is dynamically stable when the Richardson number, given by Equation 1.21, is less than 0.25.

$$R_i = \frac{N^2}{\bar{u_z}^2 + \bar{v_z}^2} \tag{1.21}$$

In Equation 1.21 $\bar{u_z}^2$ and $\bar{v_z}^2$ are the zonal and meridional wind shears, respectively. Shear instabilities occur when the Richardson number is between 0 and 0.25, and convective instabilities occur for Richardson numbers of less than zero (e.g. Dunkerton, 1984; Fritts and Rastogi, 1985; Fritts and Alexander, 2003). Both convective and shear instabilities tend to occur at similar wave amplitudes (e.g Dunkerton, 1984; Fritts and Rastogi, 1985), only differing significantly for low frequency waves (Fritts and Alexander, 2003). For these waves the shear instability has greater importance due to the transverse velocities induced by the Coriolis force (Fritts and Rastogi, 1985).

1.2.4 Planetary Waves

Planetary waves are large-scale oscillations that are coherent around a circle of latitude with predominantly low wavenumbers. They can be stationary or zonally prop-

agating features and can reach large amplitude as they propagate upwards. They are excited in the troposphere due to topography, differences in the heating of land and ocean areas, and convection.

In the equatorial atmosphere, which is the focus of this work, the two main types of planetary waves are Kelvin waves and mixed Rossby-gravity waves. Kelvin waves are equatorially-trapped, and propagate along the boundary provided by the reversal of the Coriolis force at the equator. They have an approximately Gaussian profile of amplitude as a function of latitude, maximising at the equator. The air parcel perturbation velocities are purely zonal and the propagation of the wave is always eastward along the equator. An illustration of a Kelvin wave is presented in Figure 1.13.

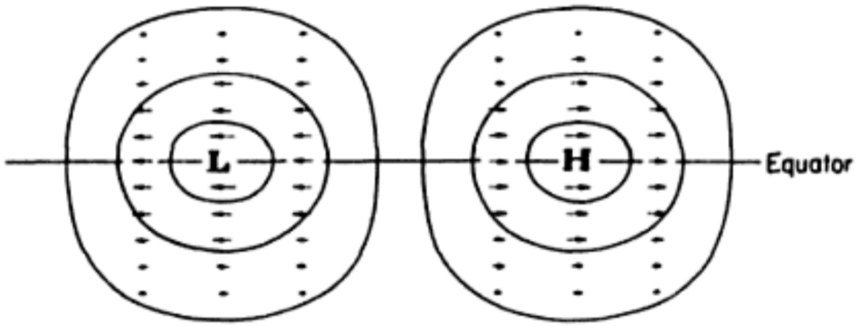

Figure 1.13: *Schematic illustration of equatorially-trapped Kelvin-wave geopotential (lines) and wind perturbations (arrows). Note that the wave is symmetric about the equator, with maximum amplitude at the equator. Kelvin waves generally have low zonal wavenumbers. Reproduced from Andrews et al. (1987), which was adapted from Matsuno (1966).*

Mixed Rossby-gravity waves, also known as Yanai waves, are also equatorially trapped like Kelvin waves, but propagate westwards. These waves tend to have higher zonal wavenumbers and also have a meridional perturbation velocity component. The meridional component of the wave amplitude is symmetric about the equator and decays with increasing latitude. However, the zonal component is antisymmetric about the equator, with opposing maxima and minima away from the equator as presented in Figure 1.14.

Kelvin waves and mixed Rossby-gravity waves are somewhat complementary as they tend to occur in different wind regimes, and have phase speeds and zonal momentum of opposite direction (e.g. Smith, 2003). A summary of the characteristics of these waves is given in Table 1.1.

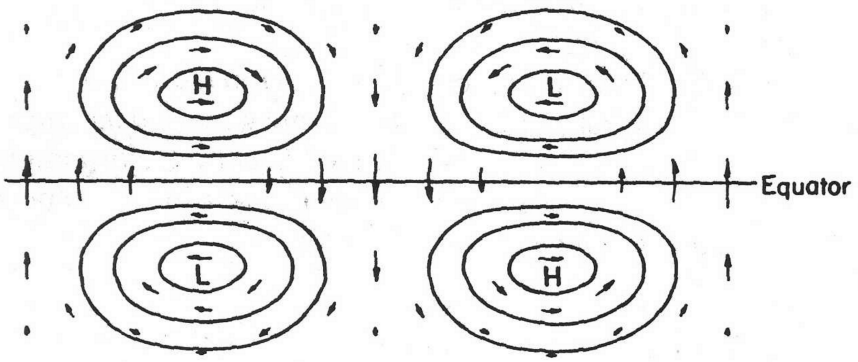

Figure 1.14: *Schematic illustration of equatorially-trapped mixed Rossby-gravity-wave geopotential (lines) and wind perturbations (arrows). Note that the wave is antisymmetric about the equator, with maximum amplitudes away from the equator. Mixed Rossby-gravity waves tend to have higher zonal wavenumbers compared to Kelvin waves. Reproduced from Andrews et al. (1987), which was adapted from Matsuno (1966).*

Theoretical description	Kelvin wave	Rossby-gravity wave
Discovered by	Wallace and Kousky (1968)	Yanai and Maruyama (1966)
Period (ground-based) $2\pi\omega^{-1}$	15 days	4–5 days
Zonal wave number $s = ka\cos\phi$	1–2	4
Vertical wavelength $2\pi m^{-1}$	6–10 km	4–8 km
Average phase speed relative to ground	$+25\ \mathrm{m\,s^{-1}}$	$-23\ \mathrm{m\,s^{-1}}$
Observed when mean zonal flow is	Easterly (max. $\approx -25\ \mathrm{m\,s^{-1}}$)	Westerly (max. $\approx +7\ \mathrm{m\,s^{-1}}$)
Average phase speed relative to maximum zonal flow	$+50\ \mathrm{m\,s^{-1}}$	$-30\ \mathrm{m\,s^{-1}}$
Approximate observed amplitudes		
u'	$8\ \mathrm{m\,s^{-1}}$	$2\text{–}3\ \mathrm{m\,s^{-1}}$
v'	0	$2\text{–}3\ \mathrm{m\,s^{-1}}$
T'	2–3 K	1 K
Approximate inferred amplitudes		
Φ'/g	30 m	4 m
w'	$1.5 \times 10^{-3}\ \mathrm{m\,s^{-1}}$	$1.5 \times 10^{-3}\ \mathrm{m\,s^{-1}}$
Approximate meridional scales $\left(\frac{2N}{\beta\lvert m\rvert}\right)^{1/2}$	1300–1700 km	1000–1500 km

Table 1.1: *Characteristics of equatorially-trapped Kelvin waves and mixed Rossby-gravity waves in the equatorial lower stratosphere. From Andrews et al. (1987).*

As discussed in Section 1.2.3.4, when a wave encounters a critical level where its phase speed matches the speed of the horizontal flow, it will no longer propagate and the momentum and energy of the wave is absorbed by the flow. Kelvin waves, which have eastward phase speeds, will thus propagate freely through westward winds but may be inhibited by eastward winds. Similarly, mixed Rossby-gravity waves, which have westward phase speeds, will thus propagate freely through eastward winds but may be inhibited by westward winds. The momentum deposited by these waves when they interact at critical levels contributes to the driving of the QBO, and also the SAO to a lesser extent, which dominate the seasonal to inter-annual wind variability of the equatorial stratosphere and mesosphere (Andrews et al., 1987; Smith, 2003).

1.2.5 Atmospheric Tides

Atmospheric solar tides are global-scale oscillations generated through the solar heating of chemical species, particularly ozone and water vapour, that exist at different heights in the Earth's atmosphere, as presented in Figure 1.15a. They have periods with harmonics of the solar day. The diurnal and semi-diurnal periods have the most significant amplitudes and can reach large amplitudes (> 20 ms^{-1}) in the upper mesosphere. Atmospheric tides generated by the Moon's gravitational pull are also present in the atmosphere. These have a period of 24.8 hours due to the slightly longer lunar day, and tend to have smaller amplitudes, typically of order $5 - 20\%$ of the amplitude of solar tides (e.g. Sandford and Mitchell, 2007; Sandford et al., 2007).

Atmospheric tides can be characterised as migrating (sun-following) or non migrating (non-sun following). Migrating tides will always propagate westward and are described by classical tidal theory. Non-migrating tides can be stationary or propagate in either a westward or eastward direction. It is not possible to distinguish between migrating and non-migrating tides using single-site instruments, but it can be done by using longitudinal chains of ground-based instruments or precessing satellites. Non-migrating tides can be excited by longitudinal variations in heating, such as by the latent heat release in tropical convection (e.g. Hagan and Forbes, 2003) or by non-linear interaction between tidal modes and planetary waves.

The negligible in-situ heating in the MLT region (see Figure 1.15a) implies that the large amplitude tides observed in this region have propagated up from lower heights (Andrews et al., 1987). Thus, their amplitudes will grow as they propagate upwards and they are observed to reach amplitudes of tens of ms^{-1} in the mesosphere.

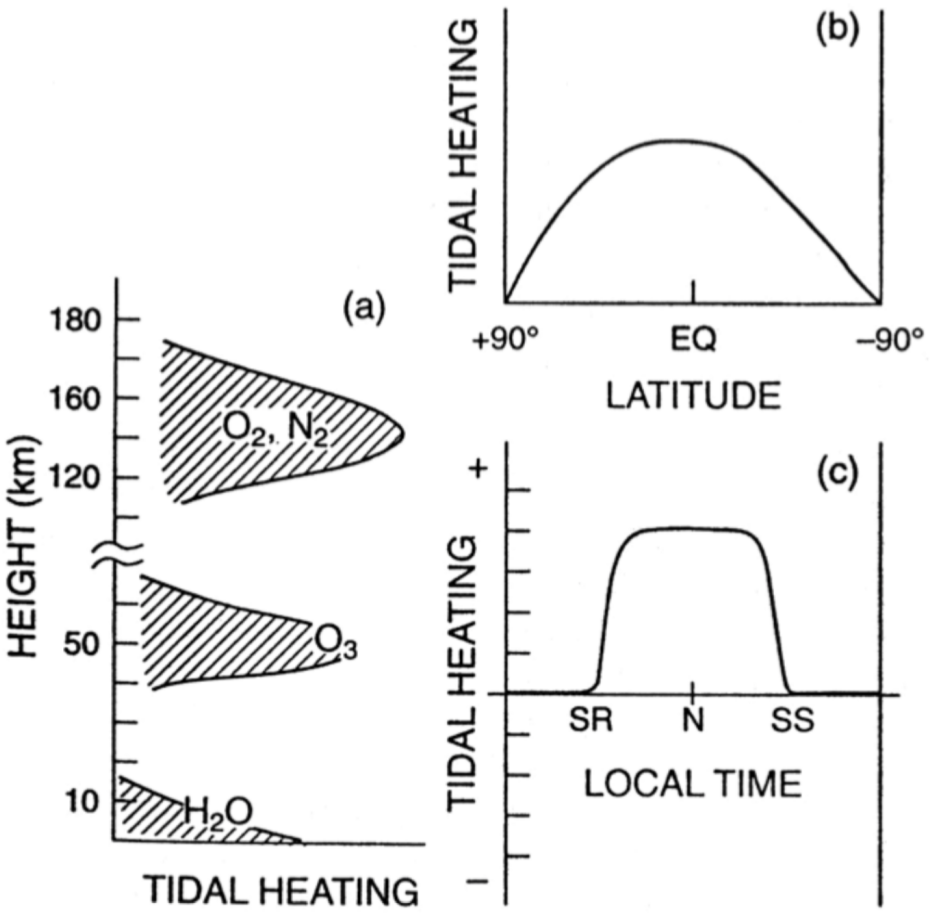

Figure 1.15: *Tidal heating as a function of height (a), latitude (b), and local time (c), reproduced from Forbes (1995). The chemical species responsible for this heating are water vapour in the troposphere, ozone in the stratosphere and lower mesosphere, and oxygen and nitrogen in the thermosphere (a). Heating is strongest over the equator and decreases with latitude (b). Heating rapidly increases and decreases as the sun rises and sets, such that the heating profile can be approximated by a square wave (c).*

Tides are generally the dominant component of the dynamics of the MLT region but are less intermittent than gravity waves and planetary waves. The large amplitude tidal fluctuations can also have an impact on the critical level filtering of ascending gravity waves (e.g. Fritts and Vincent, 1982).

1.2.6 Summary

Section 1.2 has introduced the complex field of atmospheric waves that exist in the equatorial atmosphere, which display variability on a large range of spatial and temporal scales. They act as a coupling mechanism between their sources in the troposphere

and the middle atmosphere where they encounter critical levels, break and dissipate their energy and momentum, thus driving the circulation. Consequently, these waves are fundamentally important for explaining the observed dynamics of the stratosphere and mesosphere.

Atmospheric waves are innately linked to the variability of their tropospheric sources and the variability of the atmosphere they propagate through. The rest of this chapter will discuss some of the main modes of seasonal and inter-annual variability in the equatorial atmosphere, which influence the source generation and propagation of gravity waves.

1.3 Global-Scale Seasonal and Inter-Annual Variability in the Equatorial Atmosphere

1.3.1 Introduction

Variability is inherent throughout the atmosphere and exists on a large range of temporal and spatial scales. A number of modes of variability exist in ordered global-scale structures that have specific periods resulting from factors such as the variations in solar heating or the drag induced by waves breaking in the atmosphere. This variability, which exhibits itself in a number of atmospheric properties, such as temperature and wind velocity, can influence the generation of waves through the variability in their convective sources, or the propagation of waves through critical level filtering, which results from the variability in the direction and magnitude of the mean flow.

Here we will focus on some of the dominant modes of seasonal and annual variability in the tropical atmosphere that is the focus of this thesis. These are summarised below and discussed in more detail in this Section.

- **Madden-Julian Oscillation (MJO)**: The MJO dominates the intraseasonal variability in tropospheric convection and circulation in the tropics. It has a period of approximately $30 - 90$ days and is often characterised by the slow eastward progression of tropical rainfall over the eastern hemisphere at these timescales. A comprehensive review of the MJO can be found in Zhang (2005).
- **Quasi-Biennial Oscillation (QBO)**: The QBO dominates the variability of the equatorial stratosphere. It has a period of approximately 28 months and is easily observed as downward propagating eastward and westward wind regimes (see review by Baldwin et al., 2001).
- **Semi-Annual Oscillation (SAO)**: The SAO dominates the seasonal variability in the upper stratosphere and mesosphere regions. It is thought to result from the deposition of momentum by ascending gravity waves but its mechanism is still poorly understood. Further details on the SAO can be found in Hirota (1980), Dunkerton (1982) and Vincent (2015).

1.3.2 The Madden-Julian Oscillation

On intra-seasonal timescales the variability of weather in the tropical troposphere is dominated by the MJO. This remarkable phenomena is characterised by a slow eastward progression (~ 5 ms^{-1}) of a pattern of tropical atmospheric circulation and moist convection with a period of 30–90 days. This eastward propagation is evident in Figure 1.16, which shows the lifecycle of an MJO event in composite maps of rainfall and the upper tropospheric circulation. The phases characterise the longitudinal centre of the MJO throughout its lifecycle. Note that the convective pattern is confined to the eastern hemisphere, whereas the dynamic pattern is global in extent.

As shown in Figure 1.16, the MJO is observed as an eastward moving centre of enhanced deep tropospheric convection and rainfall, the active phase (blue), flanked by two regions of suppressed rainfall and convection, the inactive phase (red). The active and inactive phases are connected by an overturning circulation that extends throughout the entire depth of the troposphere. This is observed as anomalous divergent flow at the top of the troposphere (black contours), at 200 hPa (about 13 km altitude), and anomalous converging flow near the surface, at 850 hPa (about 1.5 km altitude), in the active phase, and vice versa in the inactive phase. This overturning circulation can be seen in the illustration of the MJO presented in Figure 1.17.

The MJO is distinctly different from other types of intra-seasonal phenomena. While referred to as an oscillation, the MJO actually has a broad frequency spectrum that reflects its episodic nature. Only one fully developed MJO event exists at any given time. As shown in Figures 1.16 and 1.17, while the dynamic component of the MJO is observed at all longitudes, the zonal scale of the convective component is confined to the eastern hemisphere due to the atmospheric response to localised heating (Salby et al., 1994). Its slow eastward propagation distinguishes it from other tropical atmospheric phenomena, such as Kelvin waves, which propagate eastwards at greater speeds of about 15-17 ms^{-1} (e.g. Matthews et al., 1999; Zhang, 2005).

A number of mechanisms have been proposed for the eastward progression of the MJO, but it is still poorly understood and is often weakly represented by global weather/climate models (e.g. Matthews et al., 1999; Zhang, 2005; CLIVAR, 2009; Serra et al., 2014; Jiang et al., 2015). Extensive interactions exist between MJO modulations and seasonal to inter-annual climate variations (CLIVAR, 2009). For example, this includes links to the onset of the different Monsoons (e.g. Hendon and Liebmann, 1990; Sperber et al., 2001; Lorenz and Hartmann, 2006; Bhatla et al.,

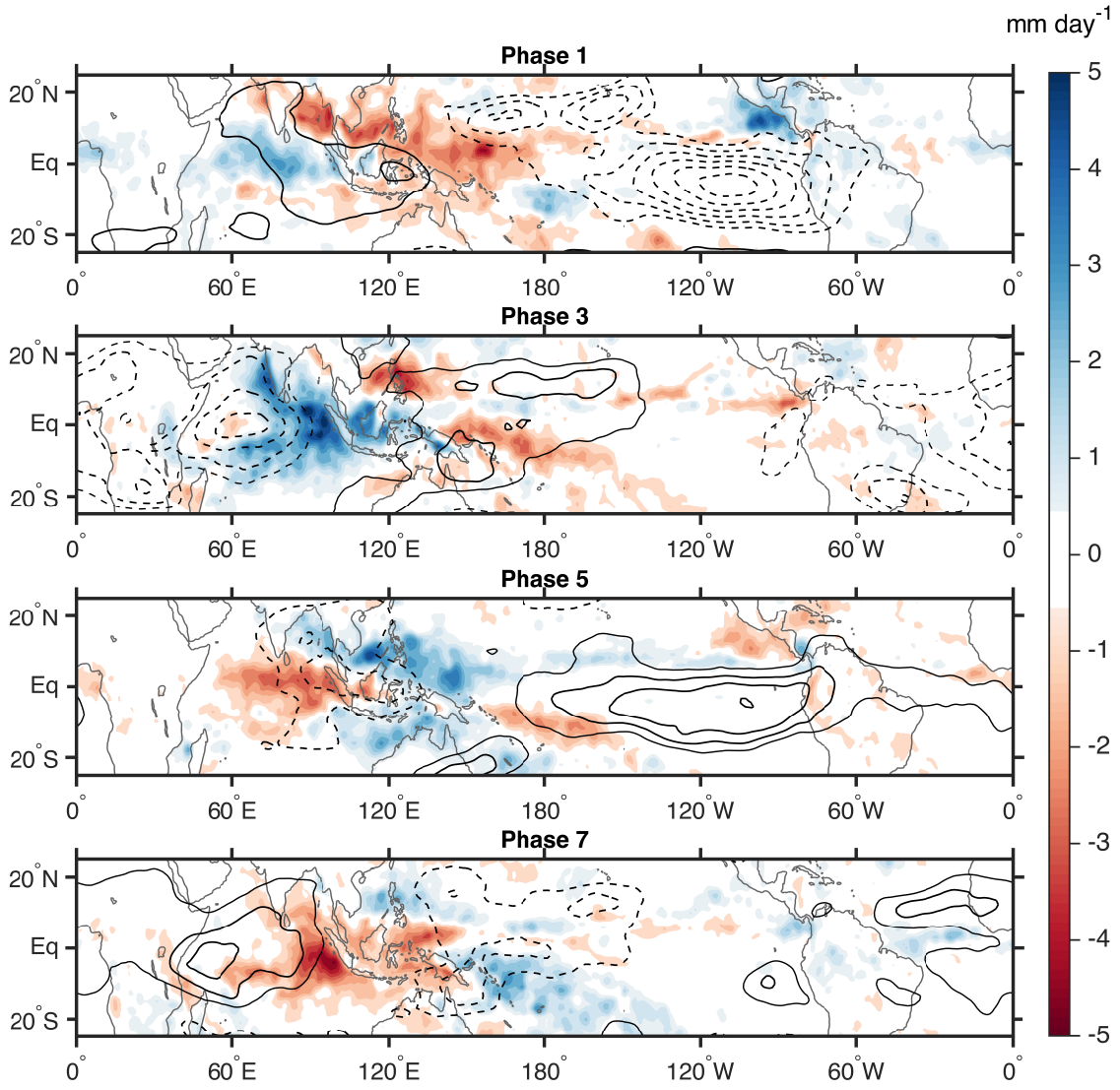

Figure 1.16: *The propagation of precipitation (colour filled contours) and upper tropospheric (200 hPa) zonal wind (black contours) anomalies for phases 1, 3, 5 and 7 of the 8 MJO phases. Eastward and westward zonal winds are depicted by solid and dashed lines, respectively, in intervals of 1 ms^{-1} starting from ± 2 ms^{-1}. Precipitation observations are from the Tropical Rainfall Measurement Mission and zonal winds are from ECMWF Reanalysis data (see Section 2.3 for further details). The eastward progression of the convective centre and upper tropospheric flow is clearly evident. Importantly, note also that that convective centre is predominantly confined to the eastern hemisphere, whereas the upper tropospheric zonal winds extend globally through all longitudes.*

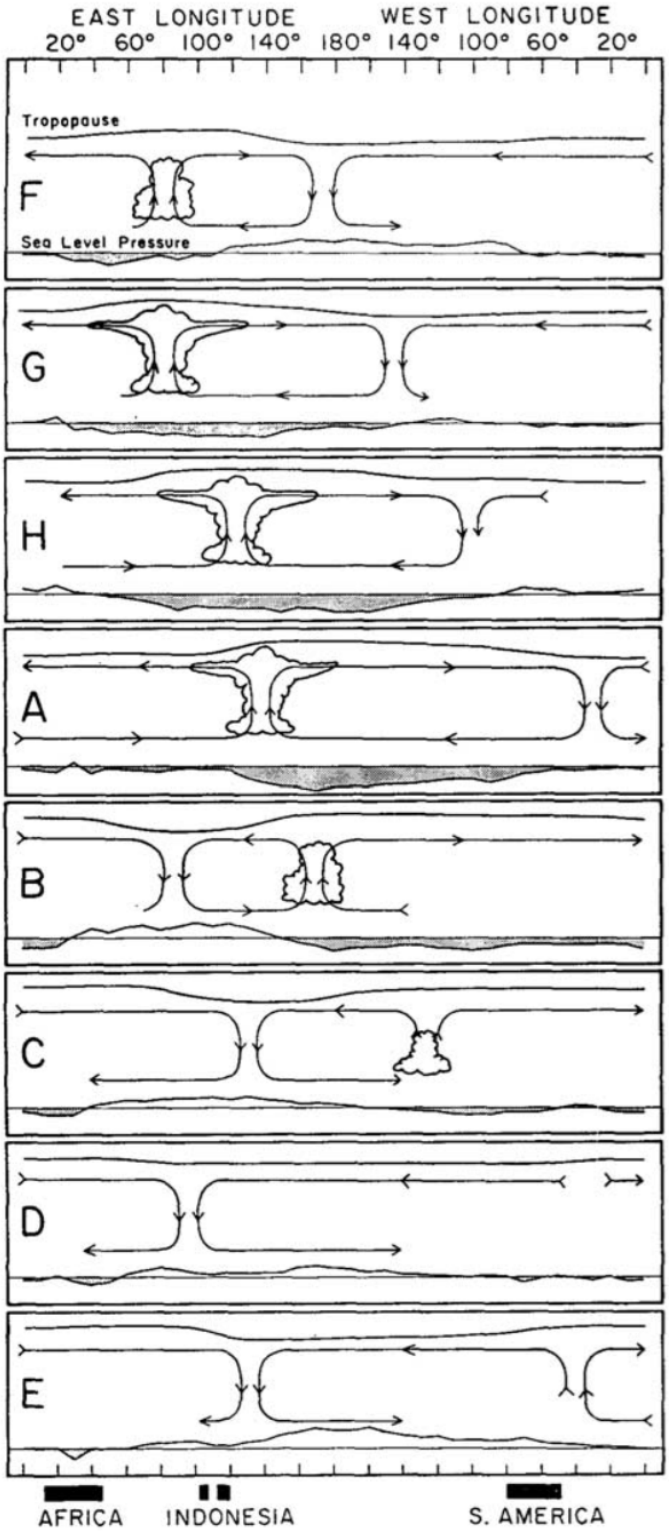

Figure 1.17: *Illustration of the fundamental large-scale features of the Madden-Julian Oscillation (MJO) throughout its life cycle (from top to bottom), from Madden and Julian (1972). In the figure, cloud symbols represent the convective centre and arrows indicate the zonal circulation. The curves above and below the circulation represent the upper tropospheric and sea level pressure perturbations, respectively.*

2016), the timing and evolution of the El Niño Southern Oscillation (e.g. Hendon et al., 2007; Tang and Yu, 2008; Hoell et al., 2014) and extratropical weather patterns and circulation (e.g. Liebmann and Hartmann, 1984; Garfinkel et al., 2014; Fauchereau et al., 2016). The MJO is also known to be closely associated with convectively coupled Rossby and Kelvin waves (e.g Matthews et al., 1999; Matthews, 2000; Sperber, 2003; Kiladis et al., 2009; Khouider et al., 2011). Detailed reviews on the MJO can be found in Madden and Julian (1994), Zhang (2005) and Serra et al. (2014).

Given the significant modulation of convection by the MJO, a simple assumption would be for this modulation to manifest itself in the source variability of gravity waves, and thus influence the flux of gravity-waves observed in the stratosphere and mesosphere. Evidence for this assumption has been provided by observations of MJO periodicities in the MLT winds, as shown in Figure 1.18 (e.g. Eckermann et al., 1997; Isoda et al., 2004; Rao et al., 2009; Davis et al., 2012). Eckermann et al. (1997) also observed MJO periodicities in gravity-wave variances in the MLT region, suggesting that the dissipation of these waves cause the MJO modulation of the winds. However, it has also been suggested that this may be due to the variability in atmospheric tides (e.g. Isoda et al., 2004).

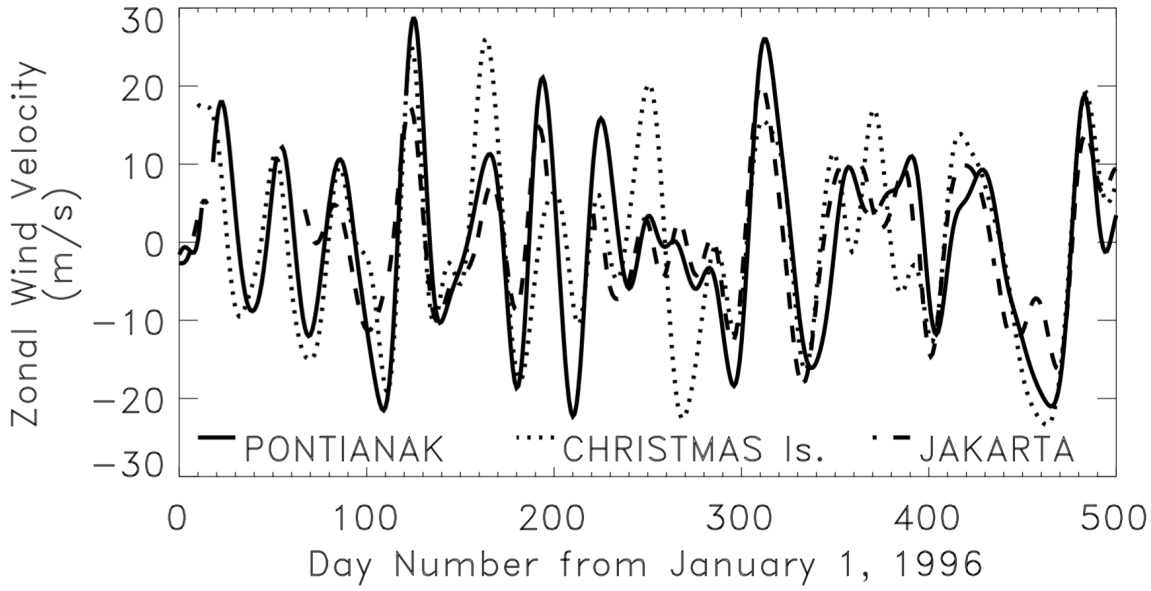

Figure 1.18: *Example of intra-seasonal oscillations in 20–100 day bandpassed zonal wind velocities in the MLT region, from Isoda et al. (2004). The figure shows significant modulation of zonal winds observed by a meteor radar at Jakarta (6° S, 107° E), and two medium-frequency radars at Pontianak (0° N, 109° E) and Christmas Island (2° N, 157° W) over a 500 day period starting on January 1st 1996.*

A small number of localised studies have provided evidence of MJO modulations of gravity waves in the stratosphere. For example, Karoly et al. (1996) reported a significant correlation between gravity-wave activity measured from radiosonde observations in the south Pacific and proxies of convection during a significant MJO event. However, Horinouchi (2008) used a cloud-resolving model to observe a significant correlation of gravity waves with the inactive phase of the MJO, where convection is reduced. This was suggested to result from larger phase speeds and longer vertical wavelengths, which favoured upward propagation.

Thus, the connection between the MJO and gravity-wave activity is still largely unknown. In particular, evidence of such a modulation has been confined to localised studies. In this thesis, we will answer the question, "does the MJO modulate the variability of stratospheric gravity waves?", by considering the large-scale variability of gravity-wave activity in the tropical stratosphere. This is compared to both the convective and dynamic signatures of the MJO to assess whether the modulation is a consequence of variability in gravity-wave sources or variability in the critical-level filtering of ascending waves. The results of this work are presented in Chapter 3 and are published in Geophysical Research Letters (Moss et al., 2016b).

1.3.3 Large-Scale Variability in the Stratosphere and Mesosphere

The QBO and SAO dominate the variability in the stratosphere and mesosphere. The vertical amplitudes of the stratospheric QBO (SQBO) and SAO (SSAO), and mesospheric QBO (MQBO) and SAO (MSAO), are presented in Figure 1.19, reproduced from Baldwin et al. (2001).

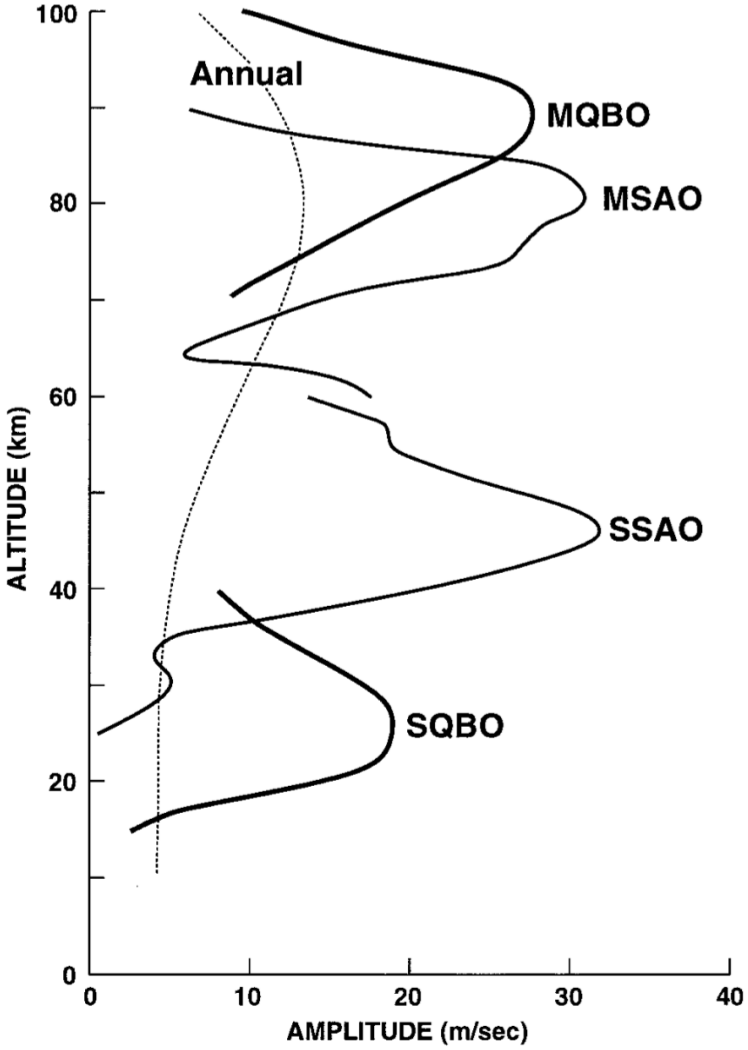

Figure 1.19: *Vertical amplitude distribution of the quasi-biennial oscillation (QBO) and semi-annual oscillation (SAO). The figure is from Baldwin et al. (2001) and is produced using UARS/HRDI observations (Burrage et al., 1996), rocket observations from Ascension Island (Hirota, 1978) and the COSPAR International Reference Atmosphere (CIRA-86).*

1.3.3.1 The Quasi-Biennial Oscillation

Figure 1.19 shows the SQBO and MQBO have maximum amplitudes of around 20 ms^{-1} and 25 ms^{-1}, respectively. The SQBO peaks at a height of approximately 25 km and the MQBO at approximately 95 km. The SQBO is thus the dominant mode of variability in the equatorial stratosphere. However, in the mesosphere the MSAO and annual components have significant amplitudes at similar heights to the MQBO. The amplitude of the QBO between 40 and 70 km is not shown due to the uncertainty in defining what part of the variability is related to the QBO.

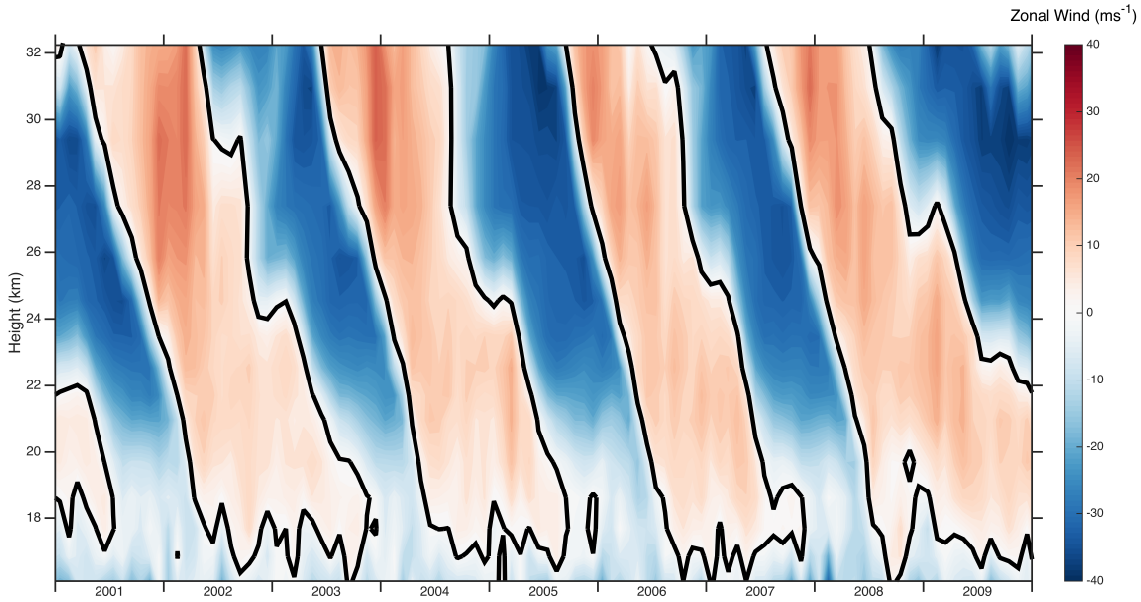

Figure 1.20: *Zonal-wind data from the Singapore radiosonde dataset for the period 2001–2009. The QBO evidently dominates the variability in zonal wind in the stratosphere. The thick black line indicates the 0 ms^{-1} wind contour. These data are available online from the Freie Universität Berlin at http://www.geo.fu-berlin.de/en/met/ag/strat/produkte/qbo/.*

Figure 1.20 presents the SQBO as manifested in zonal-wind data from the Singapore radiosonde dataset. The QBO is observed as a downward propagation of alternating eastward (red) and westward (blue) wind regimes. The QBO generally exhibits stronger winds in its westward phase, reaching speeds of approximately 30–35 ms^{-1} compared to winds of order 15–20 ms^{-1} in the eastward phase. While the average period is around 28 months, both the period and amplitude of the QBO vary from cycle to cycle.

The QBO is one of the most striking examples of wave mean-flow interaction in the Earth's atmosphere and is driven by the momentum deposition of a combination of

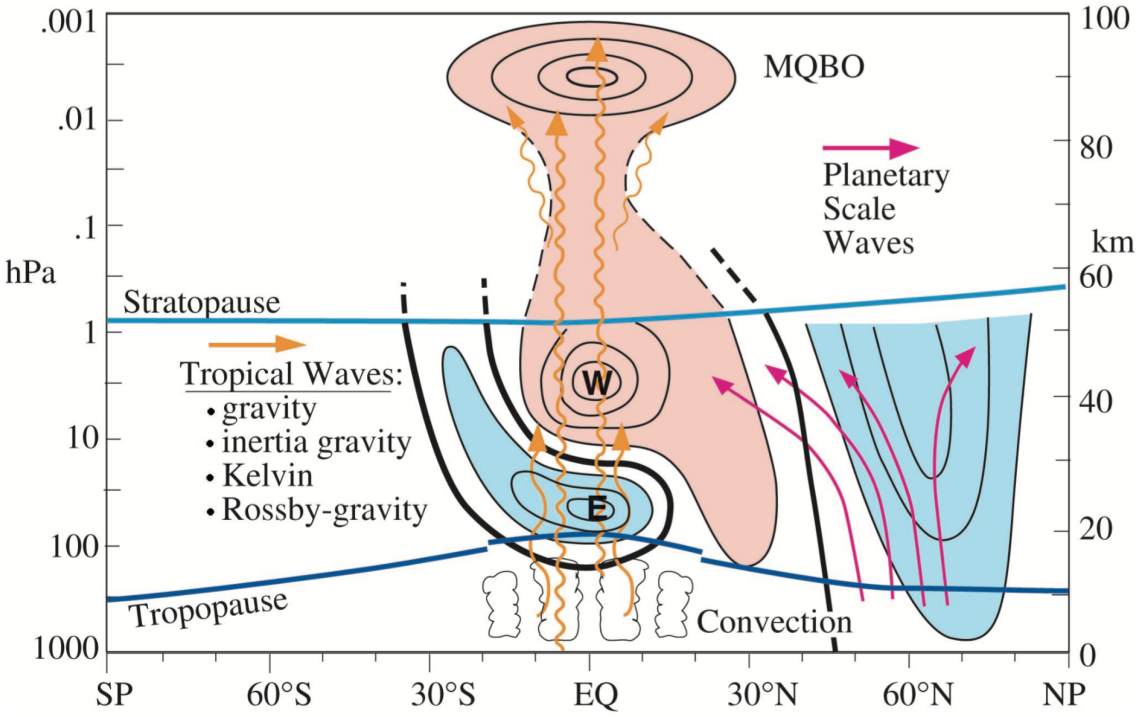

Figure 1.21: *Illustration of the dynamics of the QBO during northern winter, from Baldwin et al. (2001). The orange arrows depict various tropical waves propagating upwards to drive the QBO and the purple arrows show the propagation of planetary-scale waves at mid- to high-latitudes. The difference in zonal-mean winds between QBO easterly and westerly phases is depicted by black contours, where the QBO phase is defined by the 40 hPa equatorial zonal wind. Easterly anomalies are light blue and westerly anomalies are pink. The MQBO is also shown above 80 km and the wind contours between 50 and 80 km are dashed due to observational uncertainty.*

Kelvin, mixed Rossby-gravity and gravity waves (e.g. Dunkerton, 1997; Baldwin et al., 2001). These waves are generated in the tropical troposphere and are predominantly from convective sources. A schematic illustration of this process is presented in Figure 1.21. A detailed review of the QBO can be found in Baldwin et al. (2001).

1.3.3.2 The Semi-Annual Oscillation in the Stratosphere and Mesosphere

In the equatorial mesosphere, the principal mode of seasonal variability is the MSAO. As presented in Figure 1.19 the SSAO and MSAO peak around the stratopause and mesopause, around 50 km and 80 km, respectively, and both with amplitudes of order 30 ms^{-1}. A climatology of the winds from rocketsonde data from two low latitude sites is presented in Figure 1.22.

From Figure 1.22 a few things are apparent. Firstly, the SSAO and MSAO are centred

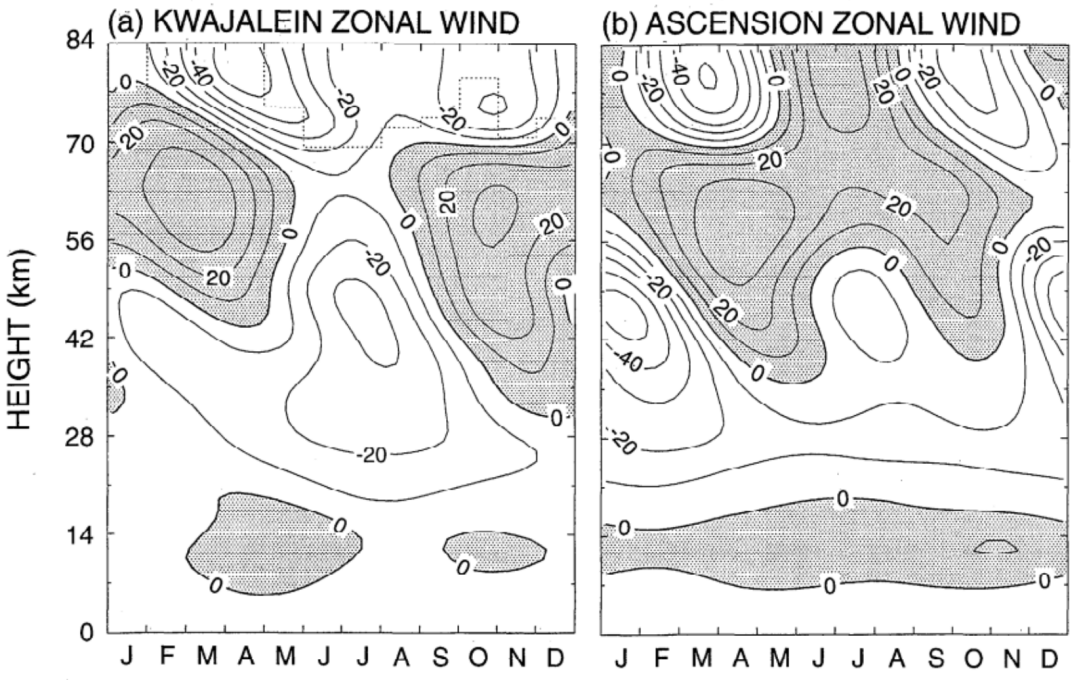

Figure 1.22: *Composite seasonal cycle of zonal winds (ms^{-1}) at (a) Kwajalein Island (9° N, 68° W) and (b) Ascension Island (8° S, 14° W) from rocketsonde data, from Garcia et al. (1997). Note that the SSAO and MSAO are centred around the stratopause and mesopause, respectively, and are out of phase with each other.*

on the stratopause and mesopause, respectively, and are out of phase. The SSAO peaks in December/January and July/August, while the MSAO peaks in March/April and September/October. Additionally, the first westward phase of the MSAO is stronger than the second westward phase. This seasonal asymmetry was first observed by Delisi and Dunkerton (1988), who attributed it to stronger dynamical forcing in northern winter. These characteristic features have been observed in a number of studies (e.g. Burrage et al., 1996; Garcia et al., 1997; Huang et al., 2008; Ratnam et al., 2008b; Peña Ortiz et al., 2010; Kumar et al., 2011; Day and Mitchell, 2013).

The causes of the MSAO are not fully understood (Vincent, 2015), but it is thought that it is entirely wave-driven (e.g. Dunkerton, 1982; Delisi and Dunkerton, 1988; Garcia et al., 1997; Garcia and Sassi, 1999). The selective filtering of waves by the eastward and westward winds of the SSAO, allows westward and eastward phase speed waves, respectively, to reach the mesosphere where they drive the MSAO. Consequently, the MSAO is out of phase with the SSAO (e.g. Dunkerton, 1982; Hitchman and Leovy, 1988)

The amplitude of the first westward phase of the MSAO is also known in some years to reach anomalously large values, over twice the climatological mean (e.g. Garcia

et al., 1997; Day and Mitchell, 2013; Moss et al., 2016a). It has been suggested that this occurs when the relative phase of the SSAO and SQBO allow favourable selective filtering, whereby an excess of westward-propagating gravity waves reach the mesosphere and drive the anomalously strong westward flow (Garcia and Sassi, 1999; Day and Mitchell, 2013). Evidence for this selective filtering mechanism was presented by Day and Mitchell (2013), who observed a narrower range of QBO winds during the anomalous MSAO westward phase event at Ascension Island (8° S, 14° W) in 2002, as shown in Figure 1.23.

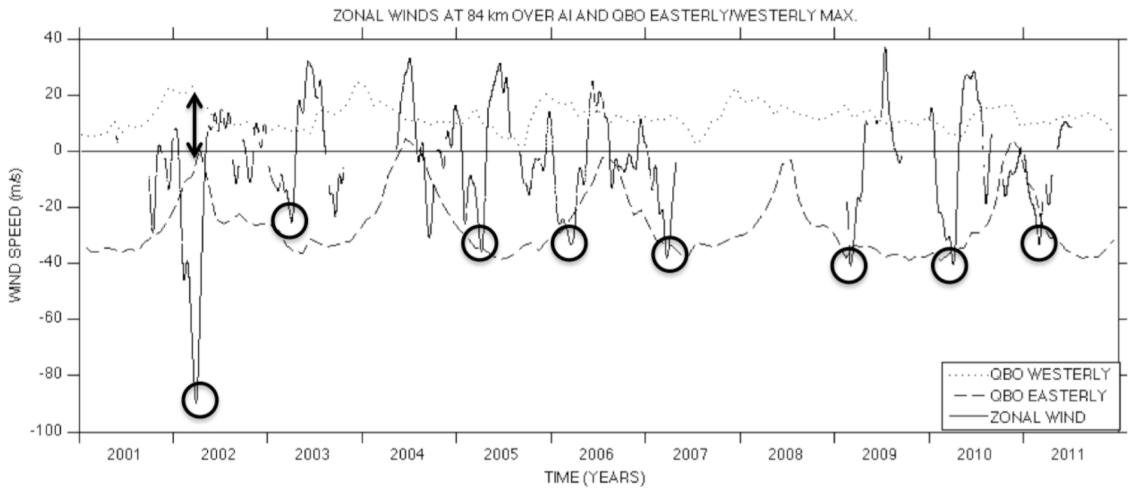

Figure 1.23: *Monthly zonal winds (solid line) from the Ascension Island (8° S, 14° W) meteor radar at 84 km, after Day and Mitchell (2013). Note the strong MSAO first westward phase winds in 2002, reaching speeds more than twice the climatological norm. The two other lines indicate the maximum eastward (dotted) and westward (dashed) winds associated with the QBO. The thick arrow shown in 2002 indicates the narrower range of winds encountered by ascending gravity waves, compared to other years, as per the QBO filtering mechanism of Garcia and Sassi (1999).*

Despite the strong suggestion that gravity waves play a dominant role in the forcing of the MSAO, it is notoriously difficult to make measurements of these waves in the mesosphere over long time periods. However, recent developments have made it possible to measure gravity-wave variances and momentum fluxes from meteor radar measurements (e.g. Hocking, 2005; Fritts et al., 2012). These techniques can now be applied to assess the contribution of gravity waves to the driving of the equatorial mesosphere (e.g. Antonita et al., 2008; Andrioli et al., 2013a,b, 2015; Moss et al., 2016a). For example, Antonita et al. (2008) demonstrated that high-frequency gravity waves provide of order 20–70% of the total MSAO forcing using meteor radar observations over southern India.

In this thesis we present the first measurements of gravity-wave variances, momentum fluxes and accelerations from the Ascension Island meteor radar. These measurement are used to assess the contribution of gravity waves to the driving of anomalous MSAO first westward phase events in the equatorial mesosphere. These results are presented in Chapter 4, and published in Moss et al. (2016a).

Chapter 2

Selected Atmospheric Measurement Techniques

Two primary sets of atmospheric measurements are used in this thesis. This chapter introduces these measurements and discusses the methods of determining gravity-wave properties from them. In addition, information is provided on the other supporting observations that are used in this thesis.

Section 2.1 introduces radio occultation measurements from the Constellation Observing System for Meteorology, Ionosphere, and Climate (COSMIC) / Formosa Satellite Mission 3 (FORMOSAT-3), a joint U.S. / Taiwanese venture. These measurements are used to study the modulation of stratospheric gravity-wave fluxes in the equatorial stratosphere in Chapter 3.

Section 2.2 introduces the method of measuring atmospheric properties from radar measurements of meteor ionisation trails. Measurements of atmospheric properties made by the Ascension Island meteor radar are used in Chapter 4 to study the influence of gravity waves on the mesospheric semi-annual oscillation.

Finally, Section 2.3, will introduce measurements of outgoing long-wave radiation, rainfall, reanalysis winds, and an index for the Madden-Julian Oscillation.

2.1 COSMIC Radio Occulation

2.1.1 Introduction to Radio Occultation

Radio occultation (RO) is a limb-sounding remote sensing technique. As a radio signal passes through the limb of a planet's atmosphere it will be refracted. As a radio receiver in orbit rises above or sets below the horizon, the tracking of a radio signal through the atmosphere, from a source such as a GPS satellite, will result in a profile of the refractive index. The refractivity will vary with height as a function of the atmosphere's properties. It is thus possible to use these refractivity measurements to determine profiles of atmospheric properties, such as temperature.

The RO technique was pioneered for studying planetary atmospheres and was first implemented by the Mariner V mission to study the atmosphere of Venus by Fjeldbo et al. (1971). The development of the Global Positioning System (GPS) network of satellites suggested RO would be an attractive and affordable way to provide a high resolution global atmospheric data-set (Yunck et al., 1988). The consequent GPS Meteorology (GPS/Met) experiment (Ware et al., 1996), Challenging Mini-satellite Payload (CHAMP) (Wickert et al., 2001) and Satellite de Aplicaciones Cientificas-C (SAC-C) (Hajj et al., 2004) missions all confirmed the potential for RO sounding of the atmosphere (Anthes et al., 2008).

2.1.2 Radio Occultation Technique

Figure 2.1 presents a schematic of the radio occultation technique and the occultation geometry (e.g. Kursinski et al., 1997; Rocken et al., 2004). As the COSMIC satellites rise above and set below the Earth's horizon the paths of the L1 (1575 MHz) and L2 (1228 MHz) radio signals from GPS satellites transverse through the Earth's atmosphere. The influence of the atmosphere on these rays can be described by the total bending angle, α, an impact parameter, a, and the tangent radius, r. A profile of the atmospheric refractive index can be retrieved from the variations in α as a function of a. The time dependence of both are derived from the accurate measurements of Doppler-shifted frequencies at the receiver. This uses the precise information about spacecraft positions and velocities to calculate the Doppler shift in the absence of atmospheric bending. Hence, the atmospheric shift can be calculated from the difference between the expected shift and the measured shift (Kursinski et al., 1997).

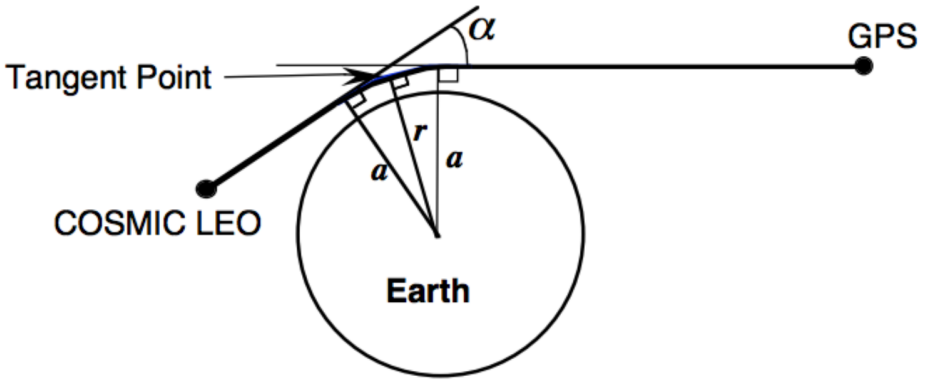

Figure 2.1: *Schematic of a COSMIC satellite tracking an occulting GPS satellite, with impact parameter, a, bending angle, α, and radius, r to the ray periapsis tangent point. Taken from (Rocken et al., 2004).*

The GPS RO retrieval methods are known as Geometrical Optics (GO) and Full Spectral Inversion (FSI). The GO method smooths the bending angle profiles of the L1 and L2 signals and applies an ionospheric calibration, although small perturbations still remain. An Abel inversion is then used to transform the bending angle to a refractive index profile which assumes the atmosphere is spherically symmetric. This method has an estimated accuracy of $0.2 - 0.4$ K (Kursinski et al., 1997) and vertical resolution is limited by Fresnel diffraction, which is about 1.5 km in the stratosphere (Tsuda et al., 2011). The FSI method implements radio holographic methods to fix complex structures due to water vapour in the troposphere and give a better vertical resolution. This method has an upper limit of 28 km (Tsuda et al., 2011). A combination of these methods is utilised by stitching them together where FSI is used for the lower portion of the atmosphere and GO above. The profiles are then combined at a height usually between 10 and 20 km (Tsuda et al., 2011).

$$N_{ref} = (n-1) \times 10^6 = 77.6\frac{p}{T} + 3.73 \times 10^5 \frac{p_w}{T^2} + 4.03 \times 10^7 \frac{n_e}{F_T^2} + 1.4W \qquad (2.1)$$

The refractivity, N_{ref}, of the atmosphere is given by Equation 2.1, where p is the atmospheric pressure in mbar, T is the atmospheric temperature in Kelvin, p_w is the total water vapour partial pressure in mbar, n_e is the electron number density per cubic meter, F_T is the transmitter frequency in Hertz, and W is the liquid water content in grams per cubic meter. The four terms represent the contributions from the dry neutral atmosphere, water vapour, free electrons in the ionosphere and particulates (primarily water). These terms are respectively due to the polarisability of molecules in the atmosphere, the large permanent dipole moment of water vapour (significant

in the lower troposphere), the number of free electrons in the ionosphere (important above $\sim 60 - 90$ km) and the scattering by water droplets. A full description of the derivation of atmospheric properties from the refractivity profile is given by Kursinski et al. (1997).

2.1.3 Resolution of the Radio Occultation Technique

Radio occultation is a limb sounding technique (see Figure 2.1) and the temperature measurements have sub-Kelvin precision (e.g. Tsuda et al., 2011). Limb sounding observations are made tangentially through the atmosphere and have a horizontal weighting function along the line of sight, which is centred on the tangent point. Limb sounding instruments tend to have much better vertical resolution than horizontal resolution. This results in a weighting function, which is 'cigar-shaped' and lies tangentially to the Earth's surface. In the stratosphere the vertical resolution of radio occultation data is approximately 1.5 km, primarily limited by Fresnel diffraction (e.g. Kursinski et al., 1997). The horizontal resolution can be approximately defined as the horizontal distance travelled by the radio signal within the atmospheric layer (e.g. Kursinski et al., 1997; Hindley et al., 2015) and is approximately 300 km in the stratosphere.

2.1.4 COSMIC Radio Occultation Measurements

2.1.4.1 The COSMIC Mission

In 2006, the Constellation Observing System for Meteorology, Ionosphere and Climate / Formosa Satellite 3 (COSMIC/FORMOSAT-3) was launched, and is the first dedicated GPS-RO satellite constellation (Rocken et al., 2000; Schreiner et al., 2007; Liou et al., 2007). Six identical micro-satellites were launched in April 2006, each carrying a GPS receiver into a 512 km altitude and 72° inclined orbit from California (Cheng et al., 2006). Over the course of the following 17 months, the satellites were moved into their final orbits, as detailed in Table 2.1. The initial months of the COSMIC mission provided a unique opportunity to obtain many closely located atmospheric soundings, which have been utilised for mesoscale atmospheric studies and estimating the precision of the RO technique (e.g. Anthes et al., 2008; Wang and Alexander, 2010).

Orbital Parameter	Information
Altitude	$750 - 800$ km
Period	≈ 100 minutes
Inclination	72°
Separation	30°

Table 2.1: *Final orbit information for the six COSMIC micro-satellites*

Figure 2.2 presents a simple illustration of the COSMIC micro-satellites and the RO technique. Each satellite carries three science payloads:

1. Tiny Ionospheric Photometer (TIP)
2. TriBand Beacon Transmitters (TBB)
3. Intergrated GPS Occulation Receiver (IGOR)

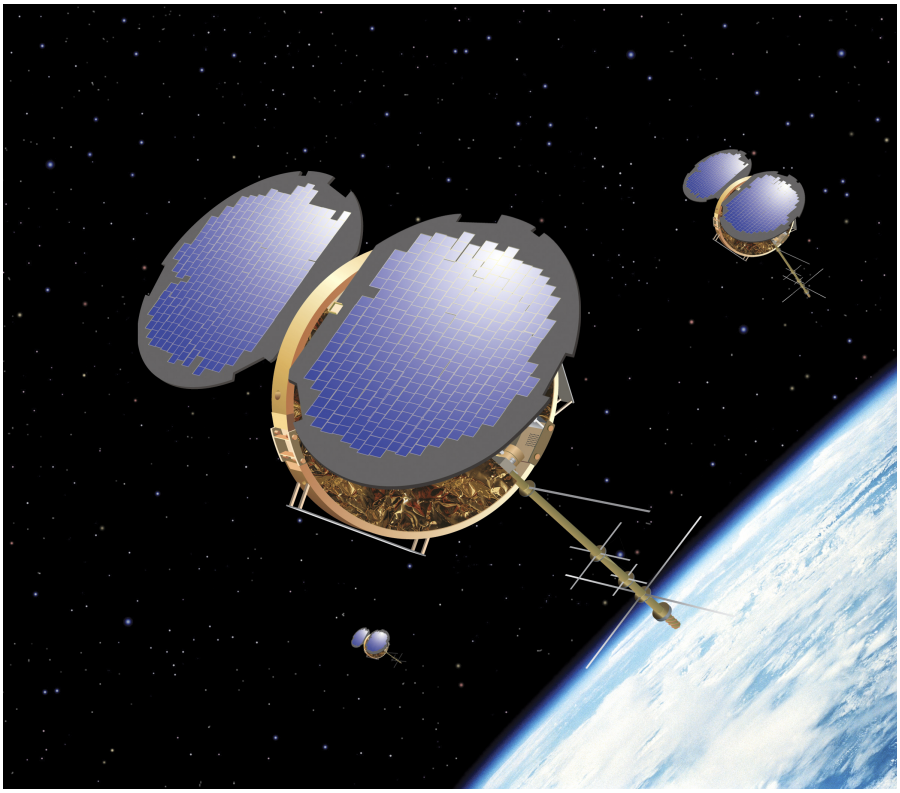

Figure 2.2: *Artists impression of the COSMIC micro-satellites. Available from the University Corporation for Atmospheric Research (UCAR) and produced by Orbital Sciences Corporation.*

The TIP and TBB instruments are payloads for ionospheric science and space weather monitoring (Rocken et al., 2000). The TIP makes nadir measurements of the ultraviolet emission from the recombination of oxygen ions and electrons in the nightside ionosphere, which can be related to the total electron content. The TBB transmits on three frequencies (150, 400 and 1000 MHz), which are used by ground or satellite receivers to determine the total electron content and ionospheric scintillation levels. The IGOR instrument is an advanced GPS RO receiver developed by the Jet Propulsion Laboratory and built by BroadReach Engineering, and is used to determine very-high vertical resolution profiles of temperature, water vapour and air density in the troposphere and stratosphere. The advantages and disadvantages of COSMIC RO data are listed in Table 2.2.

Advantages	**Disadvantages**
Good vertical resolution ($\sim$ 1 km)	Narrower altitude range than some other satellite observations
Global pseudo-random coverage, from the poles to low-latitudes	Fewer data at very low and high latitudes
Very high temperature measurement accuracy (sub-Kelvin)	Short horizontal scale waves are highly likely to not be detected (Horizontal resolution $\sim$ 300 km)
Measurements not dependent on the time of day or weather conditions	

Table 2.2: *Advantages and Disadvantages of COSMIC Radio Occultation Measurements.*

2.1.4.2 Distribution of COSMIC Radio Occultation Observations

The COSMIC satellites record approximately 1000–2000 radio occultations per day across the globe. An example of the global distribution of occultations in a typical day is presented in Figure 2.3 and histograms showing the distribution of occultations as a function of latitude and longitude are presented in Figure 2.4.

The number of occultations are approximately evenly distributed longitudinally but exhibit a large peak at mid-latitudes, a smaller peak at subtropical latitudes, and minima at the poles and equator. This non-uniform latitudinal data coverage results from the relative orbits of the COSMIC micro-satellites and the GPS satellites.

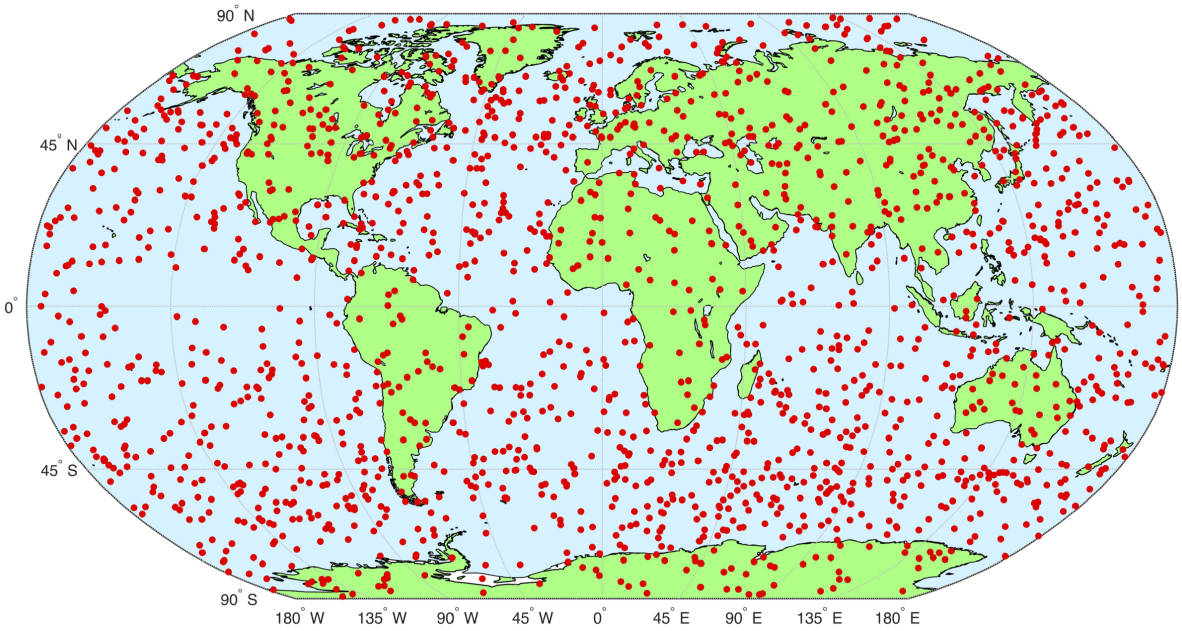

Figure 2.3: *Global distribution of 1803 radio occultations on 6th October 2008 from the COSMIC mission. The red dots represent the location of each radio occultation profile on this day.*

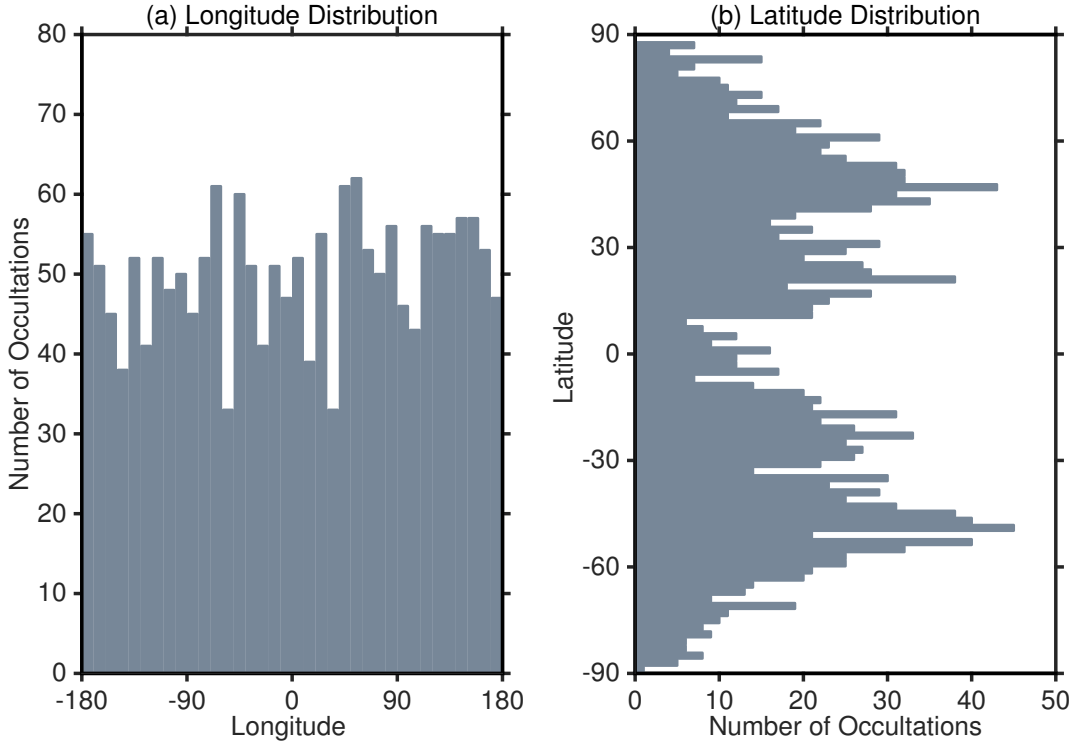

Figure 2.4: *Spatial distribution of COSMIC profiles on 6th October 2008. The panels show histograms of the number of RO soundings in (a) 10° longitude bins and (b) 2° latitude bins.*

2.1.4.3 COSMIC Temperatures and Gravity-Wave Analysis

The work presented here uses COSMIC Level-2 dry atmospheric temperature retrievals provided by the COSMIC Data Analysis and Archive Center (CDAAC), of the University Corporation for Atmospheric Research (UCAR), to study gravity waves in the tropical stratosphere. The rest of this section will discuss the analysis of these temperature data for the study of gravity waves in the tropical stratosphere.

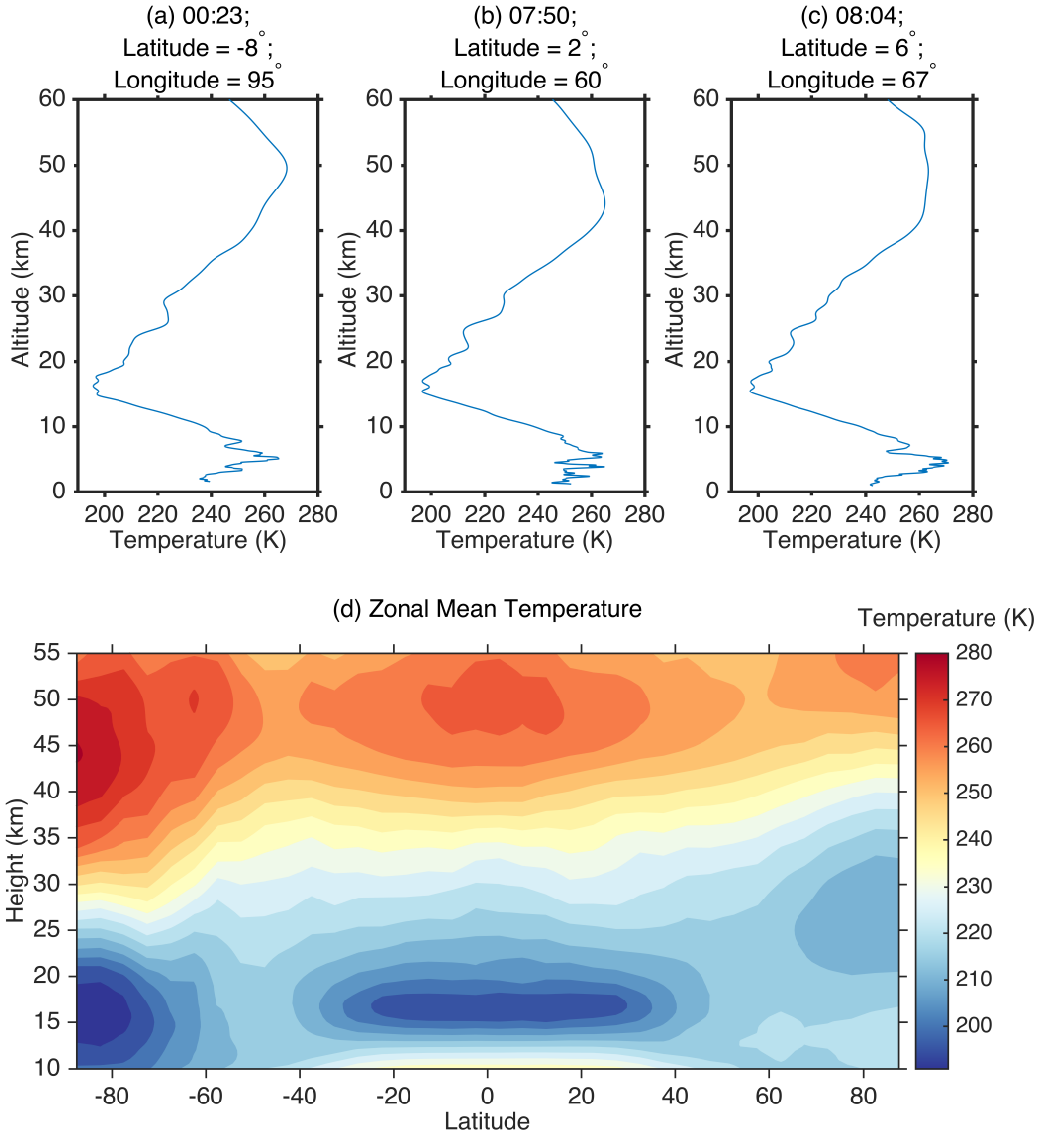

Figure 2.5: *Panels a-c present example low-latitude COSMIC RO temperature profiles recorded on the 6th October 2008. The times (UTC) and locations of the temperature profiles are included above each panel. Panel d presents zonal-mean temperature as a function of latitude and height from COSMIC RO observations, also on the 6th October 2008.*

An example of three low latitude COSMIC radio occultation temperature profiles are presented in panels a-c of Figure 2.5. These temperature profiles are typical of tropical latitudes with a cold-point tropopause of about 200 K at a height of approximately 15–20 km. This can also be seen in the panel d of Figure 2.5, which presents an example of daily zonal mean temperatures as a function of latitude and height. In panels a-c, the variability in temperature observed in the lower troposphere (< 10 km) results from water vapour in the atmosphere, which invalidates the dry atmosphere assumption.

In the example temperature profile shown in the left panel of Figure 2.5 the wave-like features that can be seen between approximately 15–30 km are a result of atmospheric waves. These atmospheric waves are a superposition of small-scale waves, such as gravity waves, and larger scale planetary waves, such as Kelvin waves. In the tropical lower stratosphere, Kelvin waves can have similar vertical wavelengths to gravity waves (Holton et al., 2001), and thus it is difficult to distinguish between the gravity-wave and Kelvin-wave contributions by simply filtering the profile. Instead, to isolate the gravity-wave perturbations, a background removal method must be applied that removes global-scale wave features. The method used in this work follows closely those used in other studies (e.g. Alexander et al., 2008a; Wang and Alexander, 2010), but uses a Fourier transform, rather than an S-Transform, for the removal of planetary-wave features. The method is summarised below.

1. The COSMIC RO temperature profiles are individually interpolated to constant height resolution of 2 km between heights of 10 km and 60 km.

2. Data are binned into daily $10^\circ \times 20^\circ$ latitude-longitude boxes in 1° steps. In this work, COSMIC data are used to study the influence of the MJO on gravity waves, which is a tropical phenomena. Thus, only tropical latitudes were considered, but this method could equally be applied at all latitudes.

3. The mean for each box is calculated at each height giving daily mean temperature for each grid box.

4. A Fourier transform is applied in longitude at each latitude and height.

5. An inverse Fourier transform is then applied at each latitude and height to determine the amplitude and phase of zonal wavenumber components $0-6$. This results in a background temperature field, which is comprised of a superposition of global-scale waves $1-6$ and the zonal mean state.

6. This background temperature profile containing the global-scale wave perturbations is interpolated to the location of each profile and is subtracted from the original temperature profile to leave just the small-scale perturbation profile, which we attribute to gravity waves (i.e. a profile of temperature perturbations as a function of height, for heights from 10 km to 60 km).

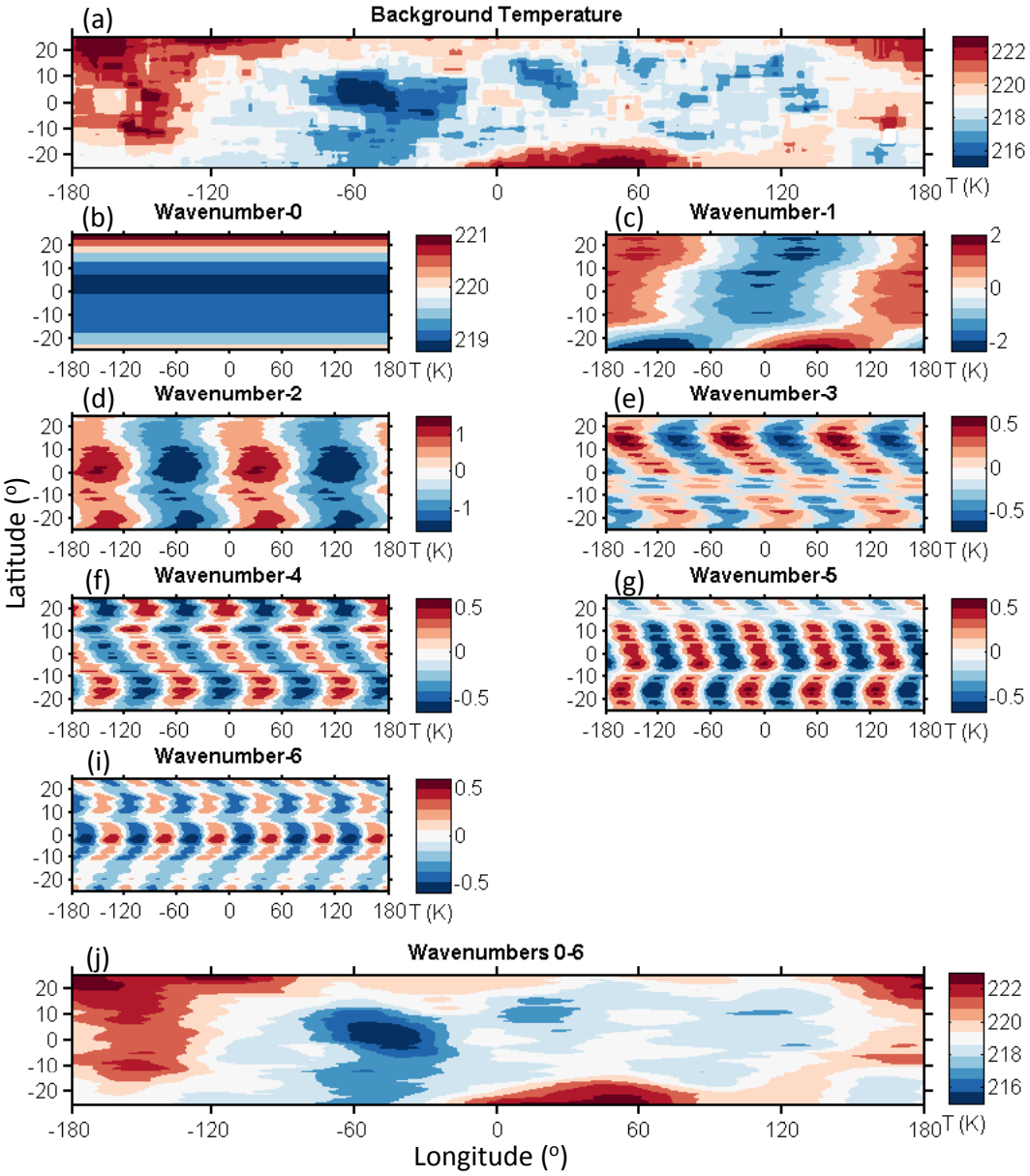

Figure 2.6: *An example of the results of the background temperature removal method, as described in steps 1–6, at a height of 26 km on the 15th July 2007. Panel a shows the daily mean temperature averaged over* $10° \times 20°$ *latitude-longitude boxes in* $1°$ *steps. Panels b-h present the individual contributions to the background daily mean temperature from global-scale features with zonal wavenumbers 0–6. Panel i shows the total contribution from wavenumbers 0–6.*

To determine the amplitude of gravity-wave features in the temperature pertubation profiles a Stockwell Transform (S-Transform) is applied (Stockwell et al., 1996). The S-Tranform is a spectral analysis technique, which provides spectral information about a signal in relation to its spatial variation (Stockwell et al., 1996). It has advantages over the Continuous Wavelet Transform (CWT) due to its direct connection to the Fourier Transform, and has a frequency invariant amplitude response and absolutely referenced phase information (Stockwell, 2007).

When applied to these profiles the S-Transform returns the amplitude of the wave features as a function of vertical wave number and height. As the data are interpolated to 2 km resolution we observe wave features with vertical wavelengths greater than 4 km. The maximum wave amplitude, T', is recorded at each height, z, and is converted to gravity wave potential energy (GWPE) per unit mass, E_p, using Equation 2.2.

$$E_p(z) = \frac{1}{2}\left(\frac{g}{N(z)}\right)^2\left(\frac{T'(z)}{\overline{T}(z)}\right)^2 \tag{2.2}$$

Where $\bar{T}$ is the background temperature, N is the Brunt-Väisälä frequency, and, g, the gravitational acceleration, is assumed to be constant.

In this work, GWPE measurements are used to determine the extent of the MJO modulation of the stratospheric gravity wave field. The results of this analysis are presented in Chapter 3, and are published in Geophysical Research Letters (Moss et al., 2016b).

2.2 Meteor Radars

2.2.1 Introduction

The mesosphere is notoriously difficult to measure and few techniques exist capable of making observations between the altitudes of $50 - 100$ km. The only in-situ measurements of this region are from rockets, but these only provide single soundings of this region and are too expensive for long-term use. Over recent decades it has become possible to investigate this region using remote-sensing instruments. These are both ground-based, including lidars, radars, imagers, and space-borne limb-sounding instruments. One such instrument is the meteor radar.

The concept of using radio measurements of meteors to study atmospheric motion was realised following early work predominantly on meteor physics (e.g. McKinley, 1961). This led to some of the first measurements of the MLT region and its dynamics (e.g. Greenhow and Neufeld, 1961). Development of radio meteor techniques in recent decades has since led to the availability of commercial meteor radars at a relatively low cost (Hocking et al., 2001).

Meteor radars are ground-based remote-sensing instruments and measure over a relatively small spatial area. However, they have good height resolution, excellent time resolution and are relatively inexpensive. They also require minimal maintenance and thus are well suited to campaigns and continuous operation in remote environments. Radio meteor measurements are not inhibited by weather or time of day, unlike lidars or all-sky imagers, meaning they provide near-continuous coverage.

This section will describe meteor measurements and the calculation of atmospheric properties from them. It will also describe meteor radar systems and specifically introduce the Ascension Island meteor radar, which is used in Chapter 4 to calculate winds, and gravity-wave properties in the mesosphere.

2.2.2 Radio Meteor Measurements

2.2.2.1 Meteoroids and Meteor Trails

Meteors are the luminous phenomena resulting from a particle of interplanetary material, a meteoroid, colliding with the Earth's atmosphere. Such interactions with

the Earth's atmosphere are primarily due to collisions rather than gravity, except in the case of very slow moving objects (Ceplecha et al., 1998). Meteors that can be observed by the naked eye result from meteoroids between approximately 5×10^{-5} m and 0.2 m diameter (Ceplecha et al., 1998). The majority of meteor trails detected by meteor radar are from meteoroids with a radius of less than 1 mm (Ceplecha et al., 1998).

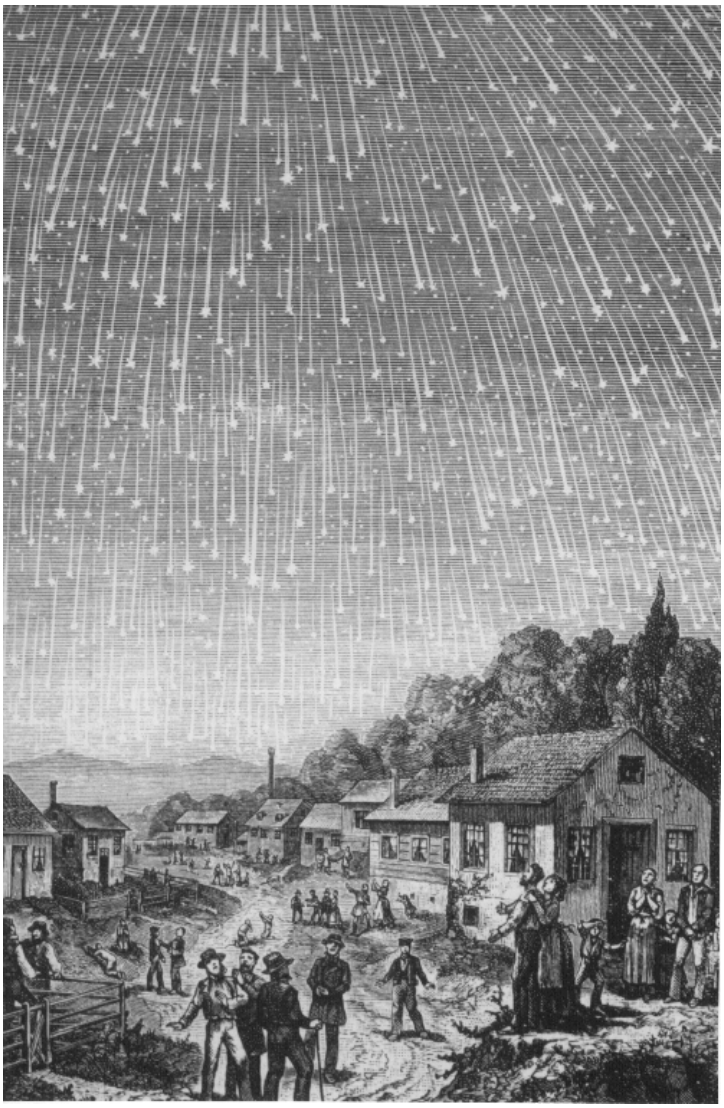

Figure 2.7: *Artist impression of the Leonid meteor storm on Wednesday 13th November 1833, produced by Karl Jauslin (1842-1904) and engraved by Adolf Vollmy (1864-1914). The scene was described to Karl Jauslin, a Swiss artist, by Joseph Harvey Waggoner (c1820 - 1889) and is the most famous of meteor shower pictures (Hughes, 1995). This event inspired the study of meteors by the astronomers of the day (Dick, 1998).*

Meteoroids enter the Earth's atmosphere at speeds of between 11 km s^{-1} and 73 km s^{-1}; the limits are imposed respectively by the Earth's escape velocity, and the sum of meteor velocities at 1 A.U. from the sun (43 km s^{-1}) and the Earth's orbital velocity (30 km s^{-1}) (Ceplecha et al., 1998). The rapid frictional heating that results from entry causes the surface to ablate when it reaches temperatures greater than 1850 K (Ceplecha et al., 1998). The visual light, which can be observed, mostly results from the de-excitation of the sublimated meteoroid atoms.

The atmospheric mean free path increases with height, and thus the meteor trail has a tapering cyclindrical shape with the greatest radius at its highest point (McKinley, 1961). The nature of this ionised trail is a function of entry speed, angle and the mass of the meteoroid particle. For a typical 40 km s^{-1} meteoroid, the trail will have an initial radius of approximately 0.3 m, 0.6 m, and 1.2 m at 75 km, 90 km and 105 km, respectively and will span around 10–15 km in height (see Table IX, Ceplecha et al., 1998).

2.2.2.2 Radio Measurements of Meteor Trails

The ablated meteoroid atoms undergo inelastic collisions with the surrounding air molecules, which produce a tapering cylindrical ionised trail that then moves with the local wind (Ceplecha et al., 1998). This plasma trail of charged particles and free electrons can specularly reflect radio waves. Using a radio pulse, the Doppler shift can be used to infer the radial velocity of the meteor with respect to the radar. Multiple receiver antennas allow interferometric determination of meteor locations in time and space.

The interaction of a radio signal with a meteor trail strongly depends on the electron line density of the meteor trails. The electron line density also depends on the mass and entry angle of the meteoroid. The interaction between the radio signal and meteor trail occurs by two distinct processes, known as underdense and overdense meteor echoes.

Underdense meteor echoes occur when the electron line density is less than approximately 10^{14} m^{-1}. For these echoes the radio signal will penetrate the trail and a fraction of the signal will be scattered. *Overdense meteor echoes* occur when the electron line density is greater than approximately 10^{14} m^{-1}. For overdense echoes the radio signal reflects from the meteor trails surface as if it were a solid metal.

During an underdense meteor echo, the radio echo will undergo an initial rapid rise in amplitude. The meteor trail radius will increase as a result of the diffusion of opposite charges interacting through an electric field, known as *ambipolar diffusion*. Within the first few seconds the radius becomes large enough that destructive interference will occur between the scatter at different depths. This process manifests itself as a sharp rise in amplitude followed by an exponential decay, as presented in Figure 2.8. The time of decay to half peak amplitude, $t_{\frac{1}{2}}$, is related to the ambipolar diffusion coefficient, D and the radio wavelength, λ, by Equation 2.3, where typical decay times are $\sim 0.1 - 1$ s (McKinley, 1961).

$$t_{\frac{1}{2}} = \frac{\lambda^2 \ln 2}{16\pi^2 D^2} \tag{2.3}$$

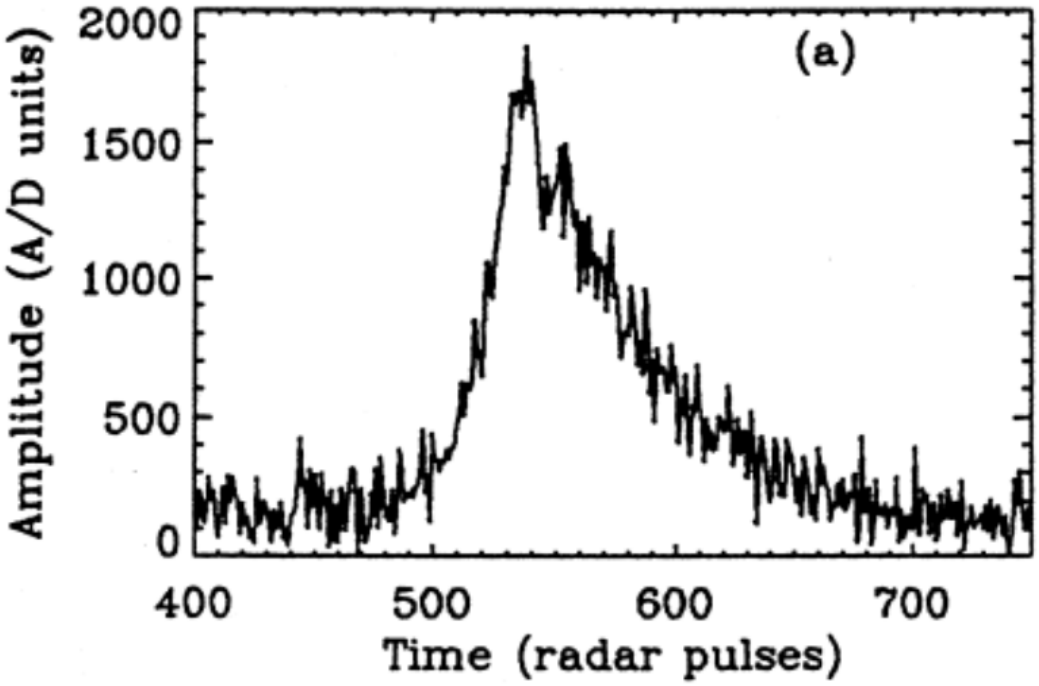

Figure 2.8: *Amplitude profile of a typical underdense meteor echo (duration 1.2 seconds) recorded by the Adelaide VHF radar at a range of 110 km and at an elevation of 60°, from Ceplecha et al. (1998).*

Overdense meteor echoes exist for a much longer duration. They are less useful as a result of the somewhat random echo amplitude fluctuations, which result from distortion by wind shears causing constructive and destructive interference from a number of specular reflection points. These are very much harder to distinguish from other undesirable signals, such as aircraft or lightning. Thus, meteor echoes are usually rejected if they do not have a characteristic underdense amplitude profile.

2.2.2.3 Radial Velocity Measurements from Underdense Meteor Echoes

The height range over which meteors can be detected is $\sim 75 - 100$ km. The lower height limit is imposed by the maximum size of meteroids that create underdense echoes ($\sim$ 1 mm), which have usually fully ablated by $\sim$ 75 km. The destructive interference that causes the exponential decay in amplitude of the meteor echo, as shown in Figure 2.8, limits the upper height of observations. At this height the meteor trail radius is sufficiently large that instantaneous destructive interference can occur. As the attenuation of the radio signal is a function of wavelength, the "underdense echo ceiling" depends on the specific wavelength used by the radar (McKinley, 1961). In addition, above $\sim$ 95 km the presence of electric and magnetic fields can distort the meteor trail, such as from anisotropic diffusion by magnetic fields (Ceplecha et al., 1998).

The specular reflection from the meteor trail needs the ionised trail to be orthogonal to the propagation direction of the radio pulse for some of the power to be reflected back to the receiver antennas. As a result only a small proportion of the meteors within the meteor radar's collecting volume are observed. The power flux incident on a meteor trail a distance, R, away from the radar transmitter is given by $\frac{P_T G}{4\pi R^2}$ W ms^{-2}, where P_T is the transmitted power, G is the antenna gain in the direction of transmission. Assuming the transmission and receiving antennas are identical, the absorbing area of the antenna is given by $\frac{G\lambda^2}{4\pi}$. Using this information the power received, P_R, from a model underdense meteor trail is given by Equation 2.4 (e.g. McKinley, 1961).

$$\begin{aligned} P_R =& \frac{P_T G^2 \lambda^3 \sigma_e}{128\pi^3 R^3}\left[\frac{C^2+S^2}{2}\right]q^2 \\ =& 2.5\times 10^{-32} P_T G^2 \left(\frac{\lambda}{R}\right)^3 \left[\frac{C^2+S^2}{2}\right]q^2 \end{aligned} \tag{2.4}$$

Where, q is the number of electrons per meter in the trail, σ_e is the scattering cross-section of a free electron, and $C = \int_{x_1}^{x} \cos\frac{\pi x^2}{2}dx$ and $S = \int_{x_1}^{x} \sin\frac{\pi x^2}{2}dx$ are the Fresnel integrals of optical diffraction theory and $C^2+S^2 = 2$ when evaluated along the whole trail.

The drifting of the meteor trail by a distance, d, results in the lengthening of the return path of the reflected signal by a distance 2d. If the drift distance was equivalent to half a wavelength, the observed phase change would be 2π radians as the return

path of the signal would have increased by one wavelength. Thus, a meteor trail drifting an arbitary distance, d, that reflects a radio wave of wavelength, λ, will have an observed phase change of $4\pi\frac{\mathrm{d}}{\lambda}$. Hence, the magnitude of the line-of-sight drift velocity, the radial velocity, v_{rad}, can be calculated from Equation 2.5:

$$v_{rad} = \frac{\Delta \mathrm{d}}{\Delta \mathrm{t}} = \frac{\lambda \Delta \phi}{4\pi \Delta \mathrm{t}} \tag{2.5}$$

2.2.2.4 Summary

Here we have introduced the measurements of meteor properties from radio echoes of meteor trails. In particular, we have introduced the measurements of underdense meteor echoes, which are useful for atmospheric measurements. We will now introduce meteor radars, and specifically SKiYMET systems. We will discuss these systems, their measurement characteristics and the determination of atmospheric properties from radial velocity measurements.

2.2.3 All-Sky Meteor Radars

2.2.3.1 SKiYMET Meteor Radars

SKiYMET meteor radars are all-sky radars produced on a commercial basis by Genesis Software and Mardoc Inc. The all-sky radar technique uses low-gain antennas to provide meteor coverage over a large volume around the radar. SKiYMET radars typically use a high pulse repetition frequency (PRF) of around $200-2000$ Hz. This high PRF allows meteor entrance speeds to be determined, but induces a smaller aliasing range of ~ 70 km. Pulse encoding is not usually used with these radars, thus it is not possible to tell which pulse is being reflected. For example, it is ambiguous whether a meteor detected at 80 km is actually at 80 km, 160 km, 240 km, etc. However, a priori knowledge of the underdense echo ceiling allows an unambiguous range to be determined (Hocking et al., 2001). The advantage and disadvantages of meteor radar observations are listed in Table 2.3. A full description of SKiYMET meteor radars can be found in Hocking et al. (2001) and a brief description is provided below.

The radar transmission frequency is in the range $25-60$ MHz. This operating frequency is chosen to be high enough that ionospheric scatter is not significant, while low enough that the meteor count rate is not greatly reduced by the lowering of the

underdense echo ceiling. The specific frequency chosen is based on the individual user preferences and where suitable gaps exist in the local radio frequency useage.

Advantages	Disadvantages
High resolution measurements of winds in the MLT region	Limited to single site locations
Measurements not dependent on the time of day or weather conditions	Limited vertical coverage
Excellent temporal resolution	Unable to resolve individual gravity waves
Cheap maintenance, thus highly suitable for long-term remote continuous operation	

Table 2.3: *Advantages and disadvantages of meteor radar measurements.*

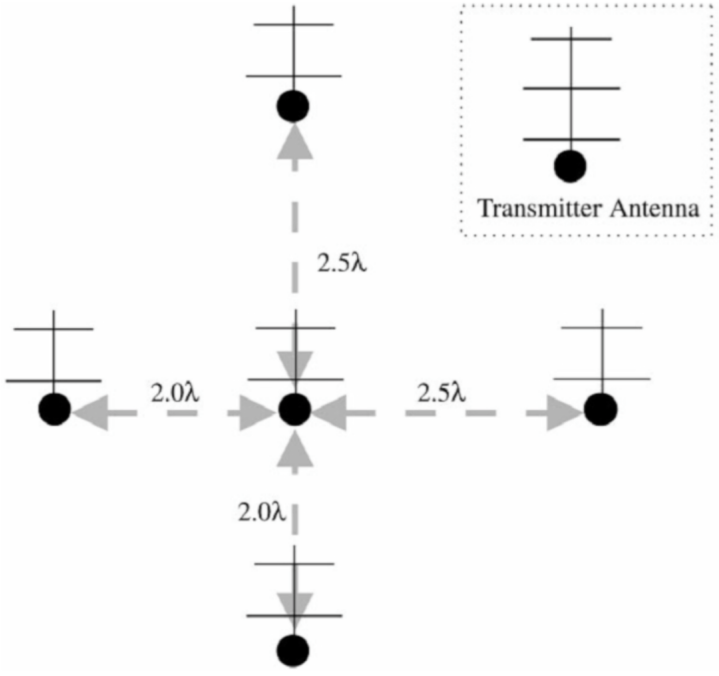

Figure 2.9: *The antenna arrangement of a typical meteor radar. Where, λ, is the transmitter wavelength. The five receiving antennas are arranged in an asymmetric cross with arms of either 2 or 2.5 wavelengths. The position of the transmitting antenna is arbitrary but should not be too close to any of the receiving antennas. Figure taken from Hocking et al. (2001).*

```
version 2.2
SITENAME ascension
LOCATION -8.0,-14.4
TIME_ZONE 0.000000
FREQUENCY(MHz)  43.500
LO_FREQUENCY(MHz)  48.500
CHANNELS 10
RESOLUTION(KM)    2.0
GATES  30
START_RGE(KM)    4.0
PRF  2144
ANTENNA_COORDS   13.78 360.00  17.23 180.00  17.23  90.00  13.78 270.00    .00 360.00
PHASE_OFFSETS   -13.50   -6.50    5.80  -21.10   26.40
INTEGRATIONS   4
RECORD_LENGTH  4.00
NSMOOTH  5
MINHT   70
MAXHT  110
RXLIST 1 1 1 1 1
RX_GAIN  115
TIME_ACCURACY HIGH
GPS_STATUS LOCK 7.952218 S 14.383133 W
VEL_ERR_LIM  5.50
SN_ACCEPT_RATIO  2.00
T_DECAY_MAX  2.00
PLANE_NORMAL    .00    .00
PULSE_CODE 1
MODE I
  Date        Time       File   Rge     Ht     Vrad   delVr  Theta  Phi0 Ambig Delphase ant pair  IREX amax  Tau  vmet  snrdb
 2006/12/21  0:01:08.099 00004 157.9  100.2  -46.72    .14 | 51.2   194.0  1     4.5     24        1   9649.  .036 -9.99  25.1
 2006/12/21  0:01:50.657 00006 108.0   85.5  -26.50   5.24   37.9   265.0  1    17.9     23        1   1356.  .091 -9.99   7.0
 2006/12/21  0:01:50.657 00007 106.0   83.9  -22.16   1.67   37.9   265.5  1     5.9     25        1   2403.  .087 -9.99  12.9
 2006/12/21  0:02:13.233 00008 187.9   97.0   65.60   1.34   59.7   296.2  1    13.4     14        1   3613.  .034 -9.99  16.3
 2006/12/21  0:02:34.571 0000A 237.9   89.2  -20.57   4.04   69.0   172.8  1    14.6     23        1   2118.  .036 -9.99  12.0
 2006/12/21  0:02:36.101 0000B 167.9   81.6  -47.62    .76   61.6   265.7  1     7.3     15        1   2095.  .156 -9.99  11.3
 2006/12/21  0:02:36.050 0000C 165.9   80.3  -47.01    .11   61.7   265.8  1     4.5     15        1   5836.  .146  8.13  20.7
 2006/12/21  0:03:05.461 0000D 132.0   91.8   11.93    .15   46.3   208.0  1     4.4     35        1   6291.  .069 -9.99  21.1
 2006/12/21  0:03:05.461 0000E 130.0   90.3   11.82    .29   46.4   208.0  1     4.5     35        1   5036.  .069 -9.99  19.3
```

Figure 2.10: *An example of the format of a typical meteor position data (MPD) file from the Ascension Island Meteor Radar, recorded on the 21st December 2006. Details of the recorded parameters are listed in Table 2.4.*

Figure 2.9 presents the arrangement of antennas in a SKiYMET system. The system is made up of a three-element Yagi transmitter antenna and five two-element Yagi receiver antennas arranged as an interferometer. This interferometer pattern gives receiver phase differences, which, with knowledge of the range, allows the specular reflection point on the meteor trail and its properties to be accurately determined. The typical accuracy of azimuth and zenith angles is of order $0.5 - 1^{\circ}$.

Real-time detection, confirmation and analysis of meteor echoes and parameters is done by an on-site PC and stored in a meteor position data (MPD) file (Hocking et al., 2001). Each daily MPD file includes details of the radar operation parameters in the header lines followed by the data for the parameters described in Table 2.4. An example of a typical MPD file is presented in Figure 2.10.

Parameter	Description
Date	The date of detection relative to UTC (yyyy/mm/dd)
Time	The time of detection (HH:MM:SS.XYZ) where XYZ is the millisecond of the detection
File	The file name extension used to store the raw data for this detection
Rge	The range of the detection in km
Ht	The corrected height above ground of the detection in km
Vrad	The radial drift velocity of the trail in ms^{-1}
DelVr	The standard deviation of the radial velocity measurement obtained from the 5 antenna pairs in the interferometer. Data with delVr $>$ 5.5 ms^{-1} are automatically rejected and represent a limiting value for this field in the MPD file
Theta	The zenith angle of the detection in degrees
Phi0	The azimuth angle of the detection in degrees (North from East)
Ambig	The number of locations this detection could have originated from
Delphase	The worst phase error between antennas if the measured azimuth and zenith of the detection are correct in degrees
ant pair	The antenna pair with the worst phase error
IREX	The receiver channel used in the analysis for certain single-channel data quality tests (Always "1" during normal operation)
amax	The peak value of the amplitude of the meteor echo in digital units
Tau	The decay time (half-life) of the meteor in seconds
vmet	The entrance speed of the meteor in kms^{-1}. Bad values are specified by "-9.99"
snrdb	The signal-to-noise ratio for this meteor

Table 2.4: *Parameters routinely measured by the Ascension Island meteor radar and included in daily meteor position data files.*

2.2.3.2 The Spatial and Temporal Distribution of Detected Meteors

An example of the spatial and temporal distribution of meteors is presented in Figure 2.11. These figures are produced from observations made by the Ascension Island meteor radar and are typical for meteor radars, except for the diurnal cycle, which is more prominent at low latitudes.

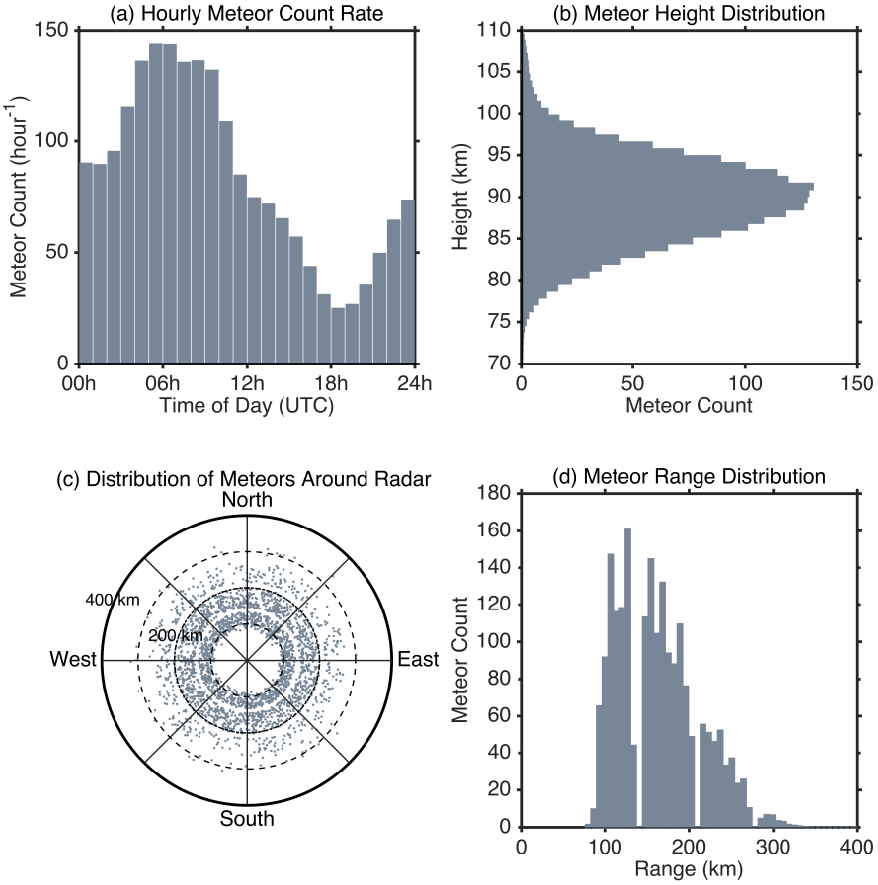

Figure 2.11: *Spatial and temporal distribution of meteors from the Ascension Island meteor radar in 2006. (a) Histogram of hourly meteor count rates over a composite day in 2006. A clear diurnal cycle is observed with a peak at 0600 UTC and a minima at 1800 UTC. (b) Histogram of meteor count as a function of height for 2006 (100 bins). (c) Azimuthal distribution of meteors on 7th January 2006. (d) Histogram of meteor count against range for 2006. Gaps occur in (c) and (d) at specific ranges due to the pulse transmission of the radar (see text).*

Figure 2.11a presents the mean temporal variation of meteor counts from Ascension Island for a day in 2006. A clear diurnal cycle is observed with the largest meteor count at 0600 UTC and smallest meteor count at 1800 UTC. This cycle results from a combination of the Earth's rotation and orbit. Any position on the Earth in the leading hemisphere encounters a greater numbers of meteors, which are 'swept up' by

the Earth's motion. In contrast, for any position on the Earth's trailing hemisphere, the meteors are 'chasing' the Earths motion and only the faster meteors can catch up. This effect is particularly apparent at low latitudes.

The distribution of meteors detected as a function of height using all meteors from 2006 is presented in Figure 2.11b. Height measurements are made using the elevation angle and range measured by the radar for each meteor echo and an adjustment is applied to take account of the curvature of the earth. A characteristic Gaussian distribution is observed with a peak at ~ 90 km and very few meteors are observed beyond 80 km and 100 km. All meteors are detected between approximately $75 - 110$ km due to the underdense echo ceiling at greater heights and meteor ablation at lower heights, as discussed in section 2.2.2.2.

SKiYMET meteor radars are all-sky systems, so the transmitted power from the transmitting antenna is largely independent of azimuth. This allows detection of meteors at all azimuth angles, and results in an approximately even azimuthal distribution of detected meteors as shown in Figure 2.11c.

No meteors are detected directly above the radar (near the zenith). This geometric effect is due to the specular reflection of radio waves from the meteor trails. For meteors at very small zenith angles to be detected would require the meteoroid to be travelling near-horizontal through the atmosphere. This would require a very long travel distance through the atmosphere and even the largest of meteoroids would have completely ablated by the time they reached the zenith.

Concentric rings with no meteors are observed in the azimuthal distribution. This is a result of the pulse transmission of the radar. Meteors do occur in these locations but are not detected as the receivers are turned off during the outgoing direct wave in transmission, which otherwise would cause saturation of the recievers and potentially damage the equipment. Thus, meteors are not detected at ranges that correspond to these times.

Figure 2.11d presents the range distribution of meteors. As in Figure 2.11c, the specific ranges that meteors are not detected is evident at approximately ~ 140 km, 210 km, and 280 km. Very few meteors are detected at ranges less than approximately 90 km. This results from a combination of the minimum height and zenith angles for detection. The range distribution peaks at approximately 120 km, beyond which the number of meteors detected falls off with increasing range as echo strength decays rapidly as a function of distance (i.e. Equation 2.4).

2.2.3.3 Meteor Radar Wind Measurements

To obtain estimates of the mean wind averaged over the collecting volume of the radar from meteor radial velocities, the following is assumed:

1. The vertical velocities in the MLT region are much smaller than the horizontal velocities. This assumption is justified as the horizontal winds are at least an order of magnitude larger than the vertical winds (e.g. Mitchell and Howells, 1998).

2. Within a given height range, the air in the meteor collecting volume moves as a uniform slab. This is valid for motions that have scales much larger than the meteor collecting volume (i.e. > 400 km).

Based on these assumptions, mean winds can be calculated provided that enough meteor measurements are available. For typical meteor count rates, one hour provides enough meteors for a wind determination and thus defines the time resolution to be typically this value. To be used in the calculation, a meteor must have an echo decay time, Tau, greater than 0.015 s to reject any short-lived noise spikes. Additionally, there must be no ambiguity in the meteor position. Typically meteors with zenith angles less than 15° are not used in wind calculations as the vertical motions become more significant, and errors in the inferred horizontal component become too large. Radial velocity measurements that have an error greater than 5.5 ms^{-1} are not used.

The radial velocity, v_{rad}, is assumed to be a component of a purely horizontal flow. The inferred line-of-sight horizontal velocity, v_h, is thus given by Equation 2.6.

$$v_h = \frac{v_{rad}}{sin(\alpha)} \tag{2.6}$$

where the adjusted zenith angle, α, is given by the curved-Earth correction shown in Equation 2.7.

$$\alpha = cos^{-1}\left(\frac{(R_E + h)^2 + R^2 - R_E^2}{2R(R_E + h)}\right) \tag{2.7}$$

h is the true height of the meteor, R_E is the Earth's radius and R is the slant range to the meteor. Any meteor with an inferred line-of-sight horizontal velocity greater than 200 ms^{-1} is rejected as an outlier.

To calculate atmospheric mean winds meteors are binned into height gates. In this thesis the height gates used are $(78-83)$, $(83-86)$, $(86-89)$, $(89-92)$, $(92-95)$ and $(95-100)$ km, but these can be adjusted provided enough meteors are present in each height gate to accurately determine the winds. The lowermost and uppermost height gates are wider to ensure enough meteors are present to produce accurate wind measurements.

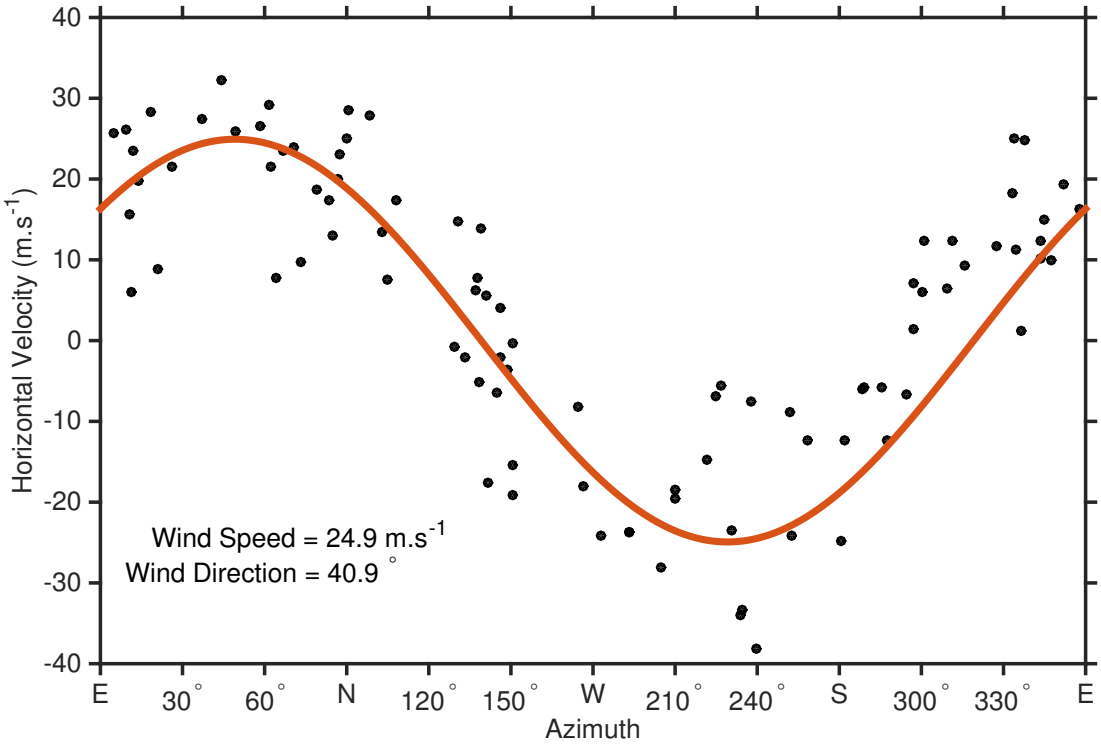

Figure 2.12: *Line-of-sight component of the inferred horizontal velocity plotted as a function of azimuth for all meteors recorded (black dots) by the Ascension Island meteor radar between 0600 UTC and 0800 UTC on the 11th June 2006 at heights between $89-92$ km. The overlaid red line is the best fit sine wave that gives the magnitude and direction of the wind. The measured wind speed and wind direction is displayed in the bottom left hand corner of the figure.*

To determine hourly winds a least-squares fit is applied to the radial velocities. This minimises the sum of the differences between the inferred line-of-sight horizontal velocities and a fitted sine wave. The amplitude and phase of this sine wave then gives the magnitude and direction of the mean wind, which can be decomposed into its zonal and meridional components. This analysis is demonstrated in Figure 2.12 for a wind measurement calculated from meteors in the $89-92$ km height gate between 0600 UTC and 0800 UTC on 11th June 2006.

As an example of the results of this analysis, Figure 2.13 presents the zonal and

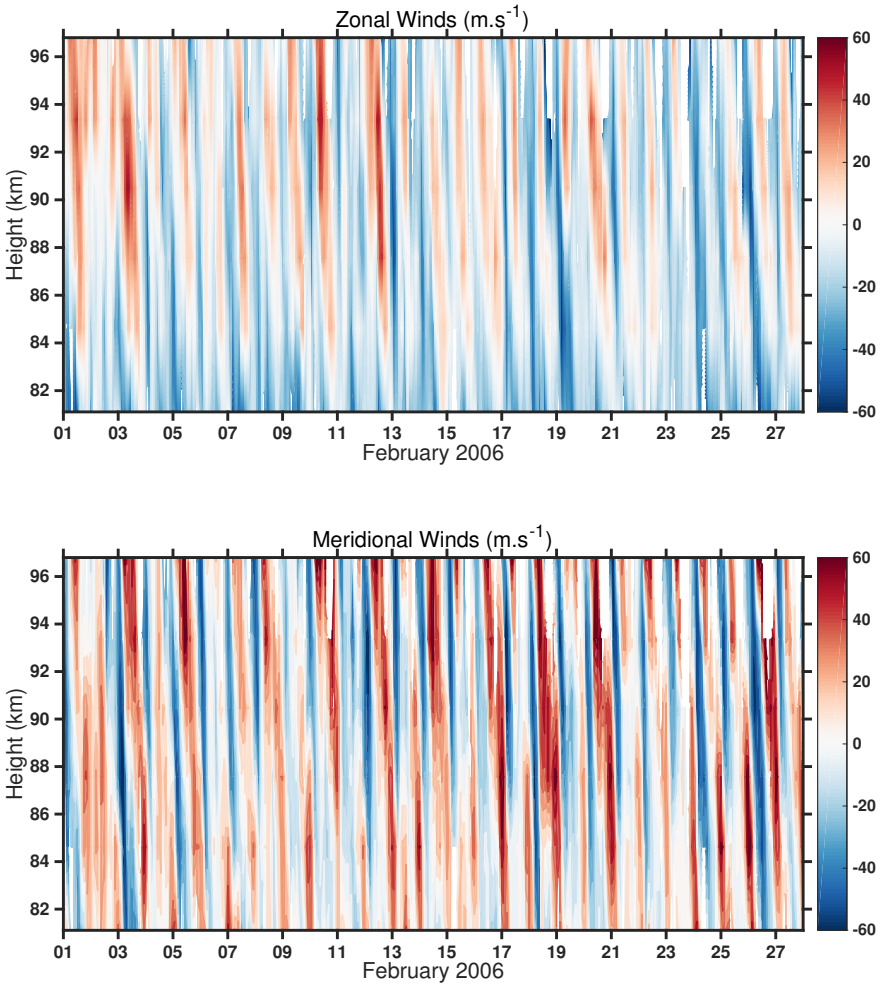

Figure 2.13: *Zonal (top) and Meridional (bottom) hourly winds over Ascension Island (8° S, 14° W) in February 2006. A clear, large amplitude 24-hour tidal signature is observed, with amplitudes that tend to be larger at greater heights.*

meridional components of the horizontal winds for February 2006. A clear diurnal tidal signature can be observed in both the zonal and meridional components. Tides dominate the variability in the MLT region at most latitudes. Low-pass filtering can be applied to remove the strong tidal signature and reveals longer period variability in the mean winds.

2.2.3.4 Meteor Radar Measurements of Gravity-Wave Variance and Momentum Flux

Very few methods exist for measuring gravity-wave properties in the mesosphere. Most of the early measurements utilised the method of Vincent and Reid (1983),

using dual beam radars (e.g. Reid and Vincent, 1987). However, these measurements tend to have limited seasonal and height coverage. The Hocking (2005) method of calculating gravity-wave variances and momentum fluxes from all-sky meteor radars was developed to take advantage of the large existing global network of meteor radars that are all of a similar design, and thus very suitable for inter-comparison studies. This method builds on the dual beam method (Vincent and Reid, 1983) and is similar to the medium-frequency interferometric method of Thorsen et al. (1997), but differs in its application.

The major advance made in the Hocking (2005) method is recognising that the dual beam technique can be extended to all-sky meteor measurements. In principle, meteor radars could be used by sampling the meteors to replicate a two-beam instrument, however in practice meteor counts from all-sky systems are too low for this. The Hocking (2005) method thus generalises for an all-sky summation, whereby the two-beam technique is a special case.

Fundamentally, the determination of gravity-wave variances and momentum fluxes from meteor measurements assumes the scatter of the individual inferred line-of-sight horizontal velocities around the fitted sine wave, as shown in Figure 2.12, are due to gravity waves. This statistical method relies on accurate mean winds being determined so that it can be assumed that the difference between the radial velocity of each meteor, v_{rad}, and the mean radial velocity expected for uniform winds, v_{radm}, is due to gravity waves alone. Thus, it is assumed that the calculated background winds include the contribution of the mean flow and other large-scale processes, such as tides, planetary waves or gravity waves with long horizontal wavelengths.

We will now consider the method of determining gravity-wave variances and momentum fluxes from meteor measurements. Following the Hocking (2005) method, we need to minimise Λ, where Λ is given by

$$\Lambda = \sum [(v'_{rad})^2 - (v'_{radm})^2]^2 \tag{2.8}$$

The summation in Equation 2.8 is over all meteors within the time and height bin. The difference between the measured and modelled radial velocities, v'_{rad}, and the component of the modelled radial velocity due to wave motion, v'_{radm}, are as follows

$$v'_{rad} = v_{rad} - v_{radm} \tag{2.9}$$

$$
\begin{aligned}
v'_{radm} &= u' \sin\theta \cos\phi \\
&+ v' \sin\theta \sin\phi \\
&+ w' \cos\theta
\end{aligned}
\tag{2.10}
$$

Substitution of Equation 2.10 into Equation 2.8 yields

$$
\begin{aligned}
\Lambda = \sum [(v'_{rad})^2 &- u'^2 \sin^2\theta \cos^2\phi \\
&+ v'^2 \sin^2\theta \sin^2\phi \\
&+ w'^2 \cos^2\theta \\
&+ 2u'v' \sin^2\theta \sin\phi \cos\phi \\
&+ 2u'w' \sin\theta \cos\theta \cos\phi \\
&+ 2v'w' \sin\theta \cos\phi \sin\phi]^2
\end{aligned}
\tag{2.11}
$$

To minimise Λ the partial derivatives of Equation 2.11 with respect to u'^2, v'^2, w'^2, $u'v'$, $u'w'$ and $v'w'$ are taken and set to 0. The final result of this is a matrix equation, Equation 2.12, which can easily be inverted to give estimates for the 6 parameters, $\overline{u'^2}$, the zonal variance, $\overline{v'^2}$, the meridional variance, $\overline{w'^2}$, the vertical variance, $\overline{u'v'}$, the meridional flux of zonal momentum (and also the zonal flux of meridional momentum), $\overline{u'w'}$, the vertical flux of zonal momentum, and $\overline{v'w'}$, the vertical flux of meridional momentum, where the bar indicates the average over the time and spatial collecting volume.

$$
\begin{bmatrix}
\Sigma\sin^4(\theta)\cos^4(\phi) & \Sigma\sin^4(\theta)\cos^2(\phi)\sin^2(\phi) & \Sigma\sin^2(\theta)\cos^2(\theta)\cos^2(\phi) & \Sigma 2\sin^4(\theta)\cos^3(\phi)\sin(\phi) & \Sigma 2\sin^3(\theta)\cos(\theta)\cos^3(\phi) & \Sigma 2\sin^3(\theta)\cos(\theta)\cos^2(\phi)\sin(\phi) \\
\Sigma\sin^4(\theta)\cos^2(\phi)\sin^2(\phi) & \Sigma\sin^4(\theta)\sin^4(\phi) & \Sigma\sin^2(\theta)\cos^2(\theta)\sin^2(\phi) & \Sigma 2\sin^4(\theta)\sin^3(\phi)\cos(\phi) & \Sigma 2\sin^3(\theta)\cos(\theta)\sin^2(\phi)\cos(\phi) & \Sigma 2\sin^3(\theta)\cos(\theta)\sin^3(\phi) \\
\Sigma\sin^2(\theta)\cos^2(\theta)\cos^2(\phi) & \Sigma\sin^2(\theta)\cos^2(\theta)\sin^2(\phi) & \Sigma\cos^4(\theta) & \Sigma 2\sin^2(\theta)\cos^2(\phi)\cos(\phi)\sin(\phi) & \Sigma 2\cos^3(\theta)\sin(\theta)\cos(\phi) & \Sigma 2\cos^3(\theta)\sin(\theta)\sin(\phi) \\
\Sigma 2\sin^4(\theta)\cos^3(\phi)\sin(\phi) & \Sigma 2\sin^4(\theta)\sin^3(\phi)\cos(\phi) & \Sigma 2\sin^2(\theta)\cos^2(\theta)\cos(\phi)\sin(\phi) & \Sigma 4\sin^4(\theta)\cos^2(\phi)\sin^2(\phi)\sin(\phi) & \Sigma 4\sin^3(\theta)\cos(\theta)\cos^2(\phi)\sin(\phi) & \Sigma 4\sin^3(\theta)\cos(\theta)\sin^2(\phi)\cos(\phi) \\
\Sigma 2\sin^3(\theta)\cos(\theta)\cos^3(\phi) & \Sigma 2\sin^3(\theta)\cos(\theta)\sin^2(\phi)\cos(\phi) & \Sigma 2\cos^3(\theta)\sin(\theta)\cos(\phi) & \Sigma 4\sin^3(\theta)\cos(\theta)\cos^2(\phi)\sin(\phi) & \Sigma 4\sin^2(\theta)\cos^2(\theta)\cos^2(\phi) & \Sigma 4\sin^2(\theta)\cos^2(\theta)\cos(\phi)\sin(\phi) \\
\Sigma 2\sin^3(\theta)\cos(\theta)\cos^2(\phi)\sin(\phi) & \Sigma 2\sin^3(\theta)\cos(\theta)\sin^3(\phi) & \Sigma 2\cos^3(\theta)\sin(\theta)\sin(\phi) & \Sigma 4\sin^3(\theta)\cos(\theta)\sin^2(\phi)\cos(\phi) & \Sigma 4\sin^2(\theta)\cos^2(\theta)\cos(\phi)\sin(\phi) & \Sigma 4\sin^2(\theta)\cos^2(\theta)\sin^2(\phi)
\end{bmatrix}
\begin{bmatrix}
u'^2 \\ v'^2 \\ w'^2 \\ u'v' \\ u'w' \\ v'w'
\end{bmatrix}
=
\begin{bmatrix}
\Sigma {v'_{rad}}^2 \sin^2(\theta)\cos^2(\phi) \\
\Sigma {v'_{rad}}^2 \sin^2(\theta)\sin^2(\phi) \\
\Sigma {v'_{rad}}^2 \cos^2(\theta) \\
\Sigma {v'_{rad}}^2 \sin^2(\theta)\cos(\phi)\sin(\phi) \\
\Sigma {v'_{rad}}^2 \sin(\theta)\cos(\theta)\cos(\phi) \\
\Sigma {v'_{rad}}^2 \sin(\theta)\cos(\theta)\sin(\phi)
\end{bmatrix}
\tag{2.12}
$$

A growing body of studies have applied the Hocking (2005) method to other meteor radars around the world (e.g. Fritts et al., 2010; Vincent et al., 2010; Fritts et al., 2012; Andrioli et al., 2013a; de Wit et al., 2014; Placke et al., 2015). The gravity-wave momentum fluxes presented in Chapter 4 of this thesis (and published in Moss et al. (2016a)) are the first measurements of momentum fluxes made using the Ascension Island meteor radar and some of the few such measurements available in the tropical mesosphere. We will now introduce the Ascension Island meteor radar system.

2.2.4 The Ascension Island Meteor Radar

The University of Bath has operated a number of commercially produced SKiYMET meteor radars since the first of these was installed at the Esrange Space Centre, near Kiruna, Sweden, in August 1999. The locations and operation periods of these meteor radars are presented in Table 2.5 and presented in Figure 2.14.

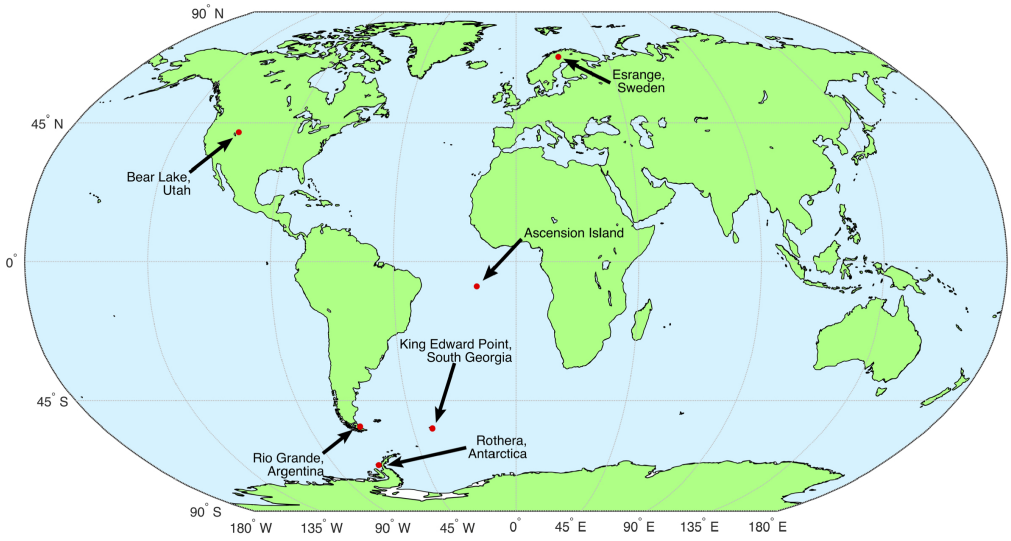

Figure 2.14: *The University of Bath's meteor radar network*

In this thesis, data from the meteor radar on Ascension Island are used. Ascension Island is a small equatorial volcanic island in the South Atlantic Ocean. The site is of particular interest due to its low-latitude and oceanic location. Thus, it can provide observations of gravity waves that will have originated from purely convective sources.

Meteor Radar	Location	Operation Period
Ascension Island	8° S, 14° W	May 2001 to August 2012
Bear Lake	42° N, 111° W	March 2008 to January 2014
Esrange	68° N, 21° E	August 1999 to present
Rothera	68° S, 68° W	February 2005 to present
Rio Grande*	54° S, 58° W	February 2008 to present
South Georgia	54° S, 37° W	February 2016 to present

Table 2.5: *The locations and operation period of the University of Bath meteor radar network. This network is designed to provide coverage at a number of key latitudes. * The Rio Grande meteor radar is owned in collaboration with other institutions, where the University of Bath is the junior partner.*

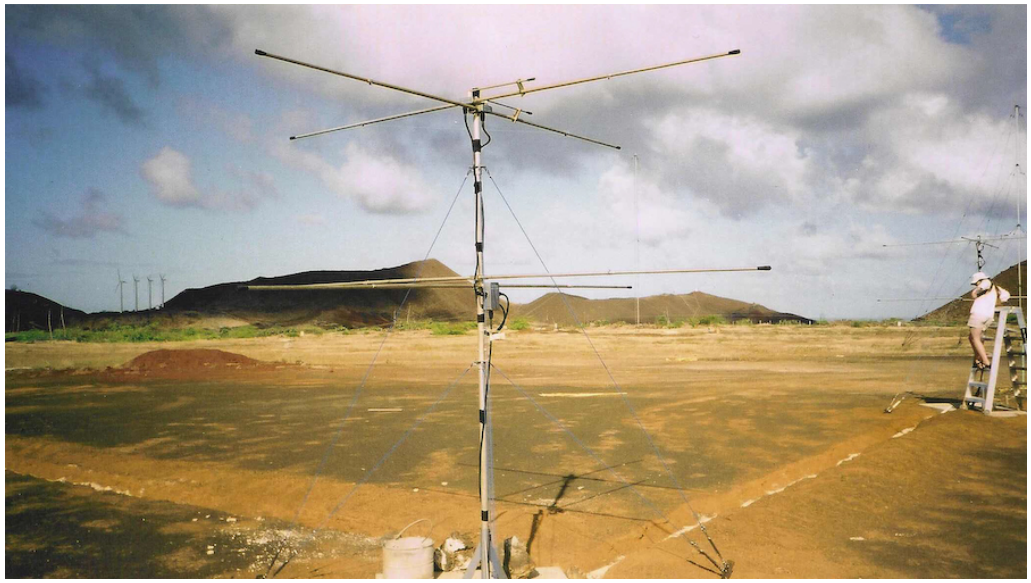

Figure 2.15: *Receiver antenna at the Ascension Island meteor radar (8° S, 14° W) site.*

A picture of a receiver antenna from the Ascension Island meteor radar site is shown in Figure 2.15. The meteor radar was installed in May 2001 and data are available from then until August 2012. It operated in an all-sky configuration with a peak power of 12 kW up until 2007, after which it was switched to 6 kW. It transmits at a frequency of 43.5 MHz. Due to difficult operating conditions on the island, the

radar has had periods of downtime during its lifetime. Most noticeably, large gaps are present from December 2003 to May 2004, April 2007 to February 2009 and July 2011 to July 2012. A summary of the data availability of the Ascension Island meteor radar, from Day and Mitchell (2013), is presented in Figure 2.16.

Despite these difficulties, data from this radar have been successfully used to study a range of atmospheric processes in the mesosphere. This has included studies of atmospheric tides (Sandford et al., 2007; Sandford and Mitchell, 2007; Davis et al., 2013), intra-seasonal and inter-annual oscillations (Rao et al., 2009; de Wit et al., 2013; Day and Mitchell, 2013; Moss et al., 2016a) and planetary waves (Pancheva et al., 2004; Younger and Mitchell, 2006; Davis et al., 2012). In Chapter 4 of this thesis and associated publication (Moss et al., 2016a), observations made by the Ascension Island meteor radar are used for the first time to study gravity waves in the equatorial mesosphere.

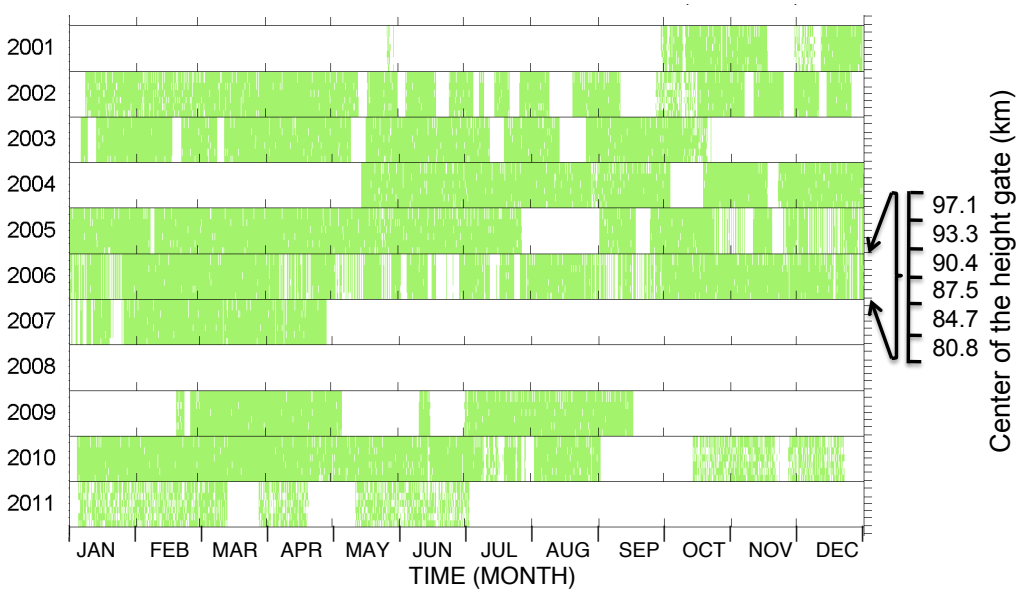

Figure 2.16: *Summary of the data availability from the Ascension Island meteor radar (8° S, 14° W).*

2.3 Other Supporting Observations

2.3.1 The Tropical Rainfall Measuring Mission

The Tropical Rainfall Measuring Mission (TRMM) provides a comprehensive data-set on tropical rainfall between 50° N and 50° S (Huffman et al., 2007). It is the first Earth Science mission dedicated to the study of topical and subtropical rainfall. The satellite was launched on November 27th 1997 as a joint mission between NASA and JAXA, the Japanese space agency, and ceased operating on April 8th 2015 when the spacecraft depleted its fuel reserves. The TRMM mission has now been superseded by the Global Precipitation Measurement (GPM) mission, which launched in February 2014 and covers all latitudes.

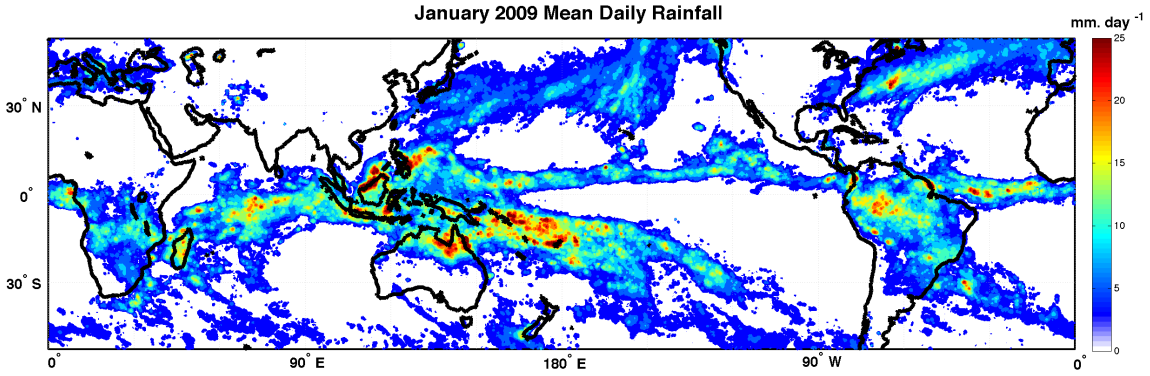

Figure 2.17: *An example of TRMM 3B42 daily precipitation data averaged over January 2009.*

In this thesis the TRMM multi-satellite precipitation analysis 3B42 data-set is used as a proxy for latent heat release (and so as a proxy for the convective sources of gravity waves). The data are a measure of the total daily precipitation total in mm and is on a $0.25° \times 0.25°$ latitude-longitude grid. It is derived by calibrating data from various geostationary satellites, such as the Geostationary Operational Environmental Satellite (GOES) and Meteosat satellites, with TRMMs (Tropical Rainfall Measurement Mission) microwave imager (TMI) and visible and infra-red scanner (VIRS) instruments. Figure 2.17 shows an example of daily precipitation averaged over January 2009 for the 3B42 TRMM data-set.

2.3.2 Outgoing Long-wave Radiation

Outgoing long-wave radiation (OLR) is a measure of the amount of energy emitted by the Earth to space. The contribution of this energy is important to the Earth's radiation budget. Deep cloud cover over a particular region will lead to measurements representing the amount of the radiation emitted at the cloud-top. As warmer objects emit more radiation than cooler objects, high cloud tops will lead to regions of lower OLR. Thus, in the tropics, OLR measurements provide an excellent proxy for convective activity and rainfall, which are known to be a strong source of gravity waves.

The National Oceanic and Atmospheric Administration (NOAA) Interpolated OLR dataset is used in this thesis and is available the from their website. The daily data provides global coverage of OLR on a $2.5° \times 2.5°$ latitude-longitude grid. Data are pre-processed and any gaps are filled using temporal and spatial interpolation as discussed in Liebmann and Smith (1996). Data are available from June 1974 to present.

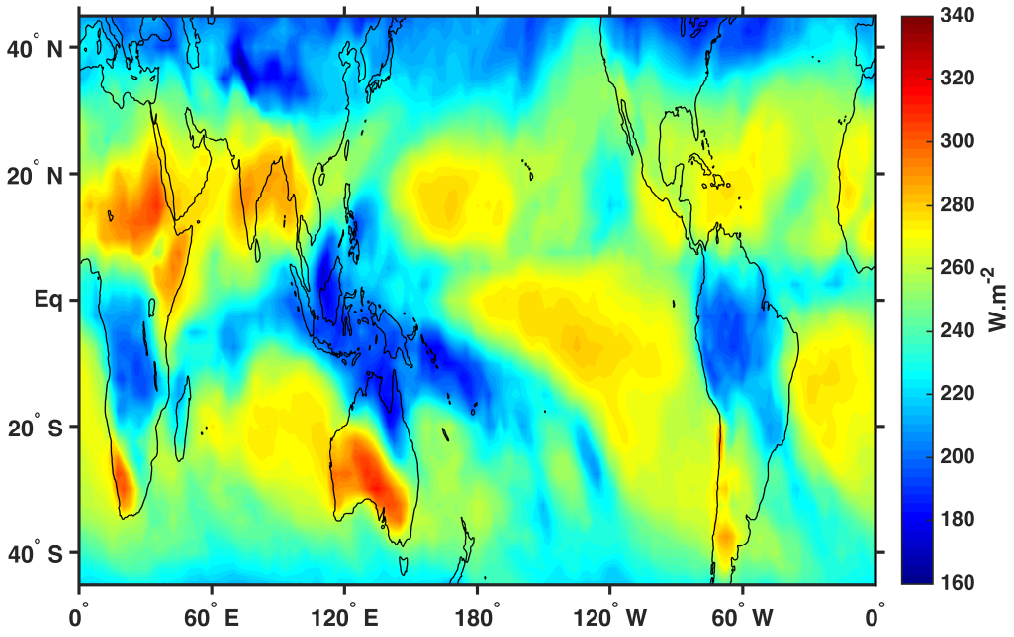

Figure 2.18: *An example of outgoing long-wave radiation data averaged over January 2009.*

A monthly mean map of OLR is presented in Figure 2.18 for January 2009; a clear connection between the rainfall data presented in Figure 2.17 and OLR can be seen. N.B. low areas of OLR (blue) are cooler regions indicative of high cloud tops and greater convective activity.

2.3.3 ECMWF Reanalysis Data

Reanalysis datasets are produced by assimilating historic data into a modern model to provide a dynamically consistent estimate of the atmospheric conditions at each point in time. These global datasets have excellent spatial and temporal resolution and incorporate huge amounts of data. While these data provide a great opportunity to study the atmosphere as a whole, they should be used with caution. In particular, the number, variety and location of the assimilated observations can induce biases and artificial variability. However, particularly on longer time-scales, these data provide a good estimate of the atmospheric variability.

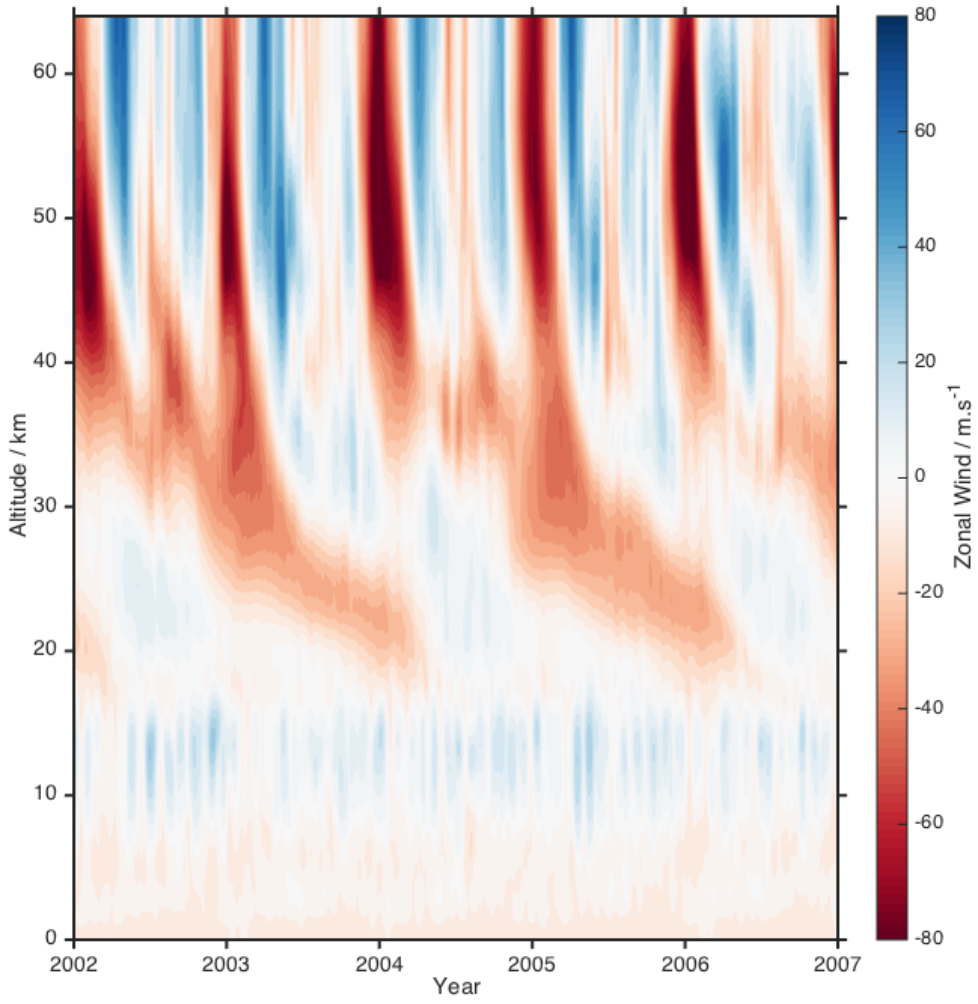

Figure 2.19: *ECMWF reanalysis monthly-smoothed zonal winds averaged over a* 5° *box centred on Ascension Island (*8° *S,* 14° *W) between 2002 and 2007. The characteristic quasi-biennial and semi-annual oscillations are readily apparent in the stratosphere and mesosphere, respectively.*

In this work, the European Centre for Medium Range Weather Forecasting (ECMWF) operational analysis data set is used to investigate the zonal-wind structure of the atmosphere. The data used are from the 1.125° resolution data-set, available from 2000 to present. Data are available at heights of up to 64 km until February 2006 when the model was extended to 80 km. Very little observational data is assimilated into the model above 40 km, and thus the ECMWF data should be treated with caution above this height. A more complete description of the ECMWF reanalysis data can be found in the review by Dee et al. (2011) and references therein. An example of ECMWF zonal winds over Ascension Island is shown in Figure 2.19.

2.4 The Real-time Multivariate MJO Index

The MJO dominates the intra-seasonal variability in the tropical troposphere. It is not unusual for large scale atmospheric processes to be described by indices that characterise their state (amplitude and phase) as a function of time. In this work the state of the MJO is defined using the Real-time Multivariate (RMM) MJO index of (Wheeler and Hendon, 2004).

The RMM index is defined by the combination of equatorially-averaged (15° N and 15° S) anomalies of OLR and zonal-wind at 850 hPa and 200 hPa, projected onto the leading pair of empirical orthogonal functions (Wheeler et al., 2009). These data are filtered beforehand so that inter-annual variability, such as the El Niño Southern Oscillation, is removed. The two principle components are defined as RMM1 and RMM2. An example of the RMM index is presented in Figure 2.20.

The bottom panel in Figure 2.20 presents the amplitude (i.e. the two principle components combined in quadrature) for 2008. An MJO event is defined as "strong" if its amplitude exceeds 1. The yellow shading, bound by the vertical dashed lines, indicates the time period examined in the top panel. The strong MJO event observed in March 2008 is observed in two dimensional phase space as an anticlockwise excursion from the origin. The index is categorised into 8 phases, which marks the location of the MJO in time, where, phases $8-1$ indicate the Western Hemisphere and Africa, phases $2-3$ indicate the Indian Ocean, phases $4-5$ indicate the Maritime Continent, and phases $6-7$ indicate the Western Pacific.

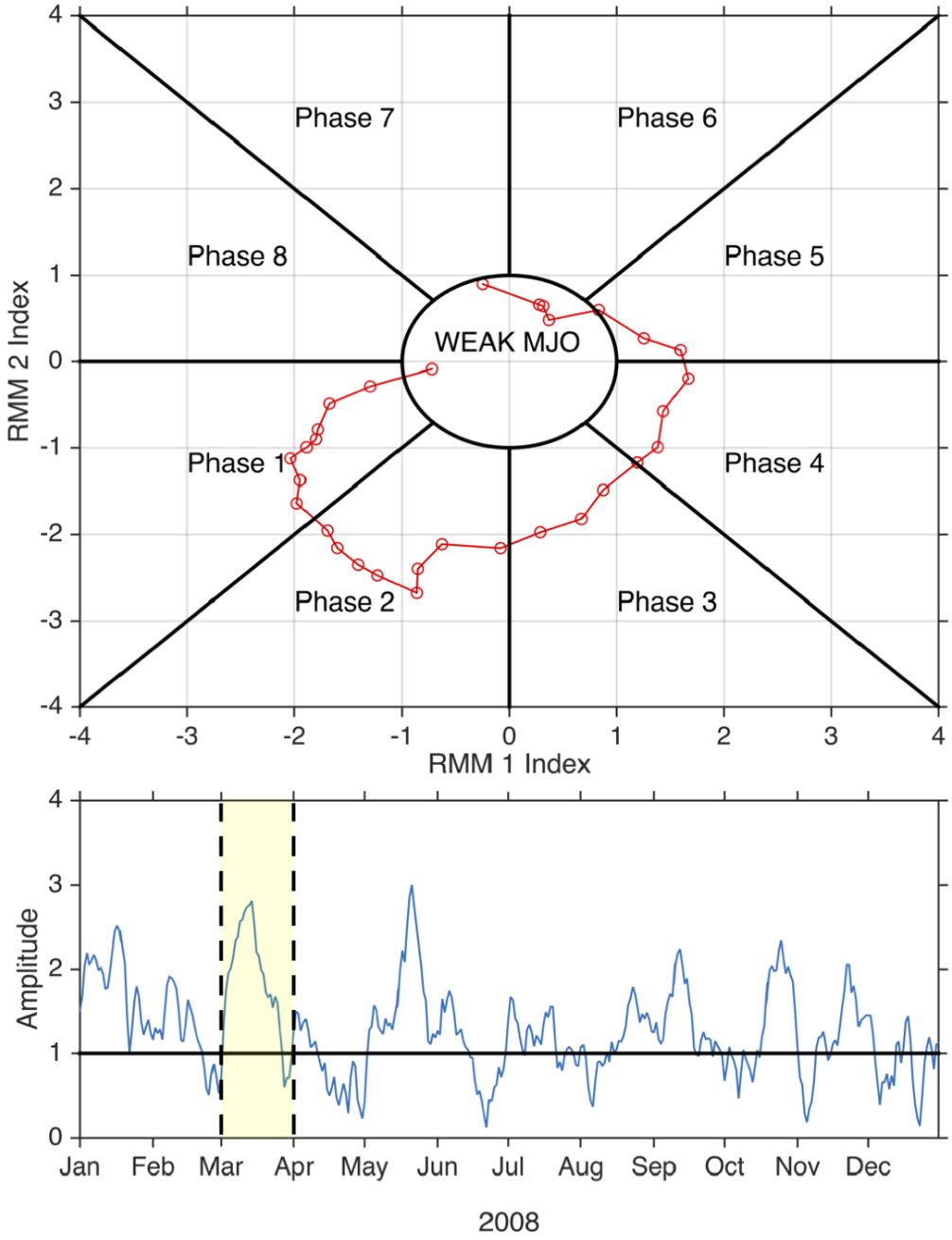

Figure 2.20: *An example of the RMM index of Wheeler and Hendon (2004) for 2008. The bottom panel presents the amplitude of the RMM index for 2008. RMM index values above 1 define a strong MJO event. The top panel shows the relative phase of the MJO for a strong event in March 2008 (highlighted by the yellow shading, bound by the vertical dashed lines, in the bottom panel).*

The RMM index is typically used to monitor the MJO and its associated weather effects. Importantly, the RMM index provides a method of isolating the MJO component of a particular variable based on the amplitude and phase of MJO events.

Composite maps for each MJO phase can provide visual evidence of the characteristic eastward propagation of MJO features. In this work the RMM indices are applied to 20–100 day bandpassed stratospheric gravity-wave potential energies to reveal MJO variability. The results of this are presented in Chapter 3 and are published in Geophysical Research Letters (Moss et al., 2016b).

2.5 Summary

This chapter introduces the two primary methods used to study gravity-wave properties in the following chapters of this thesis. COSMIC radio occultation data are used in Chapter 3 to identify MJO variability in gravity wave potential energies. Ascension Island meteor radar data are used in Chapter 4 to characterise the contribution of gravity-wave momentum fluxes to the anomalous wind events observed in the first phase of the mesospheric semi-annual oscillation in 2002.

In addition, the other supporting data-sets used in this thesis are discussed. In Chapter 3, OLR and ECMWF data are used to identify whether MJO variability in gravity-wave energies is a result of the dynamic or convective signature of the MJO. In addition ECMWF data are used to assess the critical level filtering. In Chapter 4, OLR and TRMM are used as proxies for convective activity and ECMWF data are used to assess the critical level filtering present in the underlying atmosphere.

Chapter 3

Does the Madden-Julian Oscillation Modulate Stratospheric Gravity Waves?

The circulation of the stratosphere is strongly influenced by the fluxes of gravity waves propagating from tropospheric sources. In the tropics, these gravity waves are primarily generated by convection. The Madden-Julian Oscillation (MJO) dominates the intra-seasonal variability of this convection. However, the influence of the MJO on the variability of stratospheric gravity waves is largely unknown. Here we examine gravity-wave potential energy at 26 km and the upper tropospheric zonal-wind anomaly of the MJO at 200 hPa, sorted by the relative phase of the MJO using the RMM MJO indices. We show that a strong anti-correlation exists between gravity-wave potential energy and the MJO eastward wind anomaly. We propose that this correlation is a result of the filtering of upward-propagating waves by the MJO winds. The study provides the first observational evidence that the MJO contributes significantly to the global variability of stratospheric gravity waves in the tropics. The material in this Chapter is published in:

Moss, A. C., Wright, C. J., and Mitchell, N. J. Does the Madden-Julian Oscillation Modulate Stratospheric Gravity Waves?, Geophys. Res. Lett., 43, 39733981, 2016.

3.1 Introduction

Gravity waves play a very important role in the dynamics of the stratosphere. The waves can propagate upwards from their sources in the troposphere upwards to greater heights, resulting in a vertical flux of energy and horizontal momentum. When the waves dissipate, this energy and momentum are transferred to the mean flow.

Gravity waves can be generated by a variety of sources, including winds blowing over mountains and the adjustment of jet streams. In the tropics, deep tropospheric convection associated with cumulus clouds is the main source of gravity waves (e.g. Alexander et al., 2008b; Wright and Gille, 2011). Such tropical waves drive important features of the tropical stratospheric circulation, including the Quasi-Biennial Oscillation (QBO) and Semi-Annual Oscillation (SAO) (e.g. Hamilton et al., 2004). Measurements of the fluxes and variability of gravity waves and how these are related to their sources are thus essential in efforts to understand the dynamics of the stratosphere and in efforts to develop numerical weather prediction and climate models (e.g. Fritts and Alexander, 2003; Alexander et al., 2010).

Tropical cumulus convection itself varies significantly on intra-seasonal timescales (i.e. timescales of $\sim 10 - 100$ days). The largest component of this variability is the Madden-Julian Oscillation (MJO) (Madden and Julian, 1972), which is the most prominent Intra-Seasonal Oscillation (ISO). The MJO is a large-scale repeating pattern of coupled circulation and deep convection that originates in the Indian Ocean and then propagates eastwards to the western/central Pacific. It has a period of $\sim 30 - 90$ days and typically travels at ~ 5 ms^{-1} (e.g. Zhang, 2005). Whilst the convection of the MJO is largely confined to the eastern hemisphere, its dynamical influence is apparent on a global scale (e.g. Salby et al., 1994). The MJO is known to be closely associated with convectively coupled Rossby and Kelvin waves (e.g Matthews, 2000; Sperber, 2003; Khouider et al., 2011). Anomalies in tropospheric zonal wind are observed towards the MJO centre close to the surface (850 hPa) and away from the MJO centre in the upper troposphere (200 hPa), as presented schematically in Figure 3.1. In light of the known role of the MJO in modulating tropical convection, we can thus ask the question: *does the MJO act to modulate the variability of stratospheric gravity waves?*

To date, there have only been a very limited number of attempts to determine the influence of the MJO on the variability of gravity waves in the tropical stratosphere. In particular, Horinouchi (2008) used a cloud-resolving model to investigate convectively-

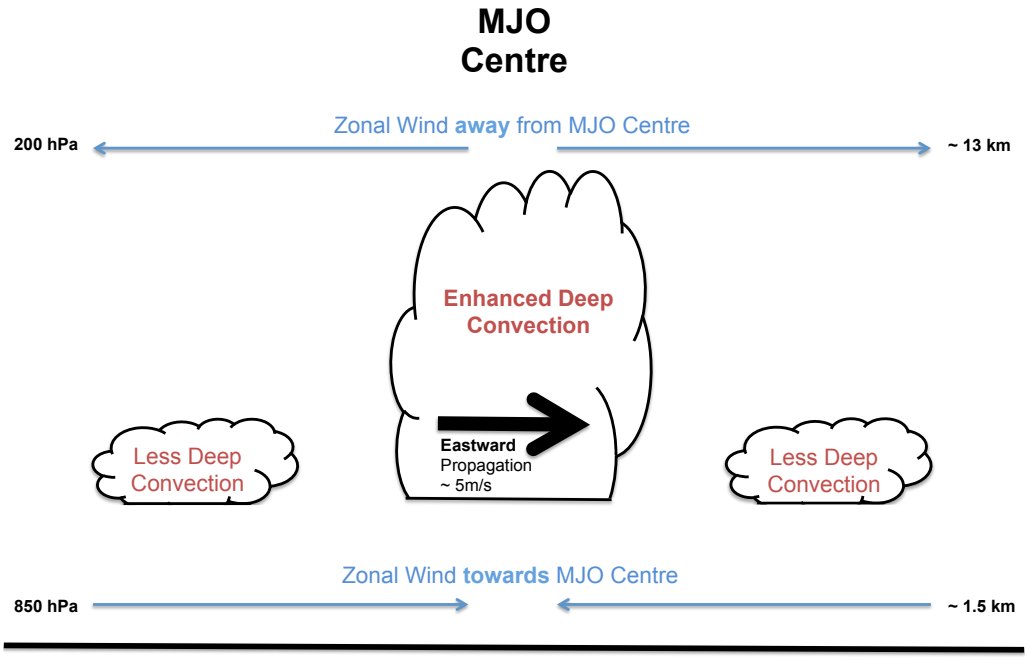

Figure 3.1: *Schematic diagram showing some characteristics of the Madden-Julian Oscillation. Adapted from Zhang (2005)*

generated gravity waves and their propagation into the stratosphere. He found that upward propagation of gravity waves was significantly increased during the inactive phase of the MJO (when there is actually reduced convection). This apparently counter-intuitive result is a consequence of the modelled gravity waves generated in the inactive phase of the MJO having i) higher phase speeds and ii) longer vertical wavelengths than those gravity waves generated in the active phase. This arises from the greater convective cloud rain-top heights associated with the inactive phase of the MJO (e.g. Morita et al., 2006). These gravity waves of higher phase speed and longer vertical wavelength are better able to propagate into the stratosphere where they account for the increased gravity-wave fluxes.

In contrast, Karoly et al. (1996) considered radiosonde data from Santa Cruz (10° S, 165° E) in the south Pacific recorded during the 4-month TOGA-COARE campaign of 1992-3 when the MJO had significant amplitude. They reported significant correlations between gravity-wave activity in the lower stratosphere (17 – 24 km) and proxies for convective activity including Outgoing Long-wave Radiation (OLR), thus suggesting a positive correlation between the MJO convection and gravity-wave activity in the lower stratosphere.

There is some evidence that ISOs in tropospheric convection, including the MJO, modulate the fluxes of gravity-waves and/or non-migrating tides in the tropical mesosphere and lower thermosphere (MLT). Eckermann et al. (1997) reported that gravity-wave variances and MLT winds both display fluctuations at ISO periodicities. They proposed that ISOs, including the MJO, may be modulating the generation of gravity waves and non-migrating tides that then subsequently propagate through the stratosphere to the MLT where their modulated momentum fluxes drive fluctuations in the winds at ISO periods when the gravity waves and/or tides dissipate. This suggestion has received support from other observations of fluctuations in MLT-region winds at ISO and MJO periodicities (e.g. Davis et al., 2012; Rao et al., 2009). However, other studies have argued that non-migrating tides drive the MLT-region ISOs, and so the role of modulated gravity-wave fluxes remains unclear (e.g. Isoda et al., 2004).

We thus see that there is great uncertainty regarding the magnitude and phasing of any connection between the MJO and stratospheric gravity waves. However, establishing the nature of any such modulation is important in attempts to understand the coupling of the tropical troposphere and stratosphere. These uncertainties highlight the need for studies to determine the magnitude and relative phasing of any MJO influence on the field of convectively-generated gravity waves.

Here we present observations of gravity-wave potential energies (GWPE) made in the tropical lower stratosphere from COSMIC radio occultation satellite observations. GWPE at 26 km and zonal-wind anomalies at the 200 hPa pressure level are examined to investigate their intra-seasonal variability. The fundamental novelty of our analysis is to sort our observations of stratospheric gravity waves by the phase of the MJO defined by the Real Multivariate MJO (RMM) indices (Wheeler and Hendon, 2004). This is the first time this analysis has been applied to stratospheric gravity-waves. Finally, we propose and provide evidence for a mechanism by which this stratospheric gravity-wave variability is caused by the MJO.

3.2 Data and Analysis

3.2.1 COSMIC GPS-RO Gravity-Wave Observations

The Constellation Observing System for Meteorology, Ionosphere and Climate (COSMIC) was launched in April 2006 and consists of six low Earth orbiting satellites that

track GPS satellites as they rise or set over the horizon. The radio signal received by these satellites is influenced by the atmospheric limb. Vertical profiles of temperature and pressure can be computed from the phase delay of the signal (Liou et al., 2007). COSMIC data has been extensively used for a number of gravity-wave studies (e.g. Alexander et al., 2008b, 2013; Wang and Alexander, 2010; Wright et al., 2011; McDonald, 2012; Faber et al., 2013; Hindley et al., 2015).

Here we use COSMIC level-2 dry atmospheric temperature data from September 2006, to December 2012. GPS radio-occultation (GPS-RO) measurements have sub-Kelvin temperature precision (Tsuda et al., 2011), horizontal resolution in the stratosphere of ~ 270 km (Kursinski et al., 1997; Hindley et al., 2015) and features with vertical scales greater than 2 km can be distinguished from noise (Marquardt and Healy, 2005; Tsuda et al., 2011). Thus, we interpolate all COSMIC profiles to 2 km resolution prior to analysis and as a result will only observe gravity waves with vertical wavelengths greater than 4 km. In addition, limb sounding instruments, such as COSMIC, are most sensitive to mid- and low-frequency gravity waves (i.e. inertia-gravity waves) that have short vertical and long horizontal wavelengths (e.g. Wright et al., 2015). Hence, our results are only representative of this part of the wave spectrum.

For each day of data, the COSMIC temperature profiles are binned onto a $10^\circ \times 20^\circ$ latitude-longitude grid, stepped in $1^\circ \times 1^\circ$ increments. Zonal mean and planetary-scale features of zonal wavenumber $0-6$, such as Kelvin waves, are calculated at each latitude and height. The resulting local background temperature profile, $\bar{T}$, is removed from each original temperature profile by interpolating to its latitude-longitude position to reveal the temperature perturbations due to gravity waves alone. We next apply an S-Transform (Stockwell et al., 1996) to each temperature perturbation profile, T', to determine the largest resulting wave amplitude at each height. This amplitude is used to calculate the potential energy, E_p, (Tsuda et al., 2000) for each height using equation 3.1, where the acceleration due to gravity, g, is assumed to be constant and N is the Brunt-Väisälä frequency.

$$E_p = \frac{1}{2}\left(\frac{g}{N}\right)^2 \left(\frac{T'}{\bar{T}}\right)^2 \tag{3.1}$$

The GWPE for each day is then defined as the average E_p for each $10^\circ \times 20^\circ$ latitude-longitude cell at a height of 26 km. The time-series of GWPE in each cell is then bandpassed with a 201-point Lanczos filter (Duchon, 1979) with half-power points at 20 and 100 day periods to reveal any intra-seasonal variability in the data. This

bandpassing method closely follows the methodology of the CLIVAR (2009), who presented a standardised method of identifying MJO signals in atmospheric data.

3.2.2 ECMWF Zonal Wind

European Centre for Medium Range Weather Forecasting (ECMWF) operational analysis data are used to calculate zonal-wind anomalies at the 200 hPa pressure level. The data used are from the 1.125° resolution data-set and are bandpassed for each grid point in the same way as GWPE to filter for intra-seasonal variability.

3.2.3 Outgoing Long-Wave Radiation

In this work the NOAA outgoing long-wave radiation (OLR) data-set is used as a proxy for convective activity. These data provide daily values of OLR on a $2.5° \times 2.5°$ latitude-longitude grid that has been pre-processed to fill any gaps using temporal and spatial interpolation (Liebmann and Smith, 1996). OLR values result from the cloud-top temperatures and, as such, a low value corresponds to increased convective activity. The OLR data-set is bandpassed for each grid point in the same way as GWPE to filter for intra-seasonal variability.

3.2.4 RMM MJO Index

The Real-time Multivariate MJO (RMM) index of Wheeler and Hendon (2004) defines the daily variation in amplitude and phase of the MJO for eight specific phases. The index is composed of a combination of equatorially-averaged anomalies of OLR and zonal-wind at 850 hPa and 200 hPa projected onto the leading pair of empirical orthogonal functions (Wheeler et al., 2009).

Here we use the MJO index to create composite maps for our data for each MJO phase. Data are only used in the composite average for each phase if they fall within that phase and the amplitude of the RMM index exceeds 1 (i.e. a strong MJO is present). This analysis results in maps of 20–100 day bandpassed GWPE and 200 hPa zonal-wind anomalies for each MJO phase. It thus provides an appropriate tool to investigate the connection between stratospheric gravity waves and the MJO. This 20-100 day period range is specifically chosen because it is that used to evaluate MJO

simulations in the consistent framework of CLIVAR (2009). We will refer to the 20-100 day period range as the "MJO period range" from here onwards.

3.3 Results

The geographical and seasonal variability of GWPE is presented in Figure 3.2. The left-hand column shows (from top to bottom) mean GWPE, the variance of 2-180 day bandpassed GWPE and the variance of MJO period range GWPE as composites averaged over boreal summer months (May to October). Mean GWPE is enhanced over Africa, the Bay of Bengal, and Central America. The variances of the 2-180 day and MJO period range GWPE are more widely distributed around the tropics.

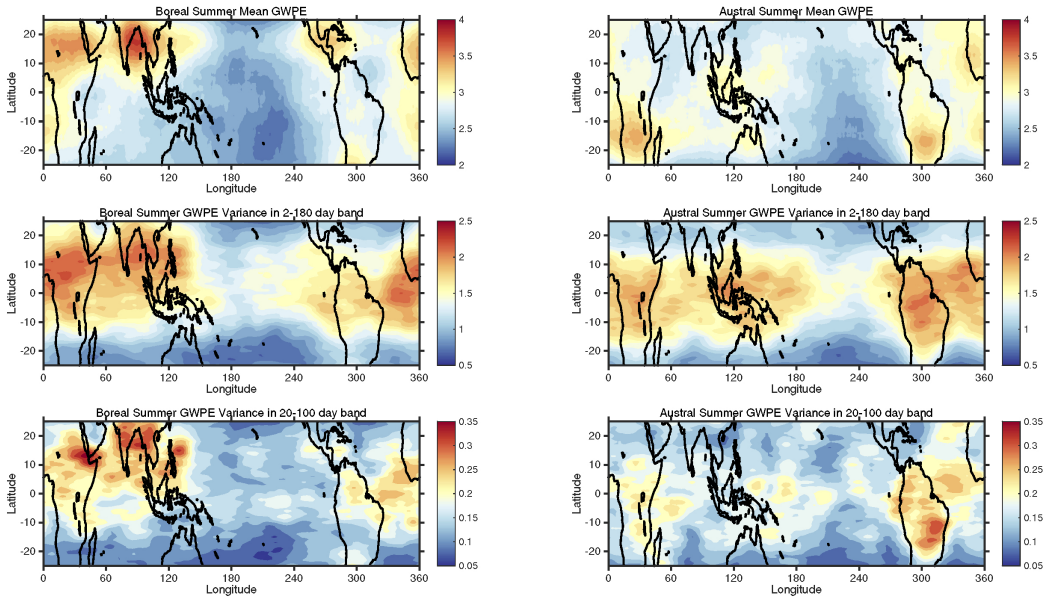

Figure 3.2: *Composite mean plots of GWPE for (left) boreal Summer (May to October) and (right) austral Summer (November to April). Top subplots show the mean GWPE for each season, middle subplots show the variance of GWPE in the intra-annual bandpass (2–180 day) for each season and the bottom subplots show the variance of GWPE in the intra-seasonal bandpass (20–100 day) for each season. The units for the top subplots of mean GWPE are in* Jkg^{-1}*. For all other subplots showing the variance of GWPE, units are in* J^2kg^{-2}*.*

The right-hand column shows the same analysis, but averaged over the austral summer months (November to April). There are enhanced regions of mean GWPE over southern Africa, Indonesia, and South America and the variance of bandpassed

GWPE is more uniformly distributed. Lower energies are observed in austral summer compared to boreal summer and the largest values tend to be in the summer hemisphere, as is especially evident in the panels showing mean GWPE. Comparison of the intra-annual and intra-seasonal gravity-wave variances shows that there is a significant proportion of variability associated with ISOs.

The RMM indices of Wheeler and Hendon (2004) provide a method of identifying whether the ISOs in observational data exhibit a correlation with the MJO. Figure 3.3 presents mean composites of MJO period range GWPE (filled contours) and MJO period range zonal-wind anomalies at 200 hPa (coloured lines) for each phase of the RMM indices where a strong MJO is present (where the amplitude of the RMM index is greater than 1). Purple solid lines indicate regions of increased eastward zonal-wind and green dot-dashed lines indicate regions of increased westward zonal-wind. The number of days noted on the right axis of each phase composite represents the number of days used to calculate that particular composite mean.

A clear eastward movement of both GWPE and zonal-wind anomalies around the entire tropical belt is observed as the phase of the MJO progresses. The amplitude of the GWPE anomalies are ~ 0.15 J kg^{-1}. This amounts to approximately $5 - 10\%$ of the total GWPE evident in Figure 3.2. This is in contrast to the convective signature of the MJO, as shown in Figure 3.4, which is mostly confined to the eastern hemisphere. The analysis used to produce Figure 3.4 is identical to that for Figure 3.3, using OLR measurements as the proxy for the convective activity associated with the MJO.

There appears to be a very close correlation between GWPE and these zonal-wind anomalies. Specifically, stronger eastward winds appear to occur at the same time as a depression in GWPE and stronger westward winds when GWPE is increased. This suggests that the dynamic response (i.e. the zonal-wind anomalies at 200 hPa - See Figure 3.1) of the MJO has a stronger influence on the stratospheric GWPE than the source-variability evidenced by OLR.

To quantify the relationship between the MJO characteristics and GWPE, we correlate the MJO period range GWPE and the MJO period range 200 hPa zonal-winds. In order to provide an estimate of the significance, bootstrapping (e.g. Efron, 1979; Wright et al., 2012) was used by randomly resampling from the days within each MJO phase 1000 times. For each sample and MJO phase, the composite map for both MJO period GWPE and 200 hPa zonal wind were averaged between 20° S and 20° N and correlated to obtain a distribution of correlation coefficients and associated

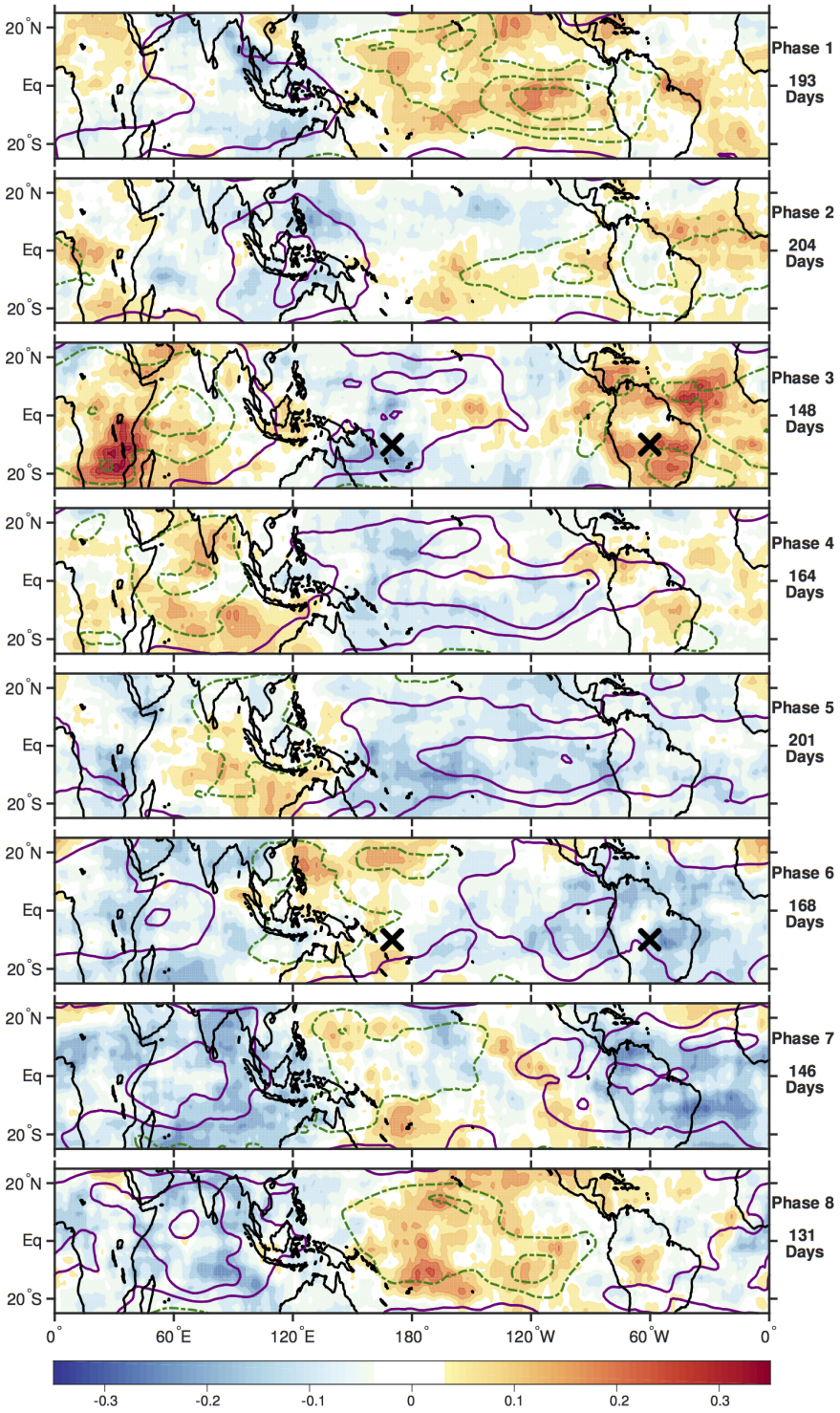

Figure 3.3: *Composite plots of 20–100 day bandpassed zonal-wind anomalies and 20–100 day bandpassed GWPE averaged over all days for each phase of the RMM MJO Index where the amplitude exceeded 1 (number of days indicated on the right axis of each panel). zonal-wind data are shown as purple solid (+ve) and green dash-dot (-ve) contours in intervals of* ± 2 *ms*$^{-1}$ *from 1 ms*$^{-1}$*. The black crosses on the panels for Phase 3 and 6 indicate two locations where wave filtering was compared (see Figure 3.7). Units of GWPE are in J kg*$^{-1}$*.*

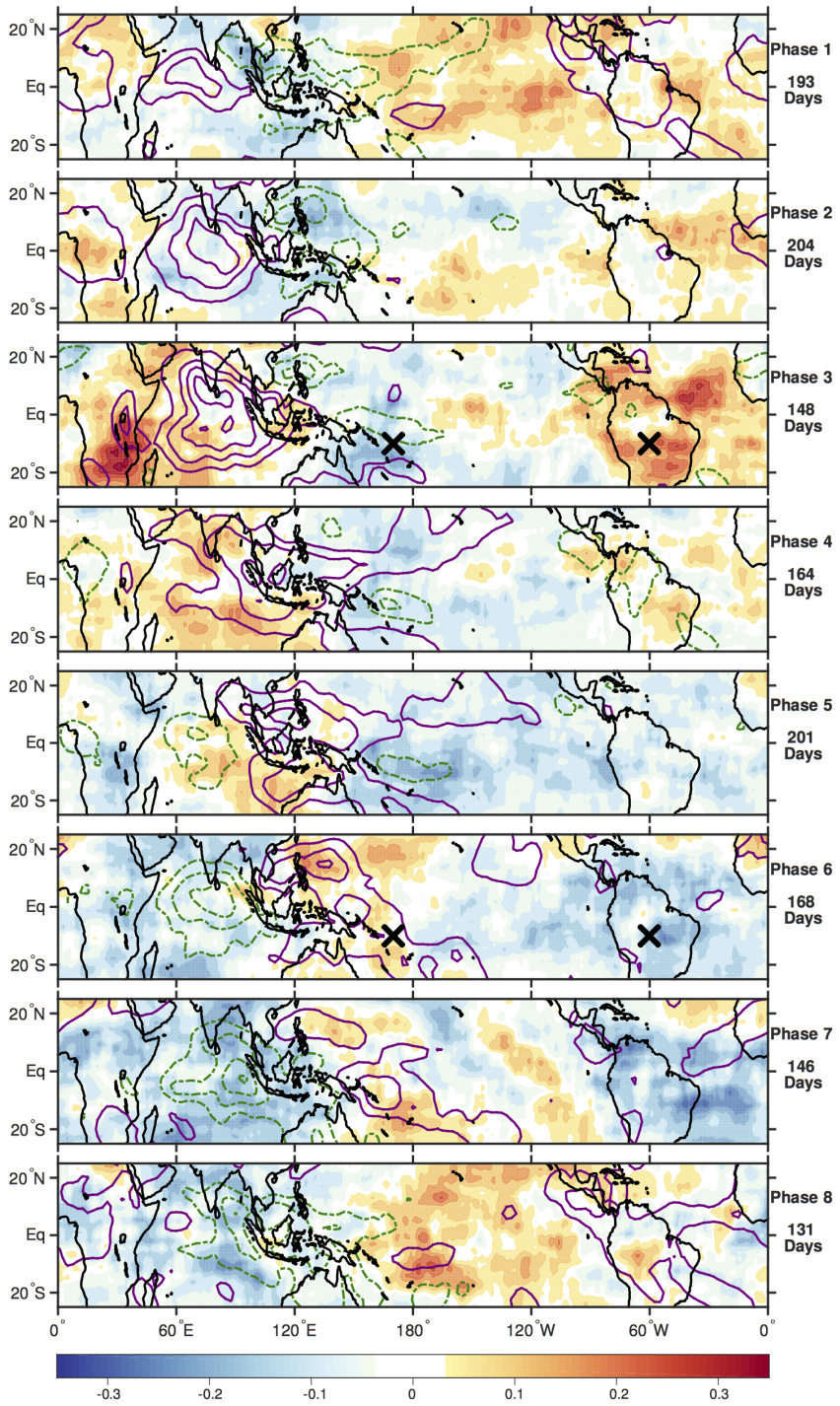

Figure 3.4: *Composite plots of 20–100 day bandpassed OLR and 20–100 day bandpassed GWPE averaged over all days for each phase of the RMM MJO Index where the amplitude exceeded 1 (number of days indicated on the right axis of each panel). OLR data are shown as purple (-ve) and green (+ve) contours in intervals of* ± 5 *Wm^{-2} from 3 Wm^{-2} (N.B. negative values of OLR are indicative of strong convection). GWPE units are J kg^{-1}.*

longitudinal lags.

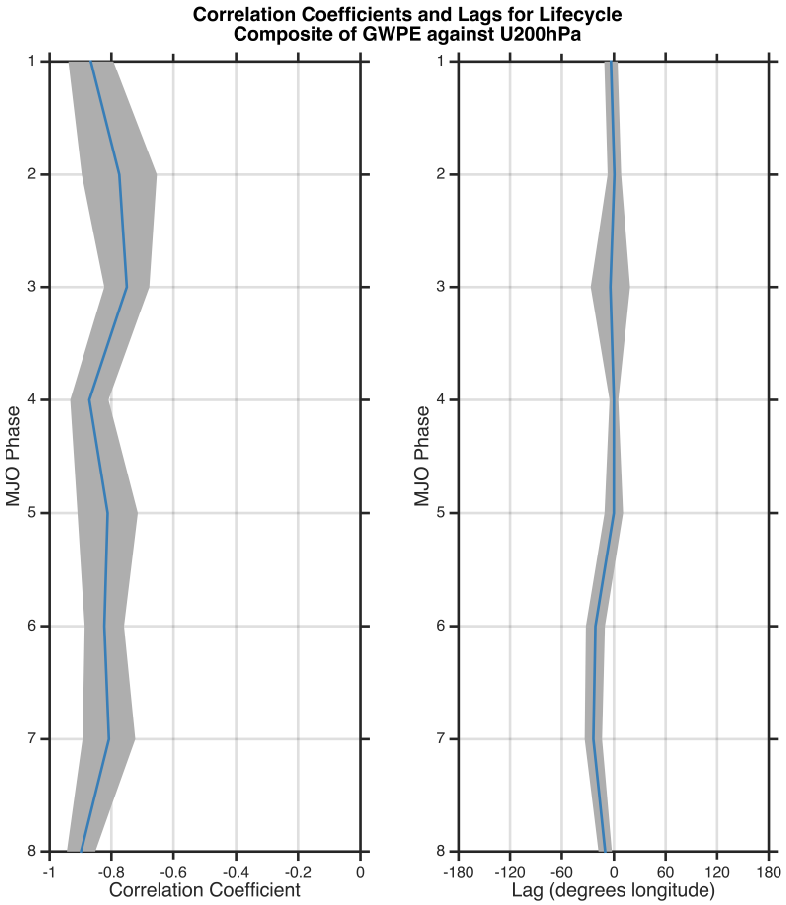

Figure 3.5: *The left panel shows maximum absolute correlation coefficients for the MJO lifecycle composites of ECMWF 200 hPa zonal-wind and GWPE averaged between 20° S and 20° N. The right panel presents the lags these correlation coefficients occur at, for each phase of the MJO. In both panels the grey shading shows the 95% confidence on the mean (blue line) of the bootstrapped distribution of values. The values presented here were calculated by bootstrapping over 10000 samples.*

A strong anti-correlation of ~ -0.8 is observed between GWPE and the 200 hPa eastward wind anomalies at $\sim -20 - 0°$ longitudinal lag (See Figure 3.5). This demonstrates that the modulation of stratospheric GWPE at 26 km is strongly correlated with the dynamic variability of the MJO as measured by the 200 hPa zonal wind anomalies.

In both panels of Figure 3.5 the grey shading shows the 95% confidence on the mean (blue line) of the bootstrapped distribution of values, for the maximum absolute correlation coefficient (left panel), and the longitudinal lag at which this occurs (right panel). A similar procedure was followed for Figure 3.6 using OLR.

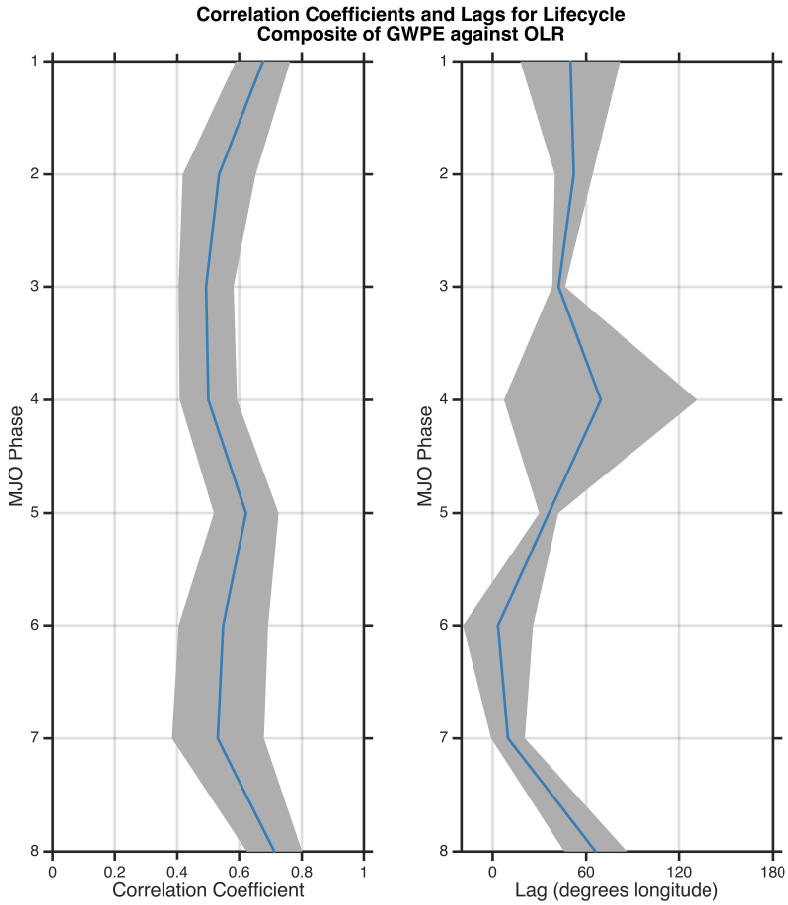

Figure 3.6: *The left panel shows maximum absolute correlation coefficients for the MJO lifecycle composites of OLR and GWPE averaged between 20° S and 20° N. The right panel presents the lags these correlation coefficients occur at, for each phase of the MJO. In both panels the grey shading shows the 95% confidence on the mean (blue line) of the bootstrapped distribution of values. The values presented here were calculated by bootstrapping over 10000 samples.*

We propose that this correlation is a result of the filtering of upward propagating gravity waves by the MJO wind anomalies, which impose an MJO modulation on the GWPE. To investigate this mechanism, we will now consider the range of absolute winds (i.e. background plus anomaly) encountered by such waves at different points in the MJO phase and consider the filtering effects on the waves of these winds.

Firstly, we will illustrate the concept of the proposed mechanism by considering the winds encountered by upward propagating gravity waves at two different locations during MJO phase 3 and phase 6. The locations are (170° E, 10° S) and (60° W, 10° S). They are arbitrarily chosen to represent regions of increased and reduced GWPE. Each location is indicated by black crosses in Figure 3.3. The composite

mean unfiltered ECMWF zonal-wind speed from $5 - 30$ km at these two locations in MJO phases 3 and 6 are presented in Figure 3.7. In each plot the range of winds encountered between 10 km and 26 km is bound by the dotted vertical lines and filled by the blue shading. The thick horizontal black bars indicate the total range of winds encountered between 10 and 26 km in each case.

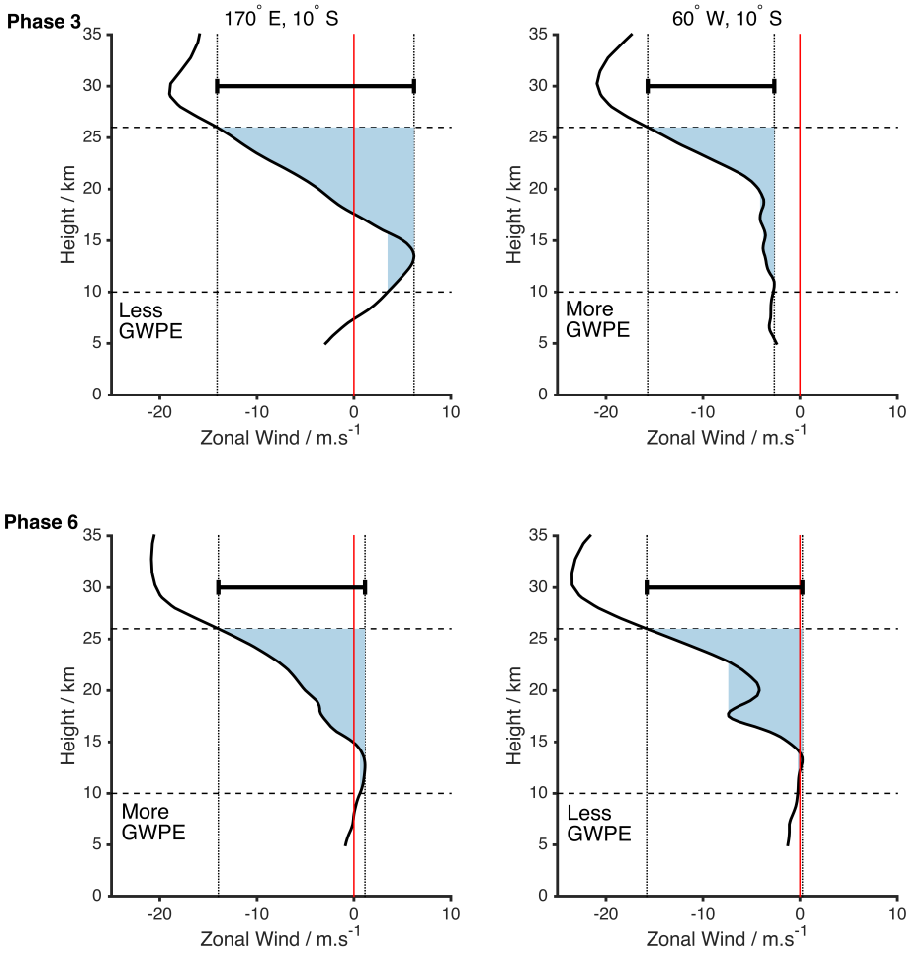

Figure 3.7: *Non-bandpassed ECMWF zonal-wind profiles for the two locations indicated by crosses in Figure 3.7 for MJO phase 3 and phase 6. The dark blue shaded region on each plot shows the range of winds encountered as waves ascend between 10 km and 26 km. The total range of winds encountered between these heights is illustrated by the black bar at the top of each panel.*

The left-hand panels in the Figure show the range of winds for (170° E, 10° S), where reduced GWPE and stronger eastward wind anomalies occur in phase 3 and vice versa in phase 6. Examination of the Figure shows that a wider range of winds is encountered by upward-propagating waves in phase 3 (-14.1 ms^{-1} to 6.19 ms^{-1}) compared to phase 6 (-14.0 ms^{-1} to 1.14 ms^{-1}). This wider range results from the

winds in phase 3 being more eastward in the upper troposphere and peaking around 13 km, which is approximately 200 hPa. In contrast, a smaller range of eastward winds are encountered in phase 6, when GWPE is greater.

The right-hand panels show the range of winds for (60° W, 10° S). Here, greater GWPE and stronger westward wind anomalies occur in phase 3 and vice versa in phase 6. A wider range of winds is observed in phase 6 (-15.8 ms^{-1} to 0.25 ms^{-1}) compared to phase 3 (-15.7 ms^{-1} to -2.63 ms^{-1}). This increase in range is due to a shift eastwards in the upper tropospheric winds in phase 6, where reduced GWPE is observed.

The spectrum of gravity-wave phase speeds is known to be centred at low values (e.g. Fritts and Alexander, 2003). The winds in Figure 3.7 will thus progressively filter out such gravity waves as they propagate to heights where their zonal phase speeds equal the local zonal wind and where they are then absorbed at a critical level. As the local wind includes the MJO anomaly, this process can thus imprint a signature of the MJO anomaly on the field of upward-propagating waves. The variation of winds and GWPE at the points considered in Figure 3.7 is thus consistent with this proposed filtering. However, the data presented in the analysis of Figure 3.7 are only for the two arbitrarily selected locations. We will therefore now generalise this analysis to consider the winds encountered by gravity waves at all longitudes. Further, it is known that the stratospheric GWPE is modulated by the phase of the QBO (e.g. Alexander et al., 2008b), so we will also sort the data by QBO phase.

In this second analysis, we examine the range of zonal winds encountered between 10 and 26 km by upward propagating waves at all longitudes for each QBO phase. We use bootstrapping (e.g. Efron, 1979; Wright et al., 2012) to calculate, as a function of longitude, the distribution of zonal wind ranges and their various percentiles, for increments of 2 degrees longitude. This bootstrapping provides a measure of the uncertainty of the winds. The bootstrapping is done by randomly sampling days from the time-series 1000 times for days sorted by both QBO phase and MJO phase.

To illustrate the results of this analysis, we will consider the case where the QBO is westward and the MJO is in phase 3 and phase 6. We present in Figure 3.8 the magnitude of the range of winds encountered between 10 km and 26 km range for MJO phase 3 (solid blue line) and MJO phase 6 (solid orange line). Also indicated by shading is the 95% confidence interval from the bootstrapping. Finally, the two vertical dashed lines indicate the longitudes of the two arbitrary locations considered above.

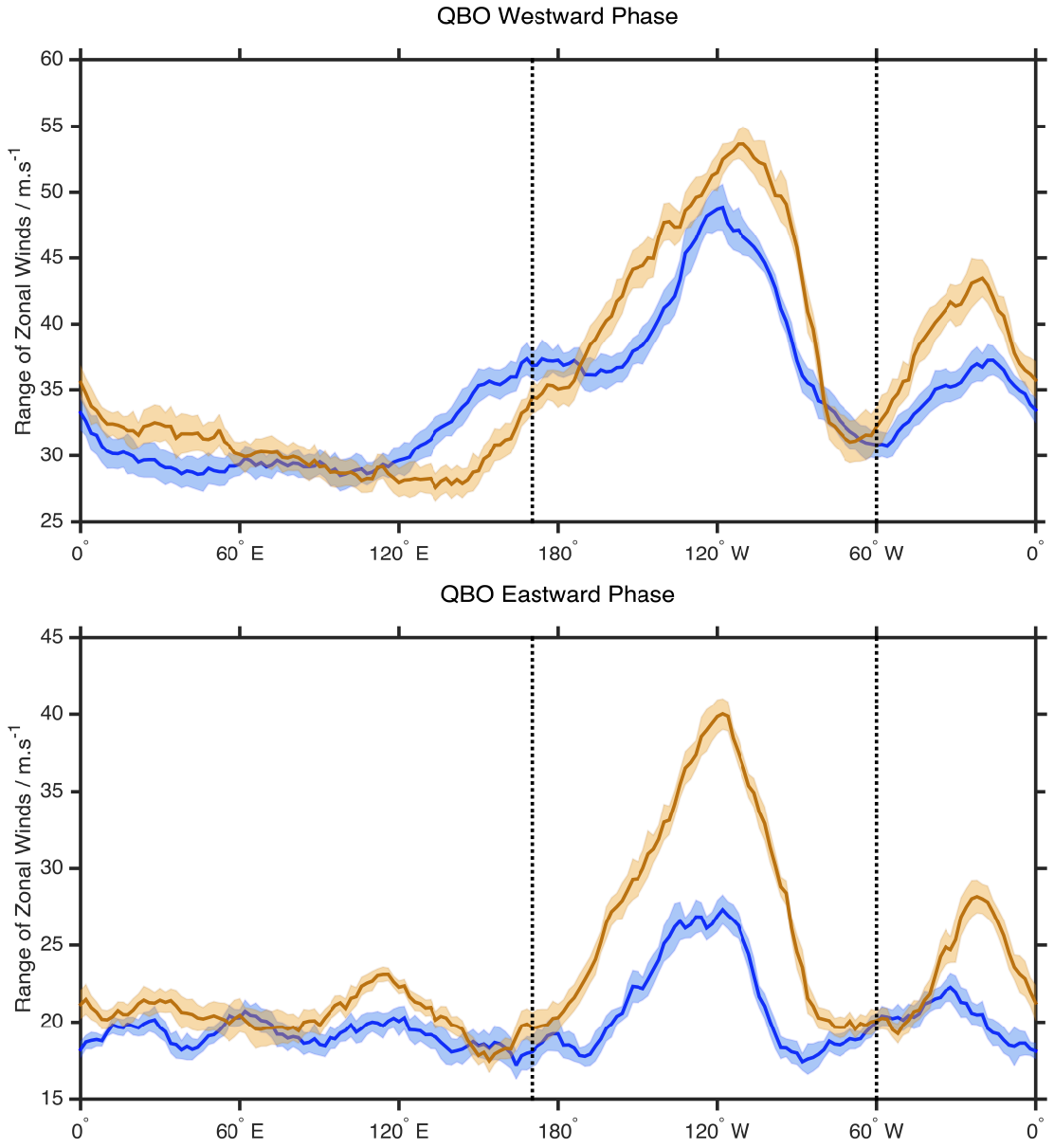

Figure 3.8: *Bootstrapped distribution (1000 samples) of non-bandpassed ECMWF zonal-wind absolute range between 10 and 26 km (i.e. the height range considered in Figure 3.7) against longitude for the QBO westward phase (top) and QBO eastward phase (bottom) at 10° S. The shading shows the 95% confidence interval on the mean (thick line) of the bootstrapped distribution for MJO phase 3 (blue) and phase 6 (orange). In both panels the vertical black dotted lines highlight the locations indicated by crosses in Figure 3.3.*

For the QBO westward phase (top panel Figure 3.8) it can be seen that the zonal wind range was generally *larger* in phase 3 than phase 6 at longitudes between approximately 120° E to 170° W (i.e. where the GWPE was *smaller* during phase 3 than phase 6 - see Figure 3.3). Conversely, the zonal wind range was *smaller* in phase

3 than phase 6 at most other longitudes (i.e. where the GWPE was *larger* during phase 3 than phase 6 - see Figure 3.3). An examination of the absolute values of the winds reveals that the variability occurs largely in the eastward component of the winds. Similar results are found comparing the winds and GWPE for the other MJO phases. Similar results are also observed for the QBO eastward phase (bottom) but are less clearly defined.

The confidence intervals shown on the figure indicate that this result is statistically significant to at least a 95% confidence level. The MJO period modulation of GWPE, as presented in Figure 3.3, is observed more clearly during the westward phase of the QBO compared to the eastward phase. This is presented in Figures 3.9 and 3.10, respectively, which shows the MJO period GWPE and 200 hPa zonal winds further filtered by QBO phase. Thus, our results provide clearer evidence of MJO modulation of GWPE by the MJO zonal wind anomalies during the QBO westward phase and a reduced effect during the QBO eastward phase. This is most likely a consequence of the larger amplitude zonal winds in the westward phase (e.g. Baldwin et al., 2001). Collectively, our results show that at a given latitude, the larger range of wind speeds encountered between 10 km and 26 km as a result of the MJO is associated with reduced GWPE at 26 km and vice versa.

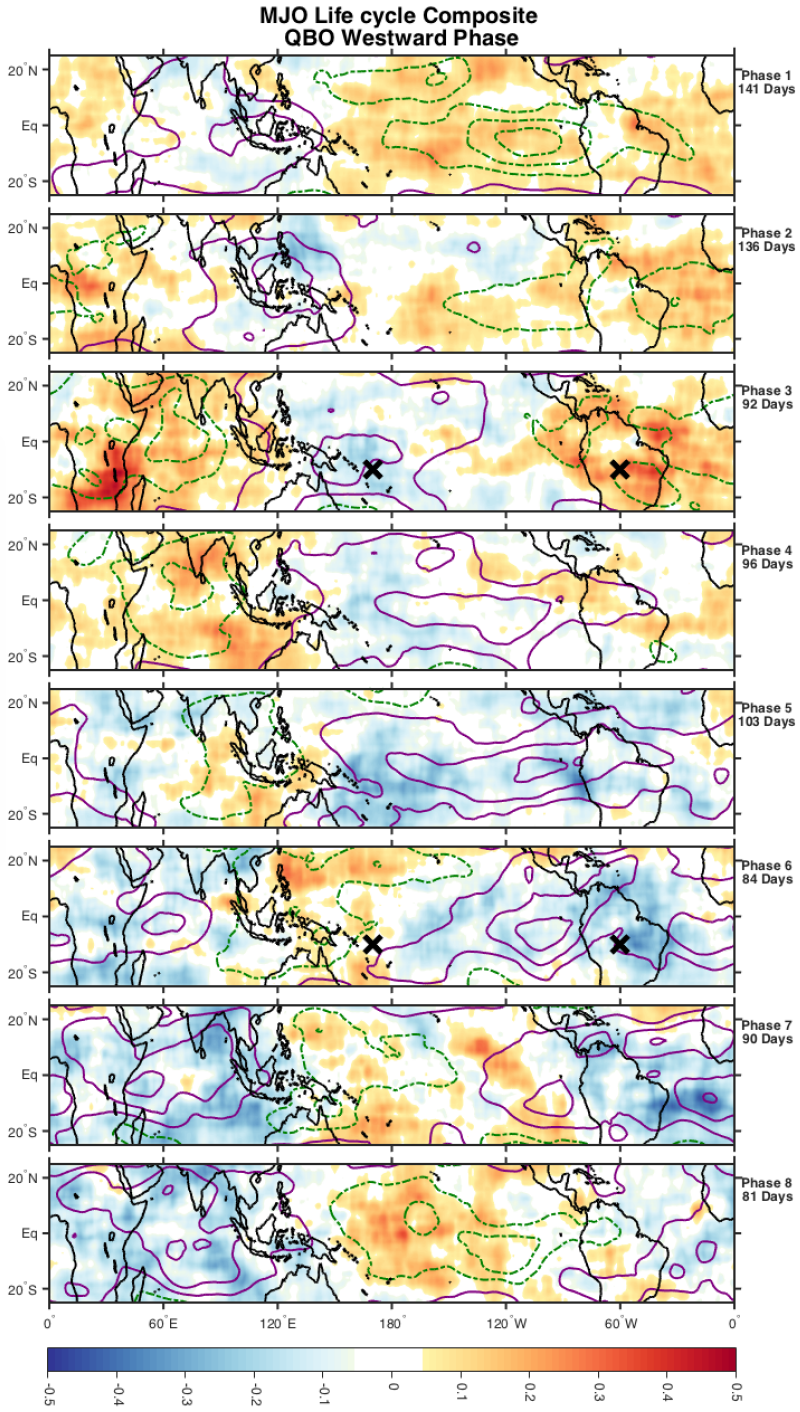

Figure 3.9: *Composite plots of 20–100 day bandpassed zonal-wind anomalies and 20-100 day bandpassed GWPE averaged over all QBO westward phase days for each phase of the RMM MJO Index where the amplitude exceeded 1 (number of days indicated on the right axis of each panel). zonal-wind data are shown as purple solid (+ve) and green dash-dot (-ve) contours in intervals of* ± 2 ms^{-1} *from 1* ms^{-1}*. The black crosses on the panels for Phase 3 and 6 indicate two locations where wave filtering was compared (see Figure 3.7). Units of GWPE are in* Jkg^{-1}*.*

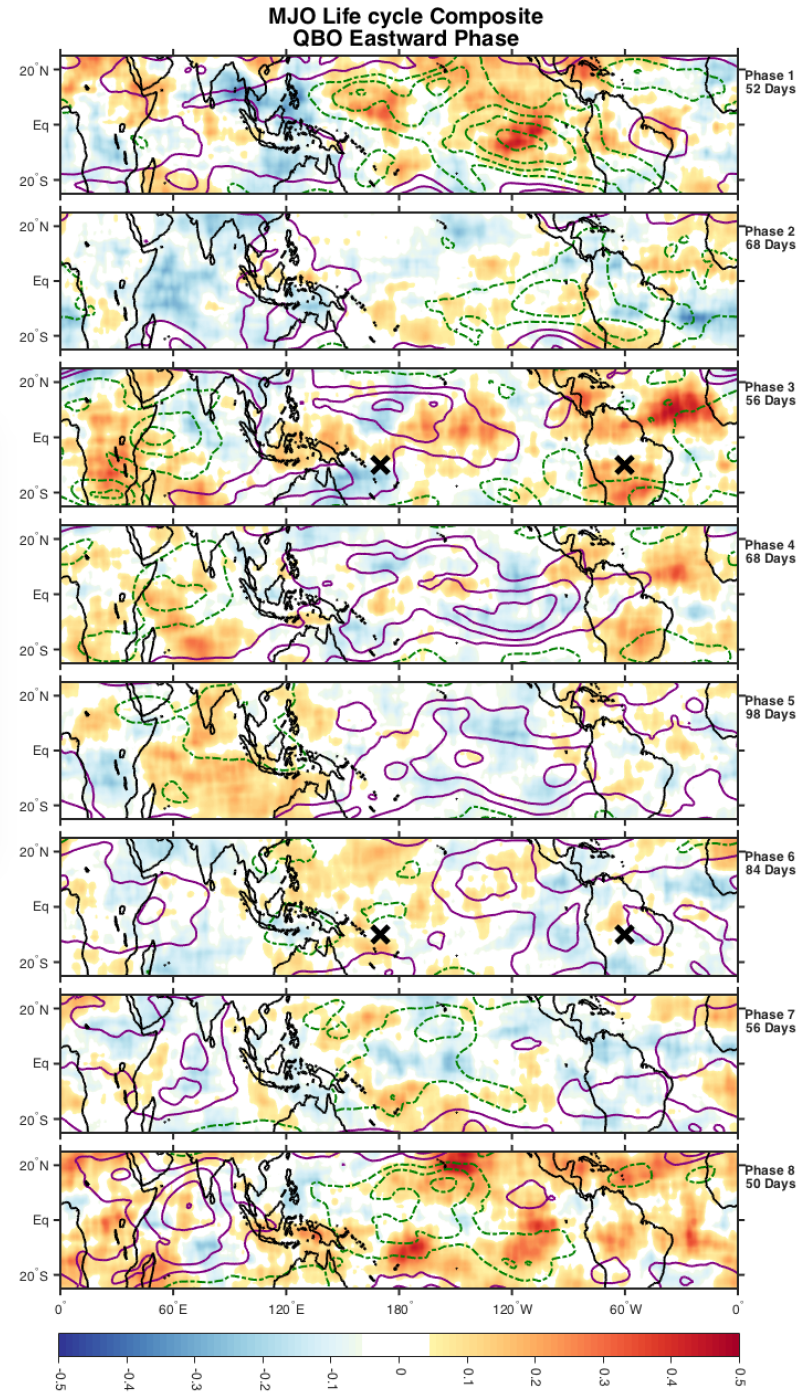

Figure 3.10: *Composite plots of 20-100 day bandpassed zonal-wind anomalies and 20-100 day bandpassed GWPE averaged over all QBO eastward phase days for each phase of the RMM MJO Index where the amplitude exceeded 1 (number of days indicated on the right axis of each panel). zonal-wind data are shown as purple solid (+ve) and green dash-dot (-ve) contours in intervals of* ± 2 *ms*$^{-1}$ *from 1 ms*$^{-1}$*. The black crosses on the panels for Phase 3 and 6 indicate two locations where wave filtering was compared (see Figure 3.7). Units of GWPE are in Jkg*$^{-1}$*.*

3.4 Discussion

There are two principal methods whereby the MJO might modulate the field of stratospheric gravity waves. Firstly, the modulation of convection by the MJO might modulate the excitation of gravity waves. Secondly, the MJO wind anomalies in the troposphere might modulate the wave propagation environment through critical-level filtering. Both of these mechanisms might thus modulate the field of gravity waves that reach the stratosphere.

There exist very few studies investigating the influence of the MJO on stratospheric gravity waves. However, Horinouchi (2008) suggested that the reduced convection during the inactive phase of the MJO would nevertheless generate larger fluxes of stratospheric gravity-wave energy and momentum than the active phase because of the longer vertical wavelengths generated being better able to propagate vertically. Our results indicate a strong correlation between GWPE and the anomalous zonal winds of the MJO, suggesting that wave critical-level filtering plays an important role. However, these results are not necessarily contradictory because the waves considered by Horinouchi (2008) are of significantly shorter horizontal wavelength and higher frequency than those accessible by COSMIC RO measurements.

Here we have proposed that the MJO wind anomalies cause the GWPE anomalies of Figure 3.3. However, we should note that this mechanism will be sensitive to the horizontal phase speed distribution of the gravity waves. In particular, the mechanism assumes a significant fraction of the waves have eastward phase speeds such that the waves will be filtered out by the eastward wind anomalies of the MJO. Our COSMIC RO measurements provide no information on wave horizontal phase speeds and our assumption cannot therefore be tested with this data-set. Nevertheless, our results suggest that the MJO plays a significant role in modulating the stratospheric gravity wave field.

3.5 Conclusion

The MJO is the dominant driver of intra-seasonal variability in the tropical troposphere. Our observations show a strong correlation between stratospheric GWPE and the anomalous tropospheric zonal winds of the MJO when the observations are sorted by MJO phase. We have proposed that this correlation is a result of a filtering of

the gravity-wave field by these winds which removes primarily eastward propagating waves during the MJO eastward wind anomalies. These results highlight the importance of tropospheric processes in controlling the stratospheric gravity-wave field.

Chapter 4

Anomalous Mesospheric Semi-Annual Oscillation in 2002 and Gravity Waves in the Equatorial Mesosphere

Anomalously strong westward winds during the first phase of the equatorial mesospheric semi-annual oscillation (MSAO) have been attributed to unusual filtering conditions producing exceptional gravity-wave fluxes. We test this hypothesis using meteor-radar measurements made over Ascension Island (8° S, 14° W). An anomalous wind event in 2002 of -85.5 ms^{-1} occurred simultaneously with the momentum fluxes of high-frequency gravity waves reaching the largest observed westward values of -29 m^{2}s^{-2} and strong westward wind accelerations of -510 ms^{-1}day^{-1}. However, despite this strong wave forcing during the event, no unusual filtering conditions or significant increases in wave-excitation proxies were observed. Further, although strong westward wave-induced accelerations were also observed during the 2006 MSAO first phase, there was no corresponding simultaneous response in westward wind. We thus suggest that strong westward fluxes/accelerations of high-frequency gravity waves are not always sufficient to produce anomalous first-phase westward MSAO winds and other forcing may be significant. The material in this Chapter is published in:

Moss, A. C., Wright, C. J., Davis, R. N., and Mitchell, N. J. Gravity-wave momentum fluxes in the mesosphere over Ascension Island (8° S, 14° W) and the anomalous zonal winds of the semi-annual oscillation in 2002, Ann. Geophys., 34, 323-330, 2016.

4.1 Introduction

The general circulation and structure of the mesosphere is strongly influenced by gravity waves launched from sources at lower heights. The waves dissipate in the mesosphere and the divergence in the vertical flux of horizontal momentum carried by the waves results in a body force that accelerates the mean flow. In particular, this acts to close the mid-latitude zonal jets, force a pole-to-pole meridional circulation and reverse the solstitial meridional temperature gradients, such that the summer polar mesosphere is the coldest place on Earth, and drives a number of planetary-scale oscillations such as the stratospheric quasi-biennial oscillation (QBO) (e.g. Fritts and Alexander, 2003).

In the equatorial mesosphere, the principal mode of seasonal wind variability is the mesospheric semi-annual oscillation (MSAO). In most years, the MSAO displays the strongest westward winds at heights of near 80 km shortly before the equinoxes and the strongest eastward winds around 85 km near the solstices. This oscillation is out of phase with the stratospheric semi-annual oscillation (SSAO) (e.g. Burrage et al., 1996; Garcia et al., 1997; Huang et al., 2008; Ratnam et al., 2008b; Kumar et al., 2011; Day and Mitchell, 2013).

However, despite the large amplitude of the MSAO, the details of its forcing remain unclear, although it is thought that the oscillation is entirely driven by waves. In particular, the majority of MSAO forcing appears to come from the dissipation of ascending gravity waves that have been selectively filtered by the eastward and westward winds of the SSAO. In this process, westward SSAO winds allow eastward-propagating waves to reach the mesosphere where their dissipation then forces eastward winds. Similarly, when the SSAO winds are eastward, westward-propagating waves reach the mesosphere where their dissipation results in a westward forcing of mesospheric winds, thus driving the MSAO as an oscillation that is out of phase with the SSAO (e.g. Dunkerton, 1982; Hitchman and Leovy, 1988).

The balance of forcing between high-frequency and inertia gravity waves is uncertain, although Antonita et al. (2008) used meteor radar observations of the mesosphere to conclude that high-frequency gravity waves contribute 20–70% of the overall forcing of the MSAO over Southern India. Other studies have suggested that near the solstices the MSAO receives significant additional forcing from the mean meridional advection of zonal winds and EP flux divergence associated with planetary waves, in particular, the two-day wave (Richter and Garcia, 2006). Near the equinoxes, limited additional

forcing may also come from the dissipation of the migrating diurnal tide (Lieberman and Hays, 1994).

A striking feature of the MSAO is that in some years the winds of the first westward phase of the oscillation reach much larger amplitudes than normal, with westward winds as strong as -80 ms^{-1}. These events are clearly different from the usual behaviour of the MSAO (e.g. Garcia et al., 1997; Day and Mitchell, 2013).

It has been suggested that these anomalous events occur when the relative phasing of the QBO and SSAO produces a selective filtering that allows an excess of westward-propagating gravity waves to reach the mesosphere, thus driving stronger westward winds than normal and thus modulating the MSAO. However, only the westward phase of the MSAO is modulated, due to the westward QBO winds being stronger than the eastward QBO winds and also because the Kelvin waves that drive the eastward phase of the MSAO have larger phase velocities and so are in any case less subject to filtering (e.g. Garcia et al., 1997; Garcia and Sassi, 1999).

It is thus clear that gravity waves play an important and probably dominant role in the forcing of the MSAO, and increased westward fluxes may explain the anomalous westward first phase events. There is thus an essential need to measure gravity-wave momentum fluxes in attempts to understand the MSAO. Despite this, it is notoriously difficult to measure gravity-wave variances, momentum fluxes and accelerations in the mesosphere over the extended intervals necessary. Recently, however, techniques have been developed that allow meteor radars to make statistical measurements of gravity waves at mesospheric heights of $\sim$ 80–100 km (e.g. Hocking, 2005; Fritts et al., 2012). Crucially, these techniques allow estimates of gravity-wave momentum fluxes and their divergence, which then allows estimates to be made of the acceleration of the mean flow by the waves. Note that this method primarily represents the fluxes of high-frequency gravity waves of period less than $\sim$ 2 hours (Placke et al., 2015).

Here, for the first time, we apply these techniques to data recorded by a meteor radar on Ascension Island (8° S, 14° W). We use these data to investigate the relationship between the fluxes of gravity waves, their forcing of the mean flow and the winds of the MSAO. In particular, we will concentrate on the role of gravity waves in forcing an anomalous first-phase westward flow event observed in February/March of 2002. Section 4.2 describes the radar, dataset and analysis used. Section 4.3 presents our observations and Section 4.4 interprets these in terms of wave forcing of the MSAO during this particular event.

4.2 Data and Data Analysis

Measurements of mesospheric winds and high-frequency gravity-wave fluxes were made using the Ascension Island meteor radar (8° S, 14° W). The radar is a commercially-produced standard Skiymet system. It operated in an all-sky configuration with a peak power of 12 kW up until 2007, after which it was switched to 6 kW. It transmits at a frequency of 43.5 MHz. The data used in this study are for the period January 2002 to December 2007. The radar operated largely uninterrupted during this interval except for a period in late 2003/early 2004.

Although not originally designed to measure momentum fluxes, standard Skiymet systems nevertheless have a proven ability to do so (e.g. Hocking, 2005; Fritts et al., 2010; Vincent et al., 2010; Fritts et al., 2012; Andrioli et al., 2013a; de Wit et al., 2014; Placke et al., 2015), albeit with a lower temporal and spatial resolution than advanced systems specifically designed for this task (Fritts et al., 2012). The ability to estimate gravity-wave momentum fluxes ultimately relies on being able to separate the contributions to the radial velocity of each individual meteor made by gravity waves from the contributions made by background winds, tides and planetary waves. Incomplete removal of the background will thus tend to amplify the estimates of momentum flux, and so such estimates are likely to be an upper bound. A particular problem at low latitudes is that the diurnal tide can reach very large amplitudes in the mesosphere. Thus, if the diurnal tide is not fully accounted for, it will tend to lead to over-estimation of the momentum flux.

In this study, the local background wind for each meteor, including the tidal wind, was estimated and then removed by linearly interpolating the two–hourly–mean background wind to the time and height of each meteor. The method we use here is an alternative to that of Andrioli et al. (2013a) who employed a composite-day analysis to reduce the effects of tidal contamination.

Monthly-mean estimates of the zonal and meridional momentum fluxes, $< \overline{u'w'} >$ and $< \overline{v'w'} >$ respectively, are made in six height gates: 78–83 km; 83–86 km; 86–89 km; 89–92 km; 92–95km; 95–100km, which are centred on 82 km, 85 km, 88 km, 90 km, 93 km and 96 km respectively. A reduced number of meteors are detected in the uppermost and lowermost height gates, which makes flux estimates less reliable in these height gates. The change of the vertical flux of zonal momentum with height, z, combined with estimates of atmospheric density, ρ, from the US Standard Atmosphere (1976), thus provide an estimate of the zonal acceleration of the mean flow, a_{GW}, due

to the dissipation of gravity-waves (e.g. Fritts and Vincent, 1982) as per Equation 4.1.

$$a_{GW} = -\frac{1}{\rho}\frac{\partial(\rho < \overline{u'w'} >)}{\partial z} \tag{4.1}$$

A significant source of error on the estimates of wind, momentum flux and acceleration values is the zenith angle. Here we estimate errors in the radar measurements as follows. We assume a 1.5° error on the zenith angle (Hocking, 2005) and add this error to individual meteor zenith angles scaled by a pseudo-random Gaussian distribution centred on zero. Likewise, the error on the radial velocity of each meteor, which is the standard deviation of the values calculated from each antenna pair, is also added to the radial velocity of each meteor. The analysis was then run independently 25 times and the standard deviation of the wind, momentum flux and acceleration at each time is used as an estimation of the error on the winds, momentum fluxes and accelerations calculated in the original analysis.

Ascension Island is a low-latitude oceanic site, so it can be assumed that most of the observed high- and mid-frequency gravity-waves in the mesosphere will have been generated by convective sources within a few hundred kilometres of the island. In this study we assume that the majority of gravity waves that reach the mesosphere are from tropospheric sources rather than in-situ generation (Fritts and Alexander, 2003). Here, NOAA's outgoing long-wave radiation (OLR) and NASA's 3B42 V7 derived Tropical Rainfall Measurement Mission (TRMM) data-sets are used as proxies for this convective activity and rainfall, respectively, on the assumption that these will provide a crude measure of the strength of gravity-wave excitation. These data-sets are frequently used for this purpose (e.g. Alexander et al., 2008b; Wright et al., 2011, 2013). Lower OLR values are a consequence of low cloud-top temperatures that correspond to increased convective activity. The TRMM daily rainfall data are proportional to the latent heat release in tropospheric clouds, or, equivalently, the available energy in these convective systems.

The OLR data-set used provides daily values of OLR on a $2.5° \times 2.5°$ latitude-longitude grid that has been pre-processed to fill any gaps using temporal and spatial interpolation (Liebmann and Smith, 1996). The TRMM data-set gives daily mean rainfall on a $0.25° \times 0.25°$ grid between 50°N and 50°S (Huffman et al., 2007). In this study a local time series of both OLR and daily rainfall is calculated by taking the average daily value of the data within a $5° \times 5°$ latitude–longitude box centred on Ascension Island.

For comparison, a zonal mean time series of OLR and daily rainfall is also calculated around a 5° latitude band centred on Ascension Island. The typical monthly-mean uncertainties, estimated using the standard error on the mean, are 0.13 Wm^{-2} and 0.01 Wm^{-2} on OLR values and 0.006 mm day^{-1} and 0.025 mm day^{-1} on daily rainfall values for local and zonal conditions, respectively.

To investigate the zonal wind structure of the stratosphere we use European Centre for Medium Range Weather Forecasting (ECMWF) operational analysis data. The data used are from the 1.125° resolution data-set, available from 2000 to present. Data are available up to 64 km until February 2006 when the model was extended to 80 km. It should be noted that limited observational data is available above 40 km and thus the ECMWF data-set is less reliable above this height. However, on the monthly time-scales used here, these ECMWF data provide a good estimate of the underlying wave-filtering local to Ascension Island. A detailed description of this data-set can be found in Dee et al. (2011).

4.3 Results

To illustrate the intra-annual variability of the mesospheric winds, Figure 4.1 shows the annual time series of monthly-mean zonal wind at 85 km for each of the years used in this study. This monthly smoothing is applied to suppress the variation of the wind due to tides and planetary waves. The mean and standard deviation of the winds are indicated by the black line and grey filled areas, while the individual years, 2003–2007 are shown by the blue lines. There is a clear MSAO present, with maximum amplitudes of ≈ 30 ms^{-1} in both the eastward and westward phases. The MSAO is seen to have a larger amplitude during the first half of the year, in agreement with previous studies (e.g. Garcia et al., 1997).

The red line shows the monthly-mean zonal wind for 2002. From February to June the zonal wind is dramatically more westward than the other years considered. In particular, during this westward phase of the MSAO, peak zonal wind values reach ≈ -85 ms^{-1}. This is more than twice the magnitude of any other year in the dataset and far exceeds the typical variability indicated by the grey shading. This figure highlights the anomalous zonal winds during the first westward phase of the MSAO in 2002.

Figure 4.2 shows the monthly-mean zonal wind and zonal momentum flux for each of

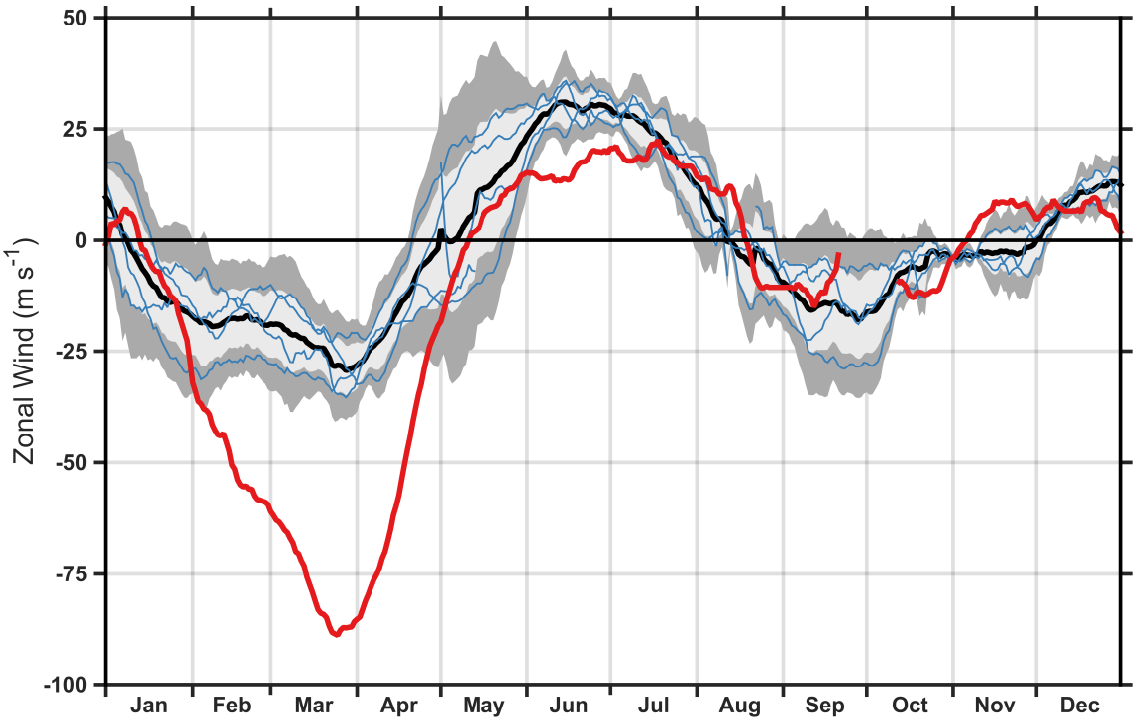

Figure 4.1: *Monthly-mean zonal wind over Ascension Island at a height of 85 km altitude during* $2002 - 2007$*. The thin blue lines are the zonal wind for each of the years* $2003 - 2007$ *and the mean for this period is shown by the thick black line. The light and dark grey filled areas show one and two standard deviations from the mean respectively. The thick red line shows the zonal wind for 2002.*

the height gates. The MSAO is the dominant signal in the zonal wind time series in the lower height gates, but becomes less significant with increasing height; this is seen as westward minima (maxima) peaking during March/April and September/October (June/July and December/January). This decrease in amplitude with height is particularly noticeable during 2002, where the magnitude of the westward zonal wind steadily changes from ≈ -85 ms^{-1} in the lowest height gate to ≈ -30 ms^{-1} in the uppermost height gate. This decrease can be observed during other years for the MSAO first phase westward maximum and also for the 2004 MSAO second phase westward maximum. In all years except 2002 and 2006 the MSAO signal becomes indistinguishable from the background above ≈ 90 km.

Momentum fluxes are mostly in the range -10 m^{2}s^{-2} to $+20$ m^{2}s^{-2}. Typical uncertainties on momentum flux estimates, not shown for reasons of clarity, range from $\sim \pm 2$ m^{2}s^{-2} in the middle height gates to $\sim \pm 7$ m^{2}s^{-2} in the uppermost and lowermost height gates where the meteor count rates are lower. These fluxes are consistent with those reported in other studies using meteor radars (e.g. Hocking, 2005; Antonita

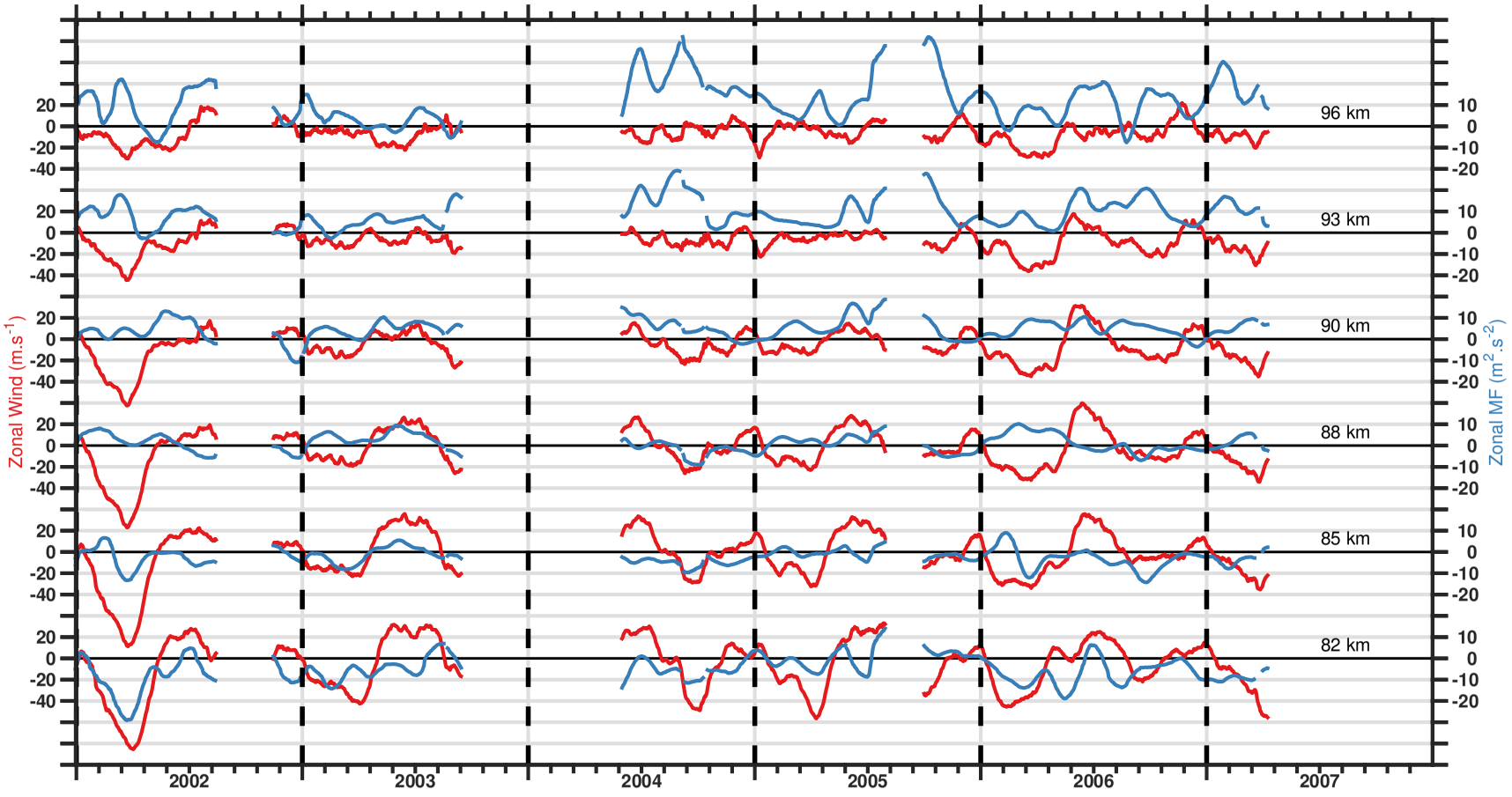

Figure 4.2: *Monthly-mean zonal wind (red) and zonal momentum flux (blue) for* $2002 - 2007$ *in six height gates. The horizontal black line is the* $0\ ms^{-1}$ *(left y-axis) and* $0\ m^2s^{-2}$ *(right y-axis) line for each height gate. The average height is shown above the zero line for each height gate.*

et al., 2008; Fritts et al., 2010; Vincent et al., 2010; de Wit et al., 2014; Placke et al., 2015). Zonal momentum flux becomes more eastward with increasing height in the mesosphere, suggesting a general transfer of westward momentum from the gravity waves to the mean flow. This is particularly evident at the time of the 2002 event in the lowest height gate.

Application of Equation 4.1 to the momentum fluxes in successive height gates allows an estimation of the acceleration of the winds due to the dissipation of gravity waves. Figure 4.3a shows monthly wave-induced zonal accelerations calculated between the height gates centred on 85 km and 88 km and the corresponding zonal wind. The times of the maximum westward wave-induced acceleration occurring during the first westward phase of the MSAO are highlighted by the black vertical dashed lines in each year (labelled A–D).

Strong westward wave-induced accelerations during the first westward phase of the MSAO are observed in 2002 (A), 2003 (B) and 2006 (D). Peak accelerations are -510 ± 76 ms^{-1}day^{-1}, -360 ± 81 ms^{-1}day^{-1}, -130 ± 45 ms^{-1}day^{-1} and -620 ± 57 ms^{-1}day^{-1} in A–D, respectively. At most other times the magnitude of accelerations are typically less than 300 ms^{-1}day^{-1}. While wave-induced accelerations of hundreds of ms^{-1}day^{-1} appear large, a number of other studies have reported similar values in the mesosphere. For example, de Wit et al. (2014) reported peak 10-day moving average accelerations between -240 ms^{-1}day^{-1} and $+140$ ms^{-1}day^{-1} using data from the Trondheim (63.4° N, 10.5° E) meteor radar during a major sudden stratospheric warming in January 2013. Similarly, Kovalam et al. (2006) used a combination of MF radar observations and model data at Christmas Island (2° N, 157° W) to estimate accelerations as large as 200 ms^{-1}day^{-1}.

Note that while the peak in the westward wave-induced acceleration during 2002 coincides well with the strongest westward winds, it is noticeable that even stronger accelerations occur at this height in 2006, but that no similar response is observed in the winds. Finally, we note that a small but significant increase in gravity-wave variance measured by the meteor radar occurred during the 2002 event (not shown for reasons of space). For example, at a height of 85 km, zonal variances increased to ~ 220 m^{2}s^2 compared to typical values at this height of ~ 160 m^{2}s^2.

To provide a crude estimate of the strength of excitation of gravity-waves near Ascension Island, two wave–generation proxies for convectively-generated gravity waves are considered. These are OLR (cloud-top temperature) and rainfall. Figure 4.3b shows monthly smoothed OLR and daily rainfall data averaged over a $5° \times 5°$ latitude–

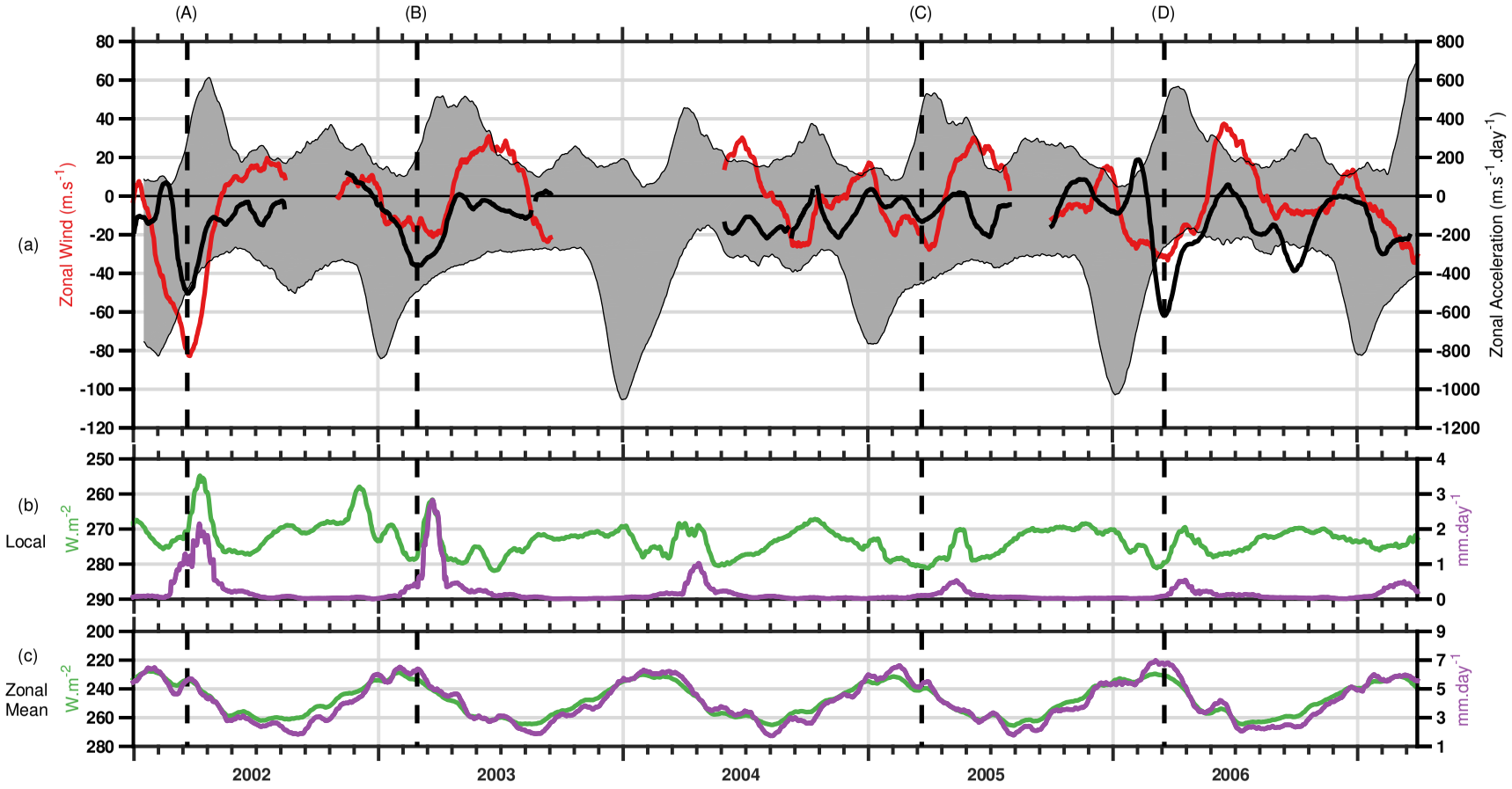

Figure 4.3: *Panel (a) shows monthly-mean zonal acceleration (black) calculated between height gates centred at 85 km and 88 km and corresponding monthly-mean zonal wind (red) for the period* $2002 - 2007$. *Grey shading marks the ECMWF maximum and minimum monthly-mean zonal winds between 0 km and 64 km. Panels (b) and (c) show monthly-mean OLR (green) and monthly-mean rainfall (purple) data for the same period averaged in (b) a local* $5° \times 5°$ *latitude–longitude box and (c) a zonal band of* $5°$ *latitude. In both panels (b) and (c) the region is centred on Ascension Island. Dashed lines A–D specify the time of peak westward accelerations during the first phase of the MSAO.*

longitude box centred on Ascension Island. Both a minimum in OLR and a maximum in daily rainfall is observed at about the same times as the MSAO events A–D, indicative of a maximum in convective activity. However, in all events, extrema in rainfall and OLR appear to lag the extrema in monthly-mean mesospheric zonal wind and momentum flux/mean-flow acceleration, indicating that the latter are not a response to the OLR/precipitation fluctuations. Figure 4.3c, shows the zonal-mean OLR and daily rainfall time series, calculated as a zonal mean around a 5° latitude band centred on Ascension Island. In contrast to the local OLR and daily rainfall, there is a clear regular annual cycle present with less inter-annual variability compared to the local time series. These results show that there is not a clear increase in the proxy for local gravity-wave excitation occurring at the time of any of the first phase MSAO events.

As mentioned in Section 4.1, the filtering of gravity waves by stratospheric winds has been proposed to play an important role in the inter-annual variability of the MSAO (Garcia et al., 1997). To investigate the significance of this wave filtering to event A in 2002, the grey shaded area in Figure 4.3a shows the range of zonal winds encountered by an ascending wave from the surface to a height of 64 km, estimated from ECMWF observational analyses data averaged over a $5° \times 5°$ latitude–longitude box centred on Ascension Island. The driving of the MSAO by gravity waves will be influenced by the fraction of those waves filtered out by these winds.

Lines A–D in Figures 4.3a highlight the times of maximum westward wave-induced accelerations during the first phase of the MSAO in each year. Using the ECMWF reanalysis data, the minimum/maximum zonal winds encountered by ascending gravity waves at A–D are -49/+28 ms^{-1}, -50/+22 ms^{-1}, -45/+44 ms^{-1} and -26/+44 ms^{-1}, respectively. This is significant because it suggests that, at least for waves ascending to 64 km, there is no significant difference in the filtering from the winds during events A–D when the full range of heights are considered. In other words, the anomalous winds in event A in 2002 are probably not the result of a reduced wave filtering in comparison to other years (i.e. in disagreement to the proposed mechanism of Garcia and Sassi (1999)).

Vertical profiles of monthly-mean mesospheric zonal wind and wave-induced acceleration at the times specified by lines A–D in Figure 4.3, are shown in Figure 4.4. The figure shows that there is a general tendency for accelerations and winds to become more eastward with height in all years. This is particularly evident in 2002 when the change in zonal wind and acceleration between the lowest and highest height gate is > 30 ms^{-1} and > 600 $ms^{-1}day^{-1}$, respectively. In addition, the enhanced westward

acceleration observed in Figure 4.3 in 2006 appears to have occurred at a particular altitude and not at multiple heights as in 2002. These results highlight the connection between strong westward accelerations and strong westward winds during event A in 2002.

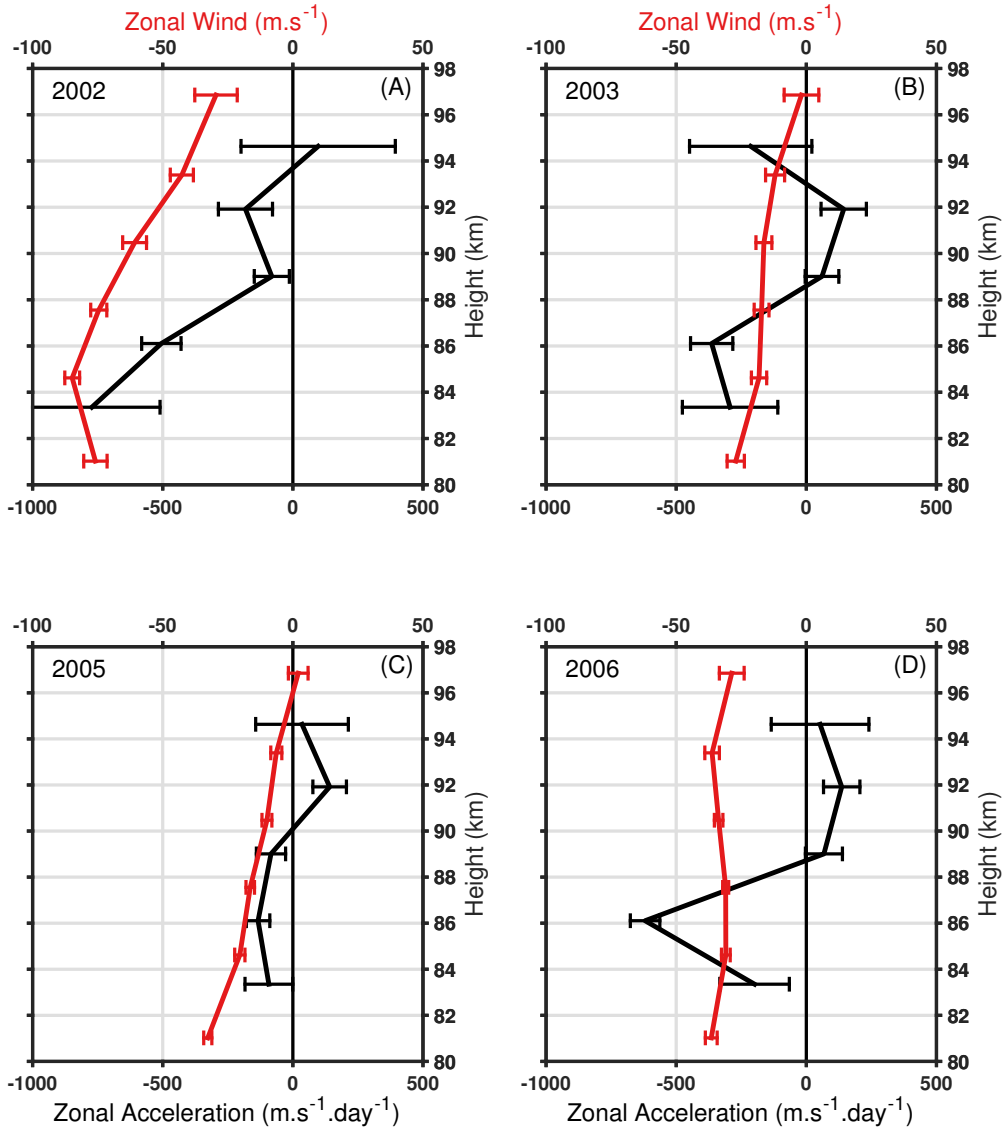

Figure 4.4: *Variation of monthly-mean zonal wind (red) and monthly-mean zonal acceleration (black) with height at the time of maximum acceleration during the first westward phase of the MSAO for (A) 2002, (B) 2003, (C) 2004 and (D) 2005. The errors on wind values have been multiplied by 10 to make them more visible here.*

4.4 Discussion and Conclusion

For the first time, measurements from the Ascension Island meteor radar are used to calculate zonal momentum fluxes and zonal-wind accelerations due to high-frequency mesospheric gravity waves. Considering the first phase of the MSAO in 2002, we note that:

1. Anomalous and strong westward winds were observed.
2. An increase in westward momentum fluxes and westward acceleration due to high-frequency gravity waves is observed to accompany the anomalous zonal winds, strongly suggesting that these waves are responsible for the anomalous winds, in agreement with the proposed selective filtering mechanism of Garcia and Sassi (1999).
3. However, the ECMWF reanalysis data ($0 - 64$ km) suggests that the winds encountered by ascending waves in 2002 were actually no more favourable for propagation to the mesosphere than in other years, which is not in agreement with the selective filtering mechanism.
4. Further, in 2002 no indication of anomalous gravity-wave excitation is provided by the OLR/precipitation proxies.

Collectively, these observations do not support the selective filtering mechanism of Garcia and Sassi (1999) for the 2002 anomalous event because the strong winds, fluxes and wave-induced accelerations do not appear to result from unusual filtering conditions. We note that the winds considered here cover a greater height range than those considered by Garcia et al. (1997), Garcia and Sassi (1999) and Day and Mitchell (2013), i.e. $0 - 64$ km here c.f. $0 - 32$ km in the earlier studies and it is only when this greater height range is considered that the filtering conditions in 2002 are seen to be not significantly different from the other years. In addition, the winds we consider are also geographically located over Ascension Island and, in combination with the increased range of heights considered, hence, represent a more realistic view of the winds encountered by ascending waves. Our observations thus do not provide a clear indication as to the origin of the increased gravity-wave fluxes associated with the 2002 event.

The first phase MSAO event in 2006 was accompanied by strong gravity-wave accelerations but did not display the anomalous westward winds observed in 2002. Again,

there is no clear indication the propagation environment was significantly different during this event. It is worth noting that the strong acceleration in 2006 is only observed at a single altitude and not at multiple heights as in 2002.

The evidence here thus suggests that episodes of strong westward fluxes/accelerations from high-frequency gravity waves can occur in the equatorial mesosphere without the need for obviously unusual wind filtering conditions in the underlying atmosphere. Further, the 2006 event demonstrates that strong westward fluxes/accelerations do not necessarily produce anomalous westward winds. This latter phenomena may indicate a significant role from other waves not detected by the meteor radar. These waves might include, low- and medium- frequency gravity waves not detected by the radar analysis, planetary waves (including Kelvin waves) and tides. Further, we note that 2002 saw the only stratospheric warming to be observed in the southern hemisphere, albeit later in the year it has been suggested to be the result of anomalous planetary wave activity during 2002.

A plausible explanation is that Kelvin wave induced accelerations may inhibit the accelerations due to gravity waves in years such as 2006. However, only ultra-fast Kelvin waves have significant amplitudes in the mesosphere and these are observed to have much smaller accelerations than the gravity-wave accelerations we observe (Chen and Miyahara, 2012; Davis et al., 2012). For example, Davis et al. (2012) observed peak 5-day mean ultra-fast Kelvin wave accelerations of 4 $ms^{-1}day^{-1}$ using the Ascension Island meteor radar and Chen and Miyahara (2012) found the range of accelerations in a year to be between 0.5 to 8 $ms^{-1}day^{-1}$ using the Kyushu University Middle Atmosphere General Circulation Model. Thus, it is unlikely that Kelvin-wave induced accelerations are responsible for the absent strong winds in 2006.

The observations presented here highlight the importance of gravity waves in the equatorial mesosphere. Our results indicate that gravity-wave fluxes/accelerations are closely associated with anomalous MSAO wind events, but the relationship between wave excitation, propagation and dissipation and the zonal winds is complex and includes many uncertainties - highlighting the need for further observations able to address a wide range of wave parameters.

Chapter 5

Summary and Further Work

The work presented in this thesis has provided a novel contribution to answering some of the important questions raised in attempts to understand the wave dynamics of the equatorial mesosphere. This final chapter will summarise the work presented and mention some of the other research contributions the author has made in parallel to this work. A number of possible further research opportunities are also proposed as suggestions for further work.

5.1 Summary of Key Results

This work has contributed to the understanding of gravity waves in the equatorial stratosphere and mesosphere. The main conclusions are summarised below.

The Contribution of the MJO to the Stratospheric Gravity-Wave Field

1. Presented the first observations of a large-scale MJO signature in tropical stratospheric gravity-wave energy.
2. Demonstrated that there is a strong anti-correlation between MJO-bandpassed gravity-wave energies and 200 hPa zonal winds (i.e. greater gravity-wave energies when the zonal-wind anomalies are westward), suggesting the MJO dynamically influences the fluxes of stratospheric gravity-waves.
3. Provided evidence to show that the MJO modulates stratospheric gravity wave fluxes through critical level wave-filtering.
4. Highlighted the importance of tropospheric processes in influencing the stratospheric gravity-wave field.

Gravity Waves and the Mesospheric Semi-Annual Oscillation

1. Gravity-wave momentum fluxes were measured for the first time using the Ascension Island meteor radar.
2. Measured large gravity-wave momentum fluxes and accelerations coincident with an anomalous MSAO wind event in 2002 using the Ascension Island meteor radar.
3. No unusual wave-filtering conditions were observed, in contradiction to current theory, and no significant increase in wave-excitation proxies were found.
4. In addition, large gravity-wave momentum fluxes and accelerations were also measured in 2006, when no anomalous MSAO wind event occurred.
5. Demonstrated that there is a close association between gravity-wave momentum fluxes and accelerations, and the anomalous MSAO wind event. However, the relationship between wave excitation, propagation and dissipation, and the zonal winds, is complex and contradicts the previous theory.

5.2 Additional Research Contributions

In addition to the work presented here, the author has contributed to additional studies that have led to or are in preparation for publication. These are briefly summarised below.

5.2.1 Multi-Instrument Gravity-Wave Measurements

Wright, C. J., Hindley, N. P., **Moss, A. C.**, Fritts, D. C., Janches D., and Mitchell, N. J.: Multi-instrument gravity-wave measurements over Tierra del Fuego and the Drake Passage Part 1: Potential energies and vertical wavelengths from AIRS, COSMIC, HIRDLS, MLS-Aura, SAAMER, SABER and radiosondes, Atmos. Meas. Tech., 9, 877–908, 2016.

Abstract: Gravity waves in the terrestrial atmosphere are a vital geophysical process, acting to transport energy and momentum on a wide range of scales and to couple the various atmospheric layers. Despite the importance of these waves, the many studies to date have often exhibited very dissimilar results, and it remains unclear whether these differences are primarily instrumental or methodological. Here, we address this problem by comparing observations made by a diverse range of the most widely used gravity-wave-resolving instruments in a common geographic region around the southern Andes and Drake Passage, an area known to exhibit strong wave activity. Specifically, we use data from three limb-sounding radiometers (Microwave Limb Sounder, MLS-Aura; HIgh Resolution Dynamics Limb Sounder, HIRDLS; Sounding of the Atmosphere using Broadband Emission Radiometry, SABER), the Constellation Observing System for Meteorology, Ionosphere and Climate (COSMIC) GPS-RO constellation, a ground-based meteor radar, the Advanced Infrared Sounder (AIRS) infrared nadir sounder and radiosondes to examine the gravity wave potential energy (GWPE) and vertical wavelengths (λ_z) of individual gravity-wave packets from the lower troposphere to the edge of the lower thermosphere ($\sim$ 100 km). Our results show important similarities and differences. Limb sounder measurements show high intercorrelation, typically > 0.8 between any instrument pair. Meteor radar observations agree in form with the limb sounders, despite vast technical differences. AIRS and radiosonde observations tend to be uncorrelated or anticorrelated with the other data sets, suggesting very different behaviour of the wave field in the different spectral regimes accessed by each instrument. Evidence of wave dissipation is seen, and varies strongly with season. Observed GWPE for individual wave packets exhibits a

log-normal distribution, with short-timescale intermittency dominating over a well-repeated monthly-median seasonal cycle. GWPE and λ_z exhibit strong correlations with the stratospheric winds, but not with local surface winds. Our results provide guidance for interpretation and intercomparison of such data sets in their full context.

The author contributed to the calculations of gravity-wave variance and momentum flux from the Southern Argentina Agile Meteor Radar located at Rio Grande, Argentina, and contributed to the interpretation of the results. Additionally, part 2 of this work, focussing on momentum flux measurements, is in preparation for publication.

5.2.2 The South Georgia Wave Experiment (SG-WEX)

Recent satellite observations have suggested that small mountainous islands that lie in regions of strong winds can be an intense source of orographic gravity-waves. The momentum deposition from these waves is believed to contribute significantly to the dynamics of the stratosphere and mesosphere. The small island of South Georgia (55° S, 37° W), which lies in the strong winds of the south Atlantic, is believed to be the most intense source of such waves (e.g. Alexander et al., 2009). Most global climate and numerical weather prediction models do not resolve or parameterise the contributions from these sub-grid scale islands (e.g. Alexander et al., 2009). Thus, studies of gravity-waves properties and intermittency from these small island sources are important for improving the accuracy of these models.

The UK Natural Environment Research Council funded SG-WEX research grant awarded to the University of Bath, University of Leeds, British Antarctic Survey and the UK Meteorological Office aims to answer five fundamental questions about the role of South Georgia as an intense and isolated source of gravity-waves. These are listed below.

1. What is the nature of gravity waves generated by South Georgia and what is their variability?

2. What is the contribution of these gravity waves to the total field of gravity waves over the South Atlantic?

3. What is the influence of gravity waves from South Georgia on the mesosphere?

4. How can these observations be used to improve gravity-wave drag parametrisations in models?

5. How important is South Georgia in comparison to other gravity-wave sources and how does it impact local winds and the development of synoptic systems?

As part of the SG-WEX research project, two radiosonde campaigns were undertaken to characterise the nature of gravity waves in the troposphere and lower stratosphere over South Georgia. The author contributed to the first of these fieldwork campaigns in January 2015. An analysis of the data from the two radiosonde campaigns, at the time of writing, are being prepared for publication, led by Dr Tracy Moffat-Griffin of the British Antarctic Survey.

Another part of the SG-WEX research project was to install a meteor radar on at the British Antarctic Survey King Edward Point research station. The radar was installed in February 2016 and the author has contributed to preliminary analysis of these data.

5.2.3 Anomalously Low Polar Mesospheric Cloud Frequency in the Southern Hemisphere 2014/15 Season

A fascinating phenomena of the polar mesosphere is that clouds form close to the mesopause ($\sim$ 80 km) around the summer solstices. These polar mesospheric clouds are also known as noctilucent (night-shining) clouds when observed from the ground, but can be observed at all hours from space (e.g. Thurairajah et al., 2013). They occur as a consequence of the dynamically driven cooling of the summer mesopause (Lindzen, 1981), causing the formation of ice when the temperatures fall low enough (e.g. Cho and Röttger, 1997), and their occurrence can also be affected by the perturbations in temperature from ascending waves (Kirkwood et al., 2002).

A striking change in the occurrence frequency of polar mesospheric clouds was observed during the southern hemisphere summer season in 2014/15. In this season a large drop in the occurrence frequency was observed around 20 days after the solstice, significantly differing from the climatological norm, as presented in Figure 5.1.

Figure 5.1 shows the abundance of polar mesospheric clouds, calculated using data from the Cloud Imaging and Particle Size (CIPS) instrument on the Aeronomy of Ice in the Mesosphere (AIM) satellite, for 120 days around the southern hemisphere

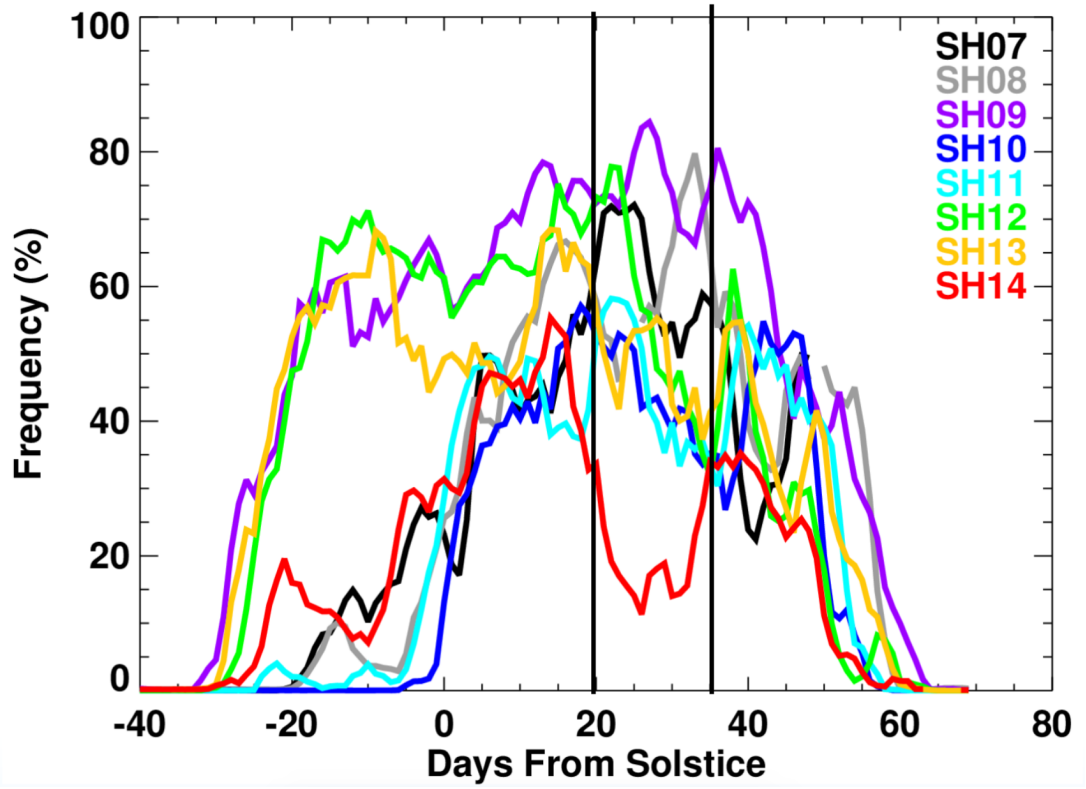

Figure 5.1: *The Cloud Imaging and Particle Size (CIPS) instrument ascending node daily polar mesospheric cloud frequency at 80° S for southern hemisphere seasons from 2007/8 to 2014/15. Note the significant drop at around 20 days after the solstice in the 2014/15 season, significantly different from all other seasons shown. From (Randall, 2015, private communication), also printed online at spaceweather.com.*

summer solstice for the seasons 2007/8–2014/15 (Randall, 2015, private communication). The departure from the climatological mean during the 2014/15 season, shown in red, is clearly evident from around 20–35 days after the solstice; the time at which the cloud occurrence usually reaches its peak.

The global meridional circulation of air in the atmosphere is known as the Brewer-Dobson circulation (Brewer, 1949). In the lower stratosphere, below 30 km, air from the equator ascends and flows poleward where it descends, whereas in the mesosphere, air ascends over the summer pole and descends over the winter pole (Murgatroyd and Singleton, 1961). This circulation is driven by the momentum deposition of breaking waves in the stratosphere and mesosphere (e.g. Roscoe, 2006). The cold summer mesopause results from the adiabatic cooling of air as it ascends over the summer pole as part of this circulation. Thus, a slowing of the circulation, could lead to warmer temperatures over the winter pole and a resultant decrease in the occurrence frequency of polar mesospheric clouds.

Figure 5.2 presents the 5-day mean meridional winds over Rothera (68° S, 68° W) at 90 km. A significant departure from the climatological mean in 2014/15 is observed at about 20 days after the summer solstice. The slowing of the meridional circulation begins just after the solstice, and falls to near 0 ms^{-1} at approximately the same time as the minimum occurrence frequency in polar mesospheric clouds occurs.

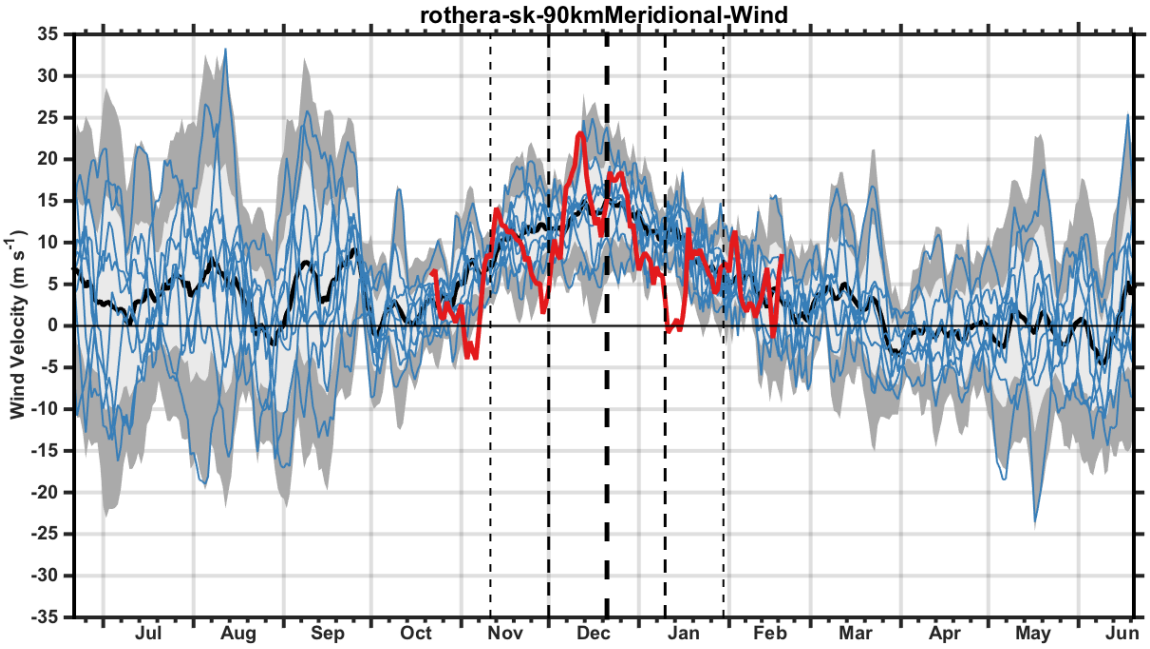

Figure 5.2: *5-day mean meridional winds at 90 km from the Rothera meteor radar (68° S, 68° W) for PMC seasons 2006/7 – 2014/15. The central thick black dashed line indicates the solstice, and the two lines either side indicate 20 and 40 days from the solstice, respectively. The thin blue lines are the meridional winds for PMC seasons 2006/7 – 2013/14 and the thick black line, and light and dark grey shading represent the mean, and one and two standard deviations of the meridional wind for these PMC seasons. The thick red line is the meridional winds observed in the 2014/15. Note the rapid deceleration of the meridional flow at around 20 days after the solstice in this season, coincident with the drop in PMC frequency observed in Figure 5.1.*

The strength of this meridional circulation of the mesosphere is dominated by the momentum deposition from ascending gravity waves (Karlsson et al., 2007). This has led to the suggestion of an inter-hemispheric coupling (IHC) mechanism, whereby tropospheric planetary-wave activity modulates the circulation and modulates the gravity-wave momentum deposition in the mesosphere, thus modulating the meridional flow (e.g. Karlsson et al., 2007). However, recent work by Siskind and McCormack (2014), suggests that momentum forcing by the quasi-two-day-wave provides an important contribution to the momentum forcing, that thus governs the PMC variability.

The possible causes of the slowing of the meridional circulation and drop in polar mesospheric cloud occurrence presented in Figures 5.1 and 5.2 are currently under investigation. The author has contributed to the analysis of data from meteor radars at Rothera and Sodankyla (67° N, 27° E), and also data from the Microwave Limb Sounder (MLS) on NASA's Aura satellite.

5.3 Suggestions for Future Work

The results presented here have highlighted the importance of gravity waves in the dynamic coupling of the atmosphere. A number of suggestions for future research projects are provided below.

1. **Does the El Niño Southern Oscillation Modulate Stratospheric Gravity Waves?**

   The results presented in Chapter 3 demonstrated that the MJO, the dominant component of intra-seasonal variability in the tropical troposphere, contributed to the flux of stratospheric gravity-waves. On inter-annual time-scales, the tropical troposphere is dominated by the El Niño Southern Oscillation (ENSO). El Niño and La Niña ENSO phases are associated with regions of enhanced sea-surface temperatures (e.g. Clarke, 2014), which would lead to regions of enhanced and suppressed convective activity. Thus, it would be interesting to ask the same question of ENSO variability; *"Does the El Niño Southern Oscillation Modulate Stratospheric Gravity Waves?"*

2. **Comparison of Momentum Flux Measurements from Low-Latitude Meteor Radars**

   The results presented in Chapter 4 highlighted the need for further observations in order to understand the influence of gravity-waves on the MSAO and also on anomalous first phase MSAO events. A number of additional meteor radars are situated at low-latitude sites in India, Indonesia and South America. This provides an opportunity to explore the longitudinal structure of the MSAO and to characterise the influence of gravity waves in driving the MSAO.

3. **Does Stratospheric Gravity Wave Activity Exhibit a Global-Scale Diurnal Cycle?**

   A diurnal cycle in gravity-wave activity in the mesosphere at low- and mid-latitudes was recently reported on by Andrioli et al. (2013a), using three meteor radars. These results suggested strong gravity-wave-tidal interactions, but in the stratosphere tidal amplitudes are much smaller. However, a strong diurnal cycle is also observed in rainfall and convective intensity (e.g. Nesbitt and Zipser, 2003), and thus the convective sources of gravity waves. It would be interesting to determine whether a diurnal cycle in gravity-wave exists in the stratosphere on a global scale, and also whether this results from variability in wave sources or from gravity-wave-tidal interactions. Gravity wave properties calculated from COSMIC RO observations would be ideal for this, as a result of the pseudo-random coverage resulting from the multiple orbits of the GPS and COSMIC satellites.

5.4 Final Note

Gravity waves play a fundamental role in controlling the circulation of the stratosphere and mesosphere. The work presented here has highlighted the role of gravity waves in coupling the large-scale processes that exist in different layers of the atmosphere. The MJO has been shown to influence gravity-wave activity in the stratosphere through critical-level filtering and gravity-waves have been shown to contribute to the driving of the MSAO. However, a number of unanswered fundamental questions remain, and further research is needed to fully understand the sources, propagation and influences of gravity waves in the atmosphere.

.

Bibliography

Alexander, M. J., Gille, J., Cavanaugh, C., Coffey, M., Craig, C., Eden, T., Francis, G., Halvorson, C., Hannigan, J., Khosravi, R., Kinnison, D., Lee, H., Massie, S., Nardi, B., Barnett, J., Hepplewhite, C., Lambert, A., and Dean, V. Global estimates of gravity wave momentum flux from High Resolution Dynamics Limb Sounder observations. *Journal of Geophysical Research: Atmospheres*, 113(D15), 2008a. doi: 10.1029/2007JD008807.

Alexander, M. J., Eckermann, S. D., Broutman, D., and Ma, J. Momentum flux estimates for South Georgia Island mountain waves in the stratosphere observed via satellite. *Geophysical Research Letters*, 36(12), 2009. doi: 10.1029/2009GL038587.

Alexander, M. J., Geller, M., McLandress, C., Polavarapu, S., Preusse, P., Sassi, F., Sato, K., Eckermann, S., Ern, M., Hertzog, A., Kawatani, Y., Pulido, M., Shaw, T. A., Sigmond, M., Vincent, R., and Watanabe, S. Recent developments in gravity-wave effects in climate models and the global distribution of gravity-wave momentum flux from observations and models. *Quarterly Journal of the Royal Meteorological Society*, 136(650):1103–1124, 2010. doi: 10.1002/qj.637.

Alexander, S. P., Tsuda, T., Kawatani, Y., and Takahashi, M. Global distribution of atmospheric waves in the equatorial upper troposphere and lower stratosphere: COSMIC observations of wave mean flow interactions. *Journal of Geophysical Research: Atmospheres*, 113(D24), 2008b. doi: 10.1029/2008JD010039.

Alexander, S. P., Klekociuk, A. R., and Tsuda, T. Gravity wave and orographic wave activity observed around the Antarctic and Arctic stratospheric vortices by the COSMIC GPS-RO satellite constellation. *J. Geophys. Res. Atmos.*, 114(D17), 2013.

Andrews, D. G., Holton, J. R., and Leovy, C. B. *Middle Atmosphere Dynamics*. International geophysics series. Academic Press, 1987. ISBN 9780120585755.

Andrioli, V. F., Fritts, D. C., Batista, P. P., and Clemesha, B. R. Improved analysis of all-sky meteor radar measurements of gravity wave variances and momentum fluxes. *Annales Geophysicae*, 31:889–908, 2013a.

Andrioli, V. F., Fritts, D. C., Batista, P. P., Clemesha, B. R., and Janches, D. Diurnal variation in gravity wave activity at low and middle latitudes. *Annales Geophysicae*, 31(11):2123–2135, 2013b. doi: 10.5194/angeo-31-2123-2013.

Andrioli, V. F., Batista, P. P., Clemesha, B. R., Schuch, N. J., and Buriti, R. A. Multi-year observations of gravity wave momentum fluxes at low and middle latitudes inferred by all-sky meteor radar. *Annales Geophysicae*, 33(9):1183–1193, 2015. doi: 10.5194/angeo-33-1183-2015.

Anthes, R. A., Ector, D., Hunt, D. C., Kuo, Y-H., Rocken, C., Schreiner, W. S., S. V. SyndergaardSokolovskiy, S., Wee, T-K., and Zeng, Z. The COSMIC/FORMOSAT-3 Mission: Early Results. *Bull. Amer. Meteor. Soc.*, 89: 313–333, 2008. doi: 10.1175/BAMS-89-3-313.

Antonita, T. M., Ramkumar, G., Kumar, K. K., and Deepa, V. Meteor wind radar observations of gravity wave momentum fluxes and their forcing toward the Mesospheric Semiannual Oscillation. *Annales Geophysicae*, 113(D10), 2008.

Baldwin, M. P., Gray, L. J., Dunkerton, T. J., Hamilton, K., Haynes, P. H., Randel, W. J., Holton, J. R., Alexander, M. J., Hirota, I., Horinouchi, T., Jones, D. B. A., Kinnersley, J. S., Marquardt, C., Sato, K., and Takahashi, M. The quasi-biennial oscillation. *Reviews of Geophysics*, 39(2):179–229, 2001. doi: 10.1029/1999RG000073.

Baumgarten, G., Fiedler, J., Hildebrand, J., and Lübken, F-J. Inertia gravity wave in the stratosphere and mesosphere observed by Doppler wind and temperature lidar. *Geophysical Research Letters*, 42(24):10,929–10,936, 2015. doi: 10.1002/2015GL066991.

Beres, J. H., Garcia, R. R., Boville, B. A., and Sassi, F. Implementation of a gravity wave source spectrum parameterization dependent on the properties of convection in the Whole Atmosphere Community Climate Model (WACCM). *Journal of Geophysical Research: Atmospheres*, 110(D10), 2005. doi: 10.1029/2004JD005504.

Bhatla, R., Singh, M., and Pattanaik, D. R. Impact of Madden-Julian oscillation on onset of summer monsoon over India. *Theoretical and Applied Climatology*, pages 1–11, 2016. doi: 10.1007/s00704-015-1715-4.

Bossert, K., Fritts, D. C., Pautet, P-D, Taylor, M. J., Williams, B. P., and Pendelton, W. R. Investigation of a mesospheric gravity wave ducting event using coordinated sodium lidar and Mesospheric Temperature Mapper measurements at ALOMAR, Norway (69° N). *Journal of Geophysical Research: Atmospheres*, 119(16):9765–9778, 2014. doi: 10.1002/2014JD021460.

Brasseur, G. P. and Solomon, S. *Aeronomy of the Middle Atmosphere: Chemistry and Physics of the Stratosphere and Mesosphere*. Atmospheric and Oceanographic Sciences Library. Springer, 3rd edition, 2005. ISBN 9781402032844.

Brewer, A. W. Evidence for a world circulation provided by the measurements of helium and water vapour distribution in the stratosphere. *Quarterly Journal of the Royal Meteorological Society*, 75(326):351–363, 1949. doi: 10.1002/qj.49707532603.

Burrage, M. D., Vincent, R. A., Mayr, H. G., Skinner, W. R., Arnold, N F., and Hays, P. B. Long-term variability in the equatorial middle atmosphere zonal wind. *Journal of Geophysical Research: Atmospheres*, 101(D8):12847–12854, 1996.

Ceplecha, Z., Borovička, J., Elford, W. G., ReVelle, D. O., Hawkes, R. L., Porubčan, V., and Šimek, M. Meteor Phenomena and Bodies. *Space Science Reviews*, 84(3): 327–471, 1998. doi: 10.1023/A:1005069928850.

Chen, Y-W. and Miyahara, S. Analysis of fast and ultrafast Kelvin waves simulated by the Kyushu-GCM. *Journal of Atmospheric and Solar-Terrestrial Physics*, 80: 1–11, 2012.

Cheng, C.-Z., Kuo, Y.-H., Anthes, R. A., and Wu, L. Satellite constellation monitors global and space weather. *Eos, Transactions American Geophysical Union*, 87(17): 166–166, 2006. doi: 10.1029/2006EO170003.

Cho, J. Y. N. and Röttger, J. An updated review of polar mesosphere summer echoes: Observation, theory, and their relationship to noctilucent clouds and subvisible aerosols. *Journal of Geophysical Research: Atmospheres*, 102(D2):2001–2020, 1997. doi: 10.1029/96JD02030.

Clark, T. L., Hauf, T., and Kuettner, J. P. Convectively forced internal gravity waves: Results from two-dimensional numerical experiments. *Quarterly Journal of the Royal Meteorological Society*, 112(474):899–925, 1986. doi: 10.1002/qj.49711247402.

Clarke, A. J. El Niño Physics and El Niño Predictability. *Annual Review of Marine Science*, 6(1):79–99, 2014. doi: 10.1146/annurev-marine-010213-135026.

CLIVAR, Madden-Julian Oscillation Working Group:. MJO Simulation Diagnostics. *J. Geophys. Res. Atmos.*, 22(3006–3030), 2009.

Das, S. S., Uma, K. N., and Das, S. K. MST radar observations of short-period gravity wave during overhead tropical cyclone. *Radio Science*, 47(2), 2012. doi: 10.1029/2011RS004840.

Davis, R. N., Chen, Y.-W., Miyahara, S., and Mitchell, N. J. The climatology, propagation and excitation of ultra-fast Kelvin waves as observed by meteor radar, Aura MLS, TRMM and in the Kyushu-GCM. *Atmospheric Chemistry and Physics*, 12(4):1865–1879, 2012. doi: 10.5194/acp-12-1865-2012.

Davis, R. N., Du, J., Smith, A. K., Ward, W. E., and Mitchell, N. J. The diurnal and semidiurnal tides over Ascension Island (8°S, 14°W) and their interaction with the stratospheric quasi-biennial oscillation: studies with meteor radar, eCMAM and WACCM. *Atmospheric Chemistry and Physics*, 13(18):9543–9564, 2013. doi: 10.5194/acp-13-9543-2013.

Day, K. A. and Mitchell, N. J. The climatology, propagation and excitation of ultra-fast Kelvin waves as observed by meteor radar, Aura MLS, TRMM and in the Kyushu-GCM. *Atmospheric Chemistry and Physics*, 13(18):9515–9523, 2013.

de Wit, R. J., Hibbins, R. E., Espy, P. J., and Mitchell, N. J. Interannual variability of mesopause zonal winds over Ascension Island: Coupling to the stratospheric QBO. *Journal of Geophysical Research: Atmospheres*, 118(21):12,052–12,060, 2013. doi: 10.1002/2013JD020203.

de Wit, R. J., Hibbins, R. E., Espy, P. J., Orsolini, Y. J., Limpasuvan, V., and Kinnison, D. E. Observations of gravity wave forcing of the mesopause region during the January 2013 major Sudden Stratospheric Warming. *Geophysical Research Letters*, 41(13):4745–4752, 2014.

de Wit, R. J., Janches, D., Fritts, D. C., and Hibbins, R. E. QBO modulation of the mesopause gravity wave momentum flux over Tierra del Fuego. *Geophysical Research Letters*, 2016. doi: 10.1002/2016GL068599.

Dee, D. P., Uppala, S. M., Simmons, A. J., Berrisford, P., Poli, P., Kobayashi, S., Andrae, U., Balmaseda, M. A., Balsamo, G., Bauer, P., Bechtold, P., Beljaars, A. C. M., van de Berg, L., Bidlot, J., Bormann, N., Delsol, C., Dragani, R., Fuentes, M., Geer, A. J., Haimberger, L., Healy, S. B., Hersbach, H., Hólm, E. V., Isaksen, L., Kållberg, P., Köhler, M., Matricardi, M., McNally, A. P., Monge-Sanz, B. M.,

Morcrette, J. J., Park, B. K., Peubey, C., de Rosnay, P., Tavolato, C., Thépaut, J. N., and Vitart, F. The ERA-Interim reanalysis: configuration and performance of the data assimilation system. *Q.J.R. Meteorol. Soc.*, 137:553–597, 2011.

Delisi, D. P. and Dunkerton, T. J. Seasonal Variation of the Semiannual Oscillation. *Journal of the Atmospheric Sciences*, 45(19):2772–2787, 1988. doi: 10.1175/1520-0469(1988)045⟨2772:SVOTSO⟩2.0.CO;2.

Dhaka, S. K., Takahashi, M., Shibagaki, Y., Yamanaka, M. D., and Fukao, S. Gravity wave generation in the lower stratosphere due to passage of the typhoon 9426 (Orchid) observed by the MU radar at Shigaraki (34.85° N, 136.10° E). *Journal of Geophysical Research: Atmospheres*, 108(D19), 2003. doi: 10.1029/2003JD003489.

Dick, S. J. Observation and interpretation of the Leonid meteors over the last millennium. *Journal of Astronomical History and Heritage*, 1:1–20, 1998.

Duchon, C. E. Lanczos filtering in one and two dimensions. *J. Appl. Meteor.*, 18: 1016–1022, 1979.

Dunkerton, T. J. Theory of the mesopause semiannual oscillation. *J. Atmos. Sci.*, 39:2681–2680, 1982.

Dunkerton, T. J. Inertia-Gravity Waves in the Stratosphere. *Journal of the Atmospheric Sciences*, 41(23):3396–3404, 1984. doi: 10.1175/1520-0469(1984)041⟨3396:IWITS⟩2.0.CO;2.

Dunkerton, T. J. The role of gravity waves in the quasi-biennial oscillation. *Journal of Geophysical Research: Atmospheres*, 102(D22):26053–26076, 1997. doi: 10.1029/96JD02999.

Eckermann, S. D., Hirota, I., and Hocking, W. K. Gravity wave and equatorial wave morphology of the stratosphere derived from long-term rocket soundings. *Quarterly Journal of the Royal Meteorological Society*, 121(521):149–186, 1995. doi: 10.1002/qj.49712152108.

Eckermann, S. D., Rajopadhyaya, D. K., and Vincent, R. A. Intraseasonal wind variability in the equatorial mesosphere and lower thermosphere: Long-term observations from the central Pacific. *Journal of Atmospheric and Solar-Terrestrial Physics*, 59(6):603–627, 1997.

Efron, B. Bootstrap Methods: Another Look at the Jackknife. *Ann. Statist.*, 7(1): 1–26, 1979. doi: 10.1214/aos/1176344552.

Ern, M., Preusse, P., Krebsbach, M., Mlynczak, M. G., and Russell III, J. M. Equatorial wave analysis from SABER and ECMWF temperatures. *Atmospheric Chemistry and Physics*, 8(4):845–869, 2008. doi: 10.5194/acp-8-845-2008.

Ern, M., Preusse, P., Gille, J. C., Hepplewhite, C. L., Mlynczak, M. G., Russell III, J. M., and Riese, M. Implications for atmospheric dynamics derived from global observations of gravity wave momentum flux in stratosphere and mesosphere. *Journal of Geophysical Research: Atmospheres*, 116(D19), 2011. doi: 10.1029/2011JD015821.

Ern, M., Ploeger, F., Preusse, P., Gille, J. C., Gray, L. J., Kalisch, S., Mlynczak, M. G., Russell III, J. M., and Riese, M. Interaction of gravity waves with the QBO: A satellite perspective. *Journal of Geophysical Research: Atmospheres*, 119 (5):2329–2355, 2014. doi: 10.1002/2013JD020731.

Ern, M., Preusse, P., and Riese, M. Driving of the SAO by gravity waves as observed from satellite. *Annales Geophysicae*, 33(4):483–504, 2015. doi: 10.5194/angeo-33-483-2015.

Espy, P. J., Hibbins, R. E., Swenson, G. R., Tang, J., Taylor, M. J., Riggin, D. M., and Fritts, D. C. Regional variations of mesospheric gravity-wave momentum flux over Antarctica. *Annales Geophysicae*, 24(1):81–88, 2006. doi: 10.5194/angeo-24-81-2006.

Faber, A., Llamedo, P., Schmidt, T., de la Torre, A., and Wickert, J. On the determination of gravity wave momentum flux from GPS radio occultation data. *Atmos. Meas. Tech.*, 6:3169–3180, 2013.

Fauchereau, N., Pohl, B., and Lorrey, A. Extratropical Impacts of the MaddenJulian Oscillation over New Zealand from a Weather Regime Perspective. *Journal of Climate*, 29(6):2161–2175, 2016. doi: 10.1175/JCLI-D-15-0152.1.

Fjeldbo, G., Kliore, A. J., and Eshleman, V. R. The Neutral Atmosphere of Venus as Studied with the Mariner V Radio Occultation Experiments. *Astronomical Journal*, 76:123–140, 1971. doi: 10.1086/111096.

Fleming, E. L., Chandra, S., Barnett, J. J., and Corney, M. Zonal mean temperature, pressure, zonal wind, and geopotential height as functions of latitude, COSPAR International Reference Atmosphere: 1986, Part II: Middle Atmosphere Models. *Adv. Space Res.*, 10(12):11–59, 1990.

Forbes, J. M. *Tidal and Planetary Waves*, pages 67–87. American Geophysical Union, 1995. ISBN 9781118664247. doi: 10.1029/GM087p0067.

Fovell, R., Durran, D., and Holton, J. R. Numerical Simulations of Convectively Generated Stratospheric Gravity Waves. *J. Atmos. Sci.*, 49:1427–1442, 1992. doi: 10.1175/1520-0469(1992)049.

France, J. A., Harvey, V. L., Alexander, M. J., Randall, C. E., and Gille, J. C. High Resolution Dynamics Limb Sounder observations of the gravity wave-driven elevated stratopause in 2006. *Journal of Geophysical Research: Atmospheres*, 117 (D20), 2012. doi: 10.1029/2012JD017958.

Fritts, D. C. and Alexander, M. J. Gravity wave dynamics and effects in the middle atmosphere. *Reviews of Geophysics*, 41(1), 2003. doi: 10.1029/2001RG000106.

Fritts, D. C. and Rastogi, P. K. Convective and dynamical instabilities due to gravity wave motions in the lower and middle atmosphere: Theory and observations. *Radio Science*, 20(6):1247–1277, 1985. doi: 10.1029/RS020i006p01247.

Fritts, D. C. and Vincent, R. A. Mesospheric momentum flux studies at Adelaide, Australia: Observations and a gravity wave-tidal interaction model. *J. Atmos. Sci.*, 44(3):605–619, 1982.

Fritts, D. C., Janches, D, and Hocking, W. K. Southern Argentina Agile Meteor Radar: Initial assessment of gravity wave momentum fluxes. *Journal of Geophysical Research: Atmospheres*, 115(D19123), 2010.

Fritts, D. C., Janches, D., Hocking, W. K., Mitchell, N. J., and Taylor, M. J. Assessment of gravity wave momentum flux measurement capabilities by meteor radars having different transmitter power and antenna configurations. *Journal of Geophysical Research: Atmospheres*, 117(D10), 2012.

Garcia, R. R. and Sassi, F. Modulation of the mesospheric semiannual oscillation by the quasi-biennial oscillation. *Earth Planets Space*, 51:563–569, 1999.

Garcia, R. R. and Solomon, S. A numerical model of the zonally averaged dynamical and chemical structure of the middle atmosphere. *Journal of Geophysical Research: Oceans*, 88(C2):1379–1400, 1983. doi: 10.1029/JC088iC02p01379.

Garcia, R. R., Dunkerton, T. J., Lieberman, R. S., and Vincent, R. A. Climatology of the semiannual oscillation of the tropical middle atmosphere. *Journal of Geophysical Research: Atmospheres*, 102(D22):26019–26032, 1997.

Gardner, C. S., Gulati, K., Zhao, Y., and Swenson, G. Measuring gravity wave momentum fluxes with airglow imagers. *Journal of Geophysical Research: Atmospheres*, 104(D10):11903–11915, 1999. doi: 10.1029/1999JD900105.

Garfinkel, C. I., Benedict, J. J., and Maloney, E. D. Impact of the MJO on the boreal winter extratropical circulation. *Geophysical Research Letters*, 41(16):6055–6062, 2014. doi: 10.1002/2014GL061094.

Geller, M. A. *Progress in Solar-Terrestrial Physics: Fifth International Symposium held at Ottawa, Canada, May 1982*, chapter Dynamics of the Middle Atmosphere, pages 359–375. Springer Netherlands, Dordrecht, 1983. ISBN 978-94-009-7096-0. doi: 10.1007/978-94-009-7096-0_28.

Gong, S., Yang, G., Dou, X., Xu, J., Chen, C., and Gong, S. Statistical study of atmospheric gravity waves in the mesopause region observed by a lidar chain in eastern China. *Journal of Geophysical Research: Atmospheres*, 120(15):7619–7634, 2015. doi: 10.1002/2014JD022673.

Greenhow, J. S. and Neufeld, E. L. Winds in the upper atmosphere. *Quarterly Journal of the Royal Meteorological Society*, 87(374):472–489, 1961. doi: 10.1002/qj.49708737403.

Hagan, M. E. and Forbes, J. M. Migrating and nonmigrating semidiurnal tides in the upper atmosphere excited by tropospheric latent heat release. *Journal of Geophysical Research: Space Physics*, 108(A2), 2003. doi: 10.1029/2002JA009466.

Hajj, G. A., Ao, C. O., Iijima, B. A., Kuang, D., Kursinski, E. R., Mannucci, A. J., Meehan, T. K., Romans, L. J., de la Torre Juarez, M., and Yunck, T. P. CHAMP and SAC-C atmospheric occultation results and intercomparisons. *Journal of Geophysical Research: Atmospheres*, 109(D6), 2004. doi: 10.1029/2003JD003909.

Hamilton, K., Vincent, R. A., and May, P. T. Darwin Area Wave Experiment (DAWEX) field campaign to study gravity wave generation and propagation. *J. Geophys. Res.*, 109:D20S01, 2004.

Hecht, J. H., Kovalam, S., May, P. T., Mills, G., Vincent, R. A., Walterscheid, R. L., and Woithe, J. Airglow imager observations of atmospheric gravity waves at Alice Springs and Adelaide, Australia during the Darwin Area Wave Experiment (DAWEX). *Journal of Geophysical Research: Atmospheres*, 109(D20), 2004. doi: 10.1029/2004JD004697.

Hendon, H. H. and Liebmann, B. The Intraseasonal (30–50 day) Oscillation of the Australian Summer Monsoon. *Journal of the Atmospheric Sciences*, 47(24):2909–2924, 1990. doi: 10.1175/1520-0469(1990)047⟨2909:TIDOOT⟩2.0.CO;2.

Hendon, H. H., Wheeler, M. C., and Zhang, C. Seasonal Dependence of the MJO-ENSO Relationship. *Journal of Climate*, 20(3):531–543, 2007. doi: 10.1175/JCLI4003.1.

Hertzog, A., Souprayen, C., and Hauchecorne, A. Observation and backward trajectory of an inertio-gravity wave in the lower stratosphere. *Annales Geophysicae*, 19 (9):1141–1155, 2001. doi: 10.5194/angeo-19-1141-2001.

Hertzog, A., Boccara, G., Vincent, R. A., Vial, F., and Cocquerez, P. Estimation of gravity wave momentum flux and phase speeds from quasi-lagrangian stratospheric balloon flights. part ii: results from the vorcore campaign in antarctica. *J. Atmos. Sci.*, 65, 2008. doi: 10.1175/2008JAS2710.1.

Hertzog, A., Alexander, M. J., and Plougonven, R. On the Intermittency of Gravity Wave Momentum Flux in the Stratosphere. *Journal of the Atmospheric Sciences*, 69(11):3433–3448, 2012. doi: 10.1175/JAS-D-12-09.1.

Hibbins, R. E., Espy, P. J., Jarvis, M. J., Riggin, D. M., and Fritts, D. C. A climatology of tides and gravity wave variance in the MLT above Rothera, Antarctica obtained by MF radar. *Journal of Atmospheric and Solar-Terrestrial Physics*, 69 (45):578–588, 2007. doi: 10.1016/j.jastp.2006.10.009.

Hindley, N. P., Wright, C. J., Smith, N. D., and Mitchell, N. J. The southern stratospheric gravity wave hot spot: individual waves and their momentum fluxes measured by COSMIC GPS-RO. *Atmos. Chem. Phys.*, 15:7797–7818, 2015.

Hines, C. O. Internal Atmospheric Gravity Waves at Ionospheric Heights. *Canadian Journal of Physics*, 38(11):1441–1481, 1960. doi: 10.1139/p60-150.

Hines, C. O. Gravity Waves in the Atmosphere. *Nature*, 239:73–78, 1972. doi: 10.1038/239073a0.

Hines, C. O. *The upper atmosphere in motion: a selection of papers with annotation.* Geophysical monograph. American Geophysical Union, 1974. ISBN 9780875900186.

Hirota, I. Equatorial Waves in the Upper Stratosphere and Mesosphere in Relation to the Semiannual Oscillation of the Zonal Wind. *Journal of the Atmospheric Sciences*, 35(4):714–722, 1978. doi: 10.1175/1520-0469(1978)035⟨0714:EWITUS⟩2.0.CO;2.

Hirota, I. Observational evidence of the semiannual oscillation in the tropical middle atmosphere—A review. *Pure and Applied Geophysics*, 118(1):217–238, 1980. doi: 10.1007/BF01586452.

Hitchman, M. H. and Leovy, C. B. Estimation of the Kelvin wave contribution to the semiannual oscillation. *J. Atmos. Sci.*, 45:1462–1475, 1988.

Hocking, W. K. A new approach to momentum flux determinations using SKiYMET meteor radars. *Annales Geophysicae*, 23(7):2433–2439, 2005. doi: 10.5194/angeo-23-2433-2005.

Hocking, W. K., Fuller, B., and Vandepeer, B. Real-time determination of meteor-related parameters utilizing modern digital technology. *Journal of Atmospheric and Solar-Terrestrial Physics*, 63(2–3):155–169, 2001. doi: 10.1016/S1364-6826(00)00138-3.

Hoell, A., Barlow, M., Wheeler, M. C., and Funk, C. Disruptions of El NiñoSouthern Oscillation Teleconnections by the MaddenJulian Oscillation. *Geophysical Research Letters*, 41(3):998–1004, 2014. doi: 10.1002/2013GL058648.

Hoffmann, L. and Alexander, M. J. Retrieval of stratospheric temperatures from Atmospheric Infrared Sounder radiance measurements for gravity wave studies. *Journal of Geophysical Research: Atmospheres*, 114(D7), 2009. doi: 10.1029/2008JD011241.

Hoffmann, L., Alexander, M. J., Clerbaux, C., Grimsdell, A. W., Meyer, C. I., Rößler, T., and Tournier, B. Intercomparison of stratospheric gravity wave observations with AIRS and IASI. *Atmospheric Measurement Techniques*, 7(12):4517–4537, 2014. doi: 10.5194/amt-7-4517-2014.

Holton, J. R. *An Introduction to Dynamic Meteorology*. Academic Press Inc., 2nd edition, 1979.

Holton, J. R. The influence of gravity wave breaking on the general circulation of the middle atmosphere. *J. Atmos. Sci.*, 40:2497–2507, 1983.

Holton, J. R., Alexander, M. J., and Boehm, M. T. Evidence for short vertical wavelength Kelvin waves in the Department of Energy-Atmospheric Radiation Measurement Nauru99 radiosonde data. *Journal of Geophysical Research: Atmospheres*, 106(D17):20125–20129, 2001. doi: 10.1029/2001JD900108.

Horinouchi, T. A numerical study of upward-propagating gravity waves in two different MJO phases. *Geophysical Research Letters*, 35(17), 2008. doi: 10.1029/2008GL034992.

Houghton, J. T. *The Physics of Atmospheres*. Cambridge University Press, 1977.

Huang, F. T., Mayr, H., Reber, C. A., Russell III, J. M., Mlynczak, M. G., and Mengel, J. G. Ozone quasi-biennial oscillations (QBO), semiannual oscillations (SAO), and correlations with temperature in the mesosphere, lower thermosphere, and stratosphere, based on measurements from SABER on TIMED and MLS on UARS. *Annales Geophysicae*, 113(15), 2008.

Huffman, G. J., Adler, R. F., Bolvin, D. T., Gu, G., Nelkin, E. J., Bowman, K. P., Hong, Y., Stocker, E. F., and B., Wolff D. The TRMM Multi-satellite Precipitation Analysis: Quasi-Global, Multi-Year, Combined-Sensor Precipitation Estimates at Fine Scale. *J. Hydrometeor.*, 8:38–35, 2007.

Hughes, D. W. The World's Most Famous Meteor Shower Picture. *Earth Moon and Planets*, 68:311–322, 1995. doi: 10.1007/BF00671522.

Isoda, F., Tsuda, T., Nakamura, T., Vincent, R. A., Reid, I. M., Achmad, E., Sadewo, A., and Nuryanto, A. Intraseasonal oscillations of the zonal wind near the mesopause observed with medium-frequency and meteor radars in the tropics. *Journal of Geophysical Research: Atmospheres*, 109(D21), 2004. doi: 10.1029/2003JD003378.

Jiang, X., Waliser, D. E., Xavier, P. K., Petch, J., Klingaman, N. P., Woolnough, S. J., Guan, B., Bellon, G., Crueger, T., DeMott, C., Hannay, C., Lin, H., Hu, W., Kim, D., Lappen, C-L., Lu, M-M., Ma, H-Y., Miyakawa, T., Ridout, J. A., Schubert, S. D., Scinocca, J., Seo, K-H., Shindo, E., Song, X., Stan, C., Tseng, W-L., Wang, W., Wu, T., Wu, X., Wyser, K., Zhang, G. J., and Zhu, H. Vertical structure and physical processes of the Madden-Julian oscillation: Exploring key model physics in climate simulations. *Journal of Geophysical Research: Atmospheres*, 120(10): 4718–4748, 2015. doi: 10.1002/2014JD022375.

Karlsson, B., Körnich, H., and Gumbel, J. Evidence for interhemispheric stratosphere-mesosphere coupling derived from noctilucent cloud properties. *Geophysical Research Letters*, 34(16), 2007. doi: 10.1029/2007GL030282.

Karoly, D. J., Roff, G. L., and Reeder, M. J. Gravity wave activity associated with tropical convection detected in TOGA COARE sounding data. *Geophysical Research Letters*, 23(3):261–264, 1996.

Khouider, B., St-Cyr, A., Majda, A. J., and Tribbia, J. The MJO and Convectively Coupled Waves in a Coarse-Resolution GCM with a Simple Multicloud Parameterization. *Journal of Atmospheric Sciences*, 68(2):240–264, 2011.

Kiladis, G. N., Wheeler, M. C., Haertel, P. T., Straub, K. H., and Roundy, P E. Convectively coupled equatorial waves. *Reviews of Geophysics*, 47(2), 2009. doi: 10.1029/2008RG000266.

Kinoshita, T., Murayama, Y., and Kawamura, S. Tidal modulations of mesospheric gravity wave kinetic energy observed with MF radar at Poker Flat Research Range, Alaska. *Journal of Geophysical Research: Atmospheres*, 120(13):6379–6390, 2015. doi: 10.1002/2014JD022647.

Kirkwood, S., Barabash, V., Brändström, B. U. E., Moström, A., Stebel, K., Mitchell, N., and Hocking, W. Noctilucent clouds, PMSE and 5-day planetary waves: A case study. *Geophysical Research Letters*, 29(10):50–1–50–4, 2002. doi: 10.1029/2001GL014022.

Kovalam, S., Vincent, R. A., and Love, P. Gravity waves in the equatorial MLT region. *Journal of Atmsopheric and Solar-Terrestrial Physics*, 68:266–282, 2006.

Kumar, K. K., Swain, D., John, S. R., and Ramkumar, G. Simultaneous observations of SAO and QBO in winds, temperature and ozone in the tropical middle atmosphere over Thumba (8.5 N, 77 E). *Clim. Dynam.*, 37:1961–1973, 2011.

Kursinski, E. R., Hajj, G. A., Schofield, J. T., Linfield, R. P., and Hardy, K. R. Observing Earth's atmosphere with radio occultation measurements using the Global Positioning System. *Journal of Geophysical Research: Atmospheres*, 102(D19):23429–23465, 1997. doi: 10.1029/97JD01569.

Lieberman, R. S. and Hays, P. B. An estimate of the momentum deposition in the lower thermosphere by the observed diurnal tide. *J. Atmos. Sci.*, 51:3094–3105, 1994.

Liebmann, B. and Hartmann, D. L. An Observational Study of Tropical-Midlatitude Interaction on Intraseasonal Time Scales during Winter. *Journal of the Atmospheric Sciences*, 41(23):3333–3350, 1984. doi: 10.1175/1520-0469(1984)041⟨3333:AOSOTI⟩2.0.CO;2.

Liebmann, B. and Smith, C. A. Description of a Complete (Interpolated) Outgoing Longwave Radiation Dataset. *Bulletin of the American Meteorological Society*, 77: 1275–1277, 1996.

Lindzen, R. S. Turbulence and stress owing to gravity wave and tidal breakdown. *J. Geophys. Res.*, 86(C10):9707–9714, 1981. doi: 10.1029/JC086iC10p09707.

Liou, Y.-A., Pavelyev, A. G., Liu, S.-F., Pavelyev, A. A., Yen, N., Huang, C.-Y., and Fong, C.-J. FORMOSAT-3/COSMIC GPS Radio Occultation Mission: Preliminary Results. *Geoscience and Remote Sensing, IEEE Transactions on*, 45(11): 3813–3826, 2007. doi: 10.1109/TGRS.2007.903365.

London, J. Radiative Energy Sources and Sinks in the Stratosphere and Mesosphere. In Nicolet, M. and Aikin, A. C., editors, *Atmospheric Ozone and its Variation and Human Influences*, page 703, 1980.

Lorenz, D. J. and Hartmann, D. L. The Effect of the MJO on the North American Monsoon. *Journal of Climate*, 19(3):333–343, 2006. doi: 10.1175/JCLI3684.1.

Lott, F. and Guez, L. A stochastic parameterization of the gravity waves due to convection and its impact on the equatorial stratosphere. *Journal of Geophysical Research: Atmospheres*, 118(16):8897–8909, 2013. doi: 10.1002/jgrd.50705.

Lu, X., Liu, A. Z., Swenson, G. R., Li, T., Leblanc, T., and McDermid, I. S. Gravity wave propagation and dissipation from the stratosphere to the lower thermosphere. *Journal of Geophysical Research: Atmospheres*, 114(D11), 2009. doi: 10.1029/2008JD010112.

Lue, H. Y., Kuo, F. S., Fukao, S., and Nakamura, T. Studies of gravity wave propagation in the mesosphere observed by MU radar. *Annales Geophysicae*, 31(5): 845–858, 2013. doi: 10.5194/angeo-31-845-2013.

Lynch, A. H. and Cassano, J. J. *Applied Atmospheric Dynamics*. Wiley, 2006.

Madden, R. A. and Julian, P. R. Description of Global-Scale Circulation Cells in the Tropics with a 40-50 Day Period. *J. Atmos. Sci.*, 29(6):1109–1123, 1972. doi: 10.1175/1520-0469(1972)029.

Madden, R. A. and Julian, P. R. Observations of the 40–50-Day Tropical Oscillation – A Review. *Monthly Weather Review*, 122(5):814–837, 1994. doi: 10.1175/1520-0493(1994)122⟨0814:OOTDTO⟩2.0.CO;2.

Manson, A. H. and Meek, C. E. Gravity Wave Propagation Characteristics (60–120 km) as Determined by the Saskatoon MF Radar (Gravnet) System: 1983–85 at 52° N, 107° W. *Journal of the Atmospheric Sciences*, 45(6):932–946, 1988. doi: 10.1175/1520-0469(1988)045⟨0932:GWPCKA⟩2.0.CO;2.

Manson, A. H., Meek, C. E., and Hall, G. E. Correlations of gravity waves and tides in the mesosphere over Saskatoon. *Journal of Atmospheric and Solar-Terrestrial Physics*, 60(11):1089–1107, 1998. doi: 10.1016/S1364-6826(98)00059-5.

Marquardt, C. and Healy, S. Measurement noise and stratospheric gravity wave characteristics obtained from GPS occultation data. *J. Meteorol. Soc. Japan*, 83: 417–428, 2005.

Matsuno, T. Quasi-Geostrophic Motions in the Equatorial Area. *Journal of the Meteorological Society of Japan. Ser. II*, 44(1):25–43, 1966.

Matthews, A. J. Propagation mechanisms for the Madden-Julian Oscillation. *Quart. J. Roy. Meteorol. Soc.*, 126:2637–2652, 2000.

Matthews, A. J., Slingo, J. M., Hoskins, B. J., and Inness, P. M. Fast and slow Kelvin waves in the Madden-Julian oscillation of a GCM. *Quarterly Journal of the Royal Meteorological Society*, 125(557):1473–1498, 1999. doi: 10.1002/qj.49712555702.

McCrea, I., Aikio, A., Alfonsi, L., Belova, E., Buchert, S., Clilverd, M., Engler, N., Gustavsson, B., Heinselman, C., Kero, J., Kosch, M., Lamy, H., Leyser, T., Ogawa, Y., Oksavik, K., Pellinen-Wannberg, A., Pitout, F., Rapp, M., Stanislawska, I., and Vierinen, J. The science case for the EISCAT_3D radar. *Progress in Earth and Planetary Science*, 2(1):1–63, 2015. doi: 10.1186/s40645-015-0051-8.

McDonald, A. J. Gravity wave occurrence statistics derived from paired COSMIC/FORMOSAT3 observations. *Journal of Geophysical Research: Atmospheres*, 117(D15), 2012. doi: 10.1029/2011JD016715.

McKinley, D. W. R. *Meteor science and engineering.* New York, McGraw-Hill, 1961.

McLandress, C. On the importance of gravity waves in the middle atmosphere and their parameterization in general circulation models. *Journal of Atmospheric and Solar-Terrestrial Physics*, 60(14):1357–1383, 1998. doi: 10.1016/S1364-6826(98)00061-3.

Mitchell, N. J. and Howells, V. St. C. Vertical velocities associated with gravity waves measured in the mesosphere and lower thermosphere with the EISCAT VHF radar. *Annales Geophysicae*, 16(10):1367–1379, 1998. doi: 10.1007/s00585-998-1367-0.

Mitchell, N. J., Thomas, L., and Prichard, I. T. Gravity waves in the stratosphere and troposphere observed by lidar and MST radar. *Journal of Atmospheric and Terrestrial Physics*, 56(8):939–947, 1994. doi: 10.1016/0021-9169(94)90155-4.

Moffat-Griffin, T., Hibbins, R. E., Jarvis, M. J., and Colwell, S. R. Seasonal variations of gravity wave activity in the lower stratosphere over an Antarctic Peninsula station. *Journal of Geophysical Research: Atmospheres*, 116(D14), 2011. doi: 10.1029/2010JD015349. D14111.

Moffat-Griffin, T., Jarvis, M. J., Colwell, S. R., Kavanagh, A. J., Manney, G. L., and Daffer, W. H. Seasonal variations in lower stratospheric gravity wave energy above the Falkland Islands. *Journal of Geophysical Research: Atmospheres*, 118 (19):10,861–10,869, 2013. doi: 10.1002/jgrd.50859.

Morita, J., Takayabu, Y. N., Shige, S., and Kodama, Y. Analysis of rainfall characteristics of the Madden–Julian oscillation using TRMM satellite data. *Dynamics of Atmospheres and Oceans*, 42(1–4):107–126, 2006.

Moss, A. C., Wright, C. J., Davis, R. N., and Mitchell, N. J. Gravity-wave momentum fluxes in the mesosphere over Ascension Island (8° S, 14° W) and the anomalous zonal winds of the semi-annual oscillation in 2002. *Annales Geophysicae*, 34(2): 323–330, 2016a. doi: 10.5194/angeo-34-323-2016.

Moss, A. C., Wright, C. J., and Mitchell, N. J. Does the Madden-Julian Oscillation Modulate Stratospheric Gravity Waves? *Geophysical Research Letters*, 43:3973–3981, 2016b. doi: 10.1002/2016GL068498.

Murgatroyd, R. J. and Singleton, F. Possible meridional circulations in the stratosphere and mesosphere. *Quarterly Journal of the Royal Meteorological Society*, 87 (372):125–135, 1961. doi: 10.1002/qj.49708737202.

Nakamura, T., Tsuda, T., Fukao, S., Manson, A. H., Meek, C. E., Vincent, R. A., and Reid, I. M. Mesospheric gravity waves at Saskatoon (52° N), Kyoto (35° N), and Adelaide (35° S). *Journal of Geophysical Research: Atmospheres*, 101(D3): 7005–7012, 1996. doi: 10.1029/95JD03826.

Nappo, C.J. *An Introduction to Atmospheric Gravity Waves*. International geophysics series. Academic Press/Elsevier, 2013. ISBN 9780123852236.

Nesbitt, S. W. and Zipser, E. J. The Diurnal Cycle of Rainfall and Convective Intensity according to Three Years of TRMM Measurements. *Journal of Climate*, 16 (10):1456–1475, 2003. doi: 10.1175/1520-0442(2003)016⟨1456:TDCORA⟩2.0.CO;2.

Nygrén, T., Aikio, A. T., Voiculescu, M., and Cai, L. Radar observations of simultaneous traveling ionospheric disturbances and atmospheric gravity waves. *Journal of Geophysical Research: Space Physics*, 120(5):3949–3960, 2015. doi: 10.1002/2014JA020794.

Pancheva, D., Mitchell, N. J., and Younger, P. T. Meteor radar observations of atmospheric waves in the equatorial mesosphere/lower thermosphere over Ascension Island. *Annales Geophysicae*, 22(2):387–404, 2004. doi: 10.5194/angeo-22-387-2004.

Pandya, R. E. and Alexander, M. J. Linear Stratospheric Gravity Waves above Convective Thermal Forcing. *J. Atmos. Sci.*, 56:2434–2446, 1999. doi: 10.1175/1520-0469(1999)056.

Peña Ortiz, C., Schmidt, H., Giorgetta, M. A., and Keller, M. QBO modulation of the semiannual oscillation in MAECHAM5 and HAMMONIA. *J. Geophys. Res.: Atmospheres*, 115(D21), 2010.

Placke, M., Hoffmann, P., Latteck, R., and Rapp, M. Gravity wave momentum fluxes from MF and meteor radar measurements in the polar MLT region. *J. Geophys. Res.: Space Physics*, 120(1), 2015.

Preusse, P., Ern, M., Eckermann, S. D., Warner, C. D., Picard, R. H., Knieling, P., Krebsbach, M., Russell III, J. M., Mlynczak, M. G., Mertens, C. J., and Riese, M. Tropopause to mesopause gravity waves in August: Measurement and modeling. *Journal of Atmospheric and Solar-Terrestrial Physics*, 68(15):1730–1751, 2006. doi: 10.1016/j.jastp.2005.10.019.

Preusse, P., Eckermann, S. D., Ern, M., Oberheide, J., Picard, R. H., Roble, R. G., Riese, M., Russell, J. M., and Mlynczak, M. G. Global ray tracing simulations of the SABER gravity wave climatology. *Journal of Geophysical Research: Atmospheres*, 114(D8), 2009. doi: 10.1029/2008JD011214.

Randall, C. E. *spaceweather.com: Noctilucent Clouds, Behaving Strangely:*, 2015. URL `http://spaceweather.com/archive.php?view=1&day=01&month=03&year=2015`. Published online on 01/03/2015; Accessed 28/03/2016.

Rao, R. K., Gurubaran, S., Sathiskumar, S., Sridharan, S., Nakamura, T., Tsuda, T., Takahashi, H., Batista, P. P., Clemesha, B. R., Buriti, R. A., Pancheva, D. V., and Mitchell, N. J. Longitudinal variability in intraseasonal oscillation in the tropical mesosphere and lower thermosphere region. *J. Geophys. Res.-Atmos.*, 114:D19110, 2009.

Rao, V. N., Shibagaki, Y., and Tsuda, T. Diurnal variation of short-period (20–120 min) gravity waves in the equatorial Mesosphere and Lower Thermosphere and its relation to deep tropical convection. *Annales Geophysicae*, 29(4):623–629, 2011. doi: 10.5194/angeo-29-623-2011.

Ratnam, M. V., Babu, A. N., Rao, V. V. M. J., Rao, S. V. B., and Rao, D. N. MST radar and radiosonde observations of inertia-gravity wave climatology over tropical stations: Source mechanisms. *Journal of Geophysical Research: Atmospheres*, 113 (D7), 2008a. doi: 10.1029/2007JD008986.

Ratnam, M. V., Kumar, G. K., Murthy, B. V. K., Patra, A. K., Rao, V. V. M. J., Rao, S. V. B., Kumar, K. K., and Ramkumar, G. Long-term variability of the low latitude mesospheric SAO and QBO and their relation with stratospheric QBO. *Geophys. Res. Lett.*, 35(5), 2008b.

Rauthe, M., Gerding, M., Höffner, J., and Lübken, F-J. Lidar temperature measurements of gravity waves over Khlungsborn (54N) from 1 to 105 km: A winter-summer comparison. *Journal of Geophysical Research: Atmospheres*, 111(D24), 2006. doi: 10.1029/2006JD007354.

Reid, I. M. and Vincent, R. A. Measurements of mesospheric gravity wave momentum fluxes and mean flow accelerations at Adelaide, Australia. *Journal of Atmospheric and Terrestrial Physics*, 49(5):443–460, 1987. doi: 10.1016/0021-9169(87)90039-0.

Richter, J. H. and Garcia, R. R. On the forcing of the Mesospheric Semi-Annual Oscillation in the Whole Atmosphere Community Climate Model. *Geophys. Res. Lett.*, 33, 2006.

Riggin, D. M., Fritts, D. C., Fawcett, C. D., Kudeki, E., and Hitchman, M. H. Radar observations of gravity waves over Jicamarca, Peru, during the CADRE campaign. *Journal of Geophysical Research: Atmospheres*, 102(D22):26263–26281, 1997. doi: 10.1029/96JD03675.

Rocken, C., Kuo, Y. H., Schreiner, W. S., Hunt, D., Sokolovskiy, S., and C., McCormick. COSMIC system description. *Terrestrial Atmospheric and Oceanic Sciences*, 11:21–52, 2000.

Rocken, C., Kuo, Y. H., Sokolovskiy, S. V., and Anthes, R. A. The ROCSAT-3/COSMIC mission and applications of GPS radio occultation data to weather and climate. *Proc. SPIE*, 5661:1–12, 2004. doi: 10.1117/12.566544.

Roscoe, H. K. The Brewer-Dobson circulation in the stratosphere and mesosphere: Is there a trend? *Advances in Space Research*, 38(11):2446–2451, 2006. doi: 10.1016/j.asr.2006.02.078.

Salby, M. L., Garcia, R. R., and Hendon, H. H. Planetary-Scale Circulations in the Presence of Climatological and Wave-Induced Heating. *Journal of Atmospheric Sciences*, 51(16):2344–2367, 1994.

Sandford, D. J. and Mitchell, N. J. Lunar tides in the Mesosphere over Ascension Island (8° S, 14.4° W). *Annales Geophysicae*, 25(1):9–12, 2007. doi: 10.5194/angeo-25-9-2007.

Sandford, D. J., Mitchell, N. J., Vincent, R. A., and Murphy, R. A. The lunar tides in the Antarctic mesosphere and lower thermosphere. *Journal of Atmospheric and Solar-Terrestrial Physics*, 69(17–18):2219–2237, 2007. doi: 10.1016/j.jastp.2007.04.010.

Sato, K., O'Sullivan, D., and Dunkerton, T. J. Low-frequency inertia-gravity waves in the stratosphere revealed by three- week continuous observation with the MU radar. *Geophys. Res. Lett.*, 24:1739–1742, 1997.

Sato, K., Tsutsumi, M., Sato, T., Nakamura, T., Saito, A., Tomikawa, Y., Nishimura, K., Kohma, M., Yamagishi, H., and Yamanouchi, T. Program of the Antarctic Syowa MST/IS radar (PANSY): Part A - Recent progress from networked studies based around MST radar. *Journal of Atmospheric and Solar-Terrestrial Physics*, 118,:2–15, 2014. doi: 10.1016/j.jastp.2013.08.022.

Schreiner, W., Rocken, C., Sokolovskiy, S., Syndergaard, S., and Hunt, D. Estimates of the precision of GPS radio occultations from the COSMIC/FORMOSAT-3 mission. *Geophysical Research Letters*, 34(4), 2007. doi: 10.1029/2006GL027557.

Serra, Y. L., Jiang, X., Tian, B., Amador-Astua, J., Maloney, E. D, and Kiladis, G. N. Tropical Intraseasonal Modes of the Atmosphere. *Annual Review of Environment and Resources*, 39(1):189–215, 2014. doi: 10.1146/annurev-environ-020413-134219.

Siskind, D. E. and McCormack, J. P. Summer mesospheric warmings and the quasi 2 day wave. *Geophysical Research Letters*, 41(2):717–722, 2014. doi: 10.1002/2013GL058875.

Smith, A. K. MIDDLE ATMOSPHERE — Planetary Waves. In Editor-in Chief: Holton, J. R., editor, *Encyclopedia of Atmospheric Sciences*, pages 1314–1321. Academic Press, Oxford, 2003. ISBN 978-0-12-227090-1. doi: 10.1016/B0-12-227090-8/00229-3.

Sperber, K. R. Propagation and the Vertical Structure of the Madden-Julian Oscillation. *Monthly Weather Review*, 131:3018–3037, 2003.

Sperber, K. R., Brankovic, C., Déqué, M., Frederiksen, C. S., Graham, R., Kitoh, A., Kobayashi, C., Palmer, T., Puri, K., Tennant, W., and Volodin, E. Dynamical Seasonal Predictability of the Asian Summer Monsoon. *Monthly Weather Review*, 129(9):2226–2248, 2001. doi: 10.1175/1520-0493(2001)129⟨2226:DSPOTA⟩2.0.CO;2.

Stockwell, R. G. Why use the S-transform? *Pseudo-differential Operators: Partial Differential Equations and Time-Frequency Analysis*, 52:279–307, 2007.

Stockwell, R. G., Mansinha, L., and Lowe, R. P. Localization of the Complex Spectrum: The S Transform. *IEEE Transactions on Signal Processing*, 44(4):998–1001, 1996.

Suzuki, S., Shiokawa, K., Otsuka, Y., Kawamura, S., and Murayama, Y. Evidence of gravity wave ducting in the mesopause region from airglow network observations. *Geophysical Research Letters*, 40(3):601–605, 2013. doi: 10.1029/2012GL054605.

Takahashi, H., Taylor, M. J., Pautet, P.-D., Medeiros, A. F., Gobbi, D., Wrasse, C. M., Fechine, J., Abdu, M. A., Batista, I. S., Paula, E., Sobral, J. H. A., Arruda, D., Vadas, S. L., Sabbas, F. S., and Fritts, D. C. Simultaneous observation of ionospheric plasma bubbles and mesospheric gravity waves during the SpreadFEx Campaign. *Annales Geophysicae*, 27(4):1477–1487, 2009. doi: 10.5194/angeo-27-1477-2009.

Tang, Y. and Yu, B. MJO and its relationship to ENSO. *Journal of Geophysical Research: Atmospheres*, 113(D14), 2008. doi: 10.1029/2007JD009230.

Thompson, R. O. R. Y. Observation of inertial waves in the stratosphere. *Quarterly Journal of the Royal Meteorological Society*, 104(441):691–698, 1978. doi: 10.1002/qj.49710444111.

Thorsen, D., Franke, S. J., and Kudeki, E. A new approach to MF radar interferometry for estimating mean winds and momentum flux. *Radio Science*, 32(2):707–726, 1997. doi: 10.1029/96RS03422.

Thurairajah, B., Bailey, S. M., Nielsen, K., Randall, C. E., Lumpe, J. D., Taylor, M. J., and Russell III, J. M. Morphology of polar mesospheric clouds as seen from space. *Journal of Atmospheric and Solar-Terrestrial Physics*, 104:234–243, 2013. doi: 10.1016/j.jastp.2012.09.009.

Tsuda, T. Characteristics of atmospheric gravity waves observed using the MU (Middle and Upper atmosphere) radar and GPS (Global Positioning System) radio occultation. *Proceedings of the Japan Academy, Series B*, 90(1):12–27, 2014. doi: 10.2183/pjab.90.12.

Tsuda, T., Nishida, M., Rocken, C., and Ware, R. H. A Global Morphology of Gravity Wave Activity in the Stratosphere Revealed by the GPS Occultation Data (GPS/MET). *Journal of Geophysical Research: Atmospheres*, 105(D6):7257–7273, 2000. doi: 10.1029/1999JD901005.

Tsuda, T., Lin, X., Hayashi, H., and Noersomadi, . Analysis of vertical wave number spectrum of atmospheric gravity waves in the stratosphere using COSMIC GPS radio occultation data. *Atmospheric Measurement Techniques*, 4(8):1627–1636, 2011. doi: 10.5194/amt-4-1627-2011.

Vallis, G. K. *Atmospheric and Oceanic Fluid Dynamics*. Cambridge University Press, Cambridge, U.K., 2006.

Vaughan, G. and Worthington, R. M. Inertia-gravity waves observed by the UK MST radar. *Quarterly Journal of the Royal Meteorological Society*, 133(S2):179–188, 2007. doi: 10.1002/qj.142.

Vincent, R. A. The dynamics of the mesosphere and lower thermosphere: a brief review. *Progress in Earth and Planetary Science*, 2(1):1–13, 2015. doi: 10.1186/s40645-015-0035-8.

Vincent, R. A. and Reid, I. M. Hf doppler measurements of mesospheric gravity wave momentum fluxes. *J. Atmos. Sci.*, 40:1321–1333, 1983. doi: 10.1175/1520-0469(1983)040⟨1321:HDMOMG⟩2.0.CO;2.

Vincent, R. A., Hertzog, A., Boccara, G., and Vial, F. Quasi-Lagrangian superpressure balloon measurements of gravity-wave momentum fluxes in the polar strato-

sphere of both hemispheres. *Geophysical Research Letters*, 34(19):1944–8007, 2007. doi: 10.1029/2007GL031072.

Vincent, R. A., Kovalam, S., Reid, I. M., and Younger, J. P. Gravity wave flux retrievals using meteor radars. *Geophys. Res. Lett.*, 37(14802), 2010.

Vincent, R. A., Alexander, M. J., Dolman, B. K., MacKinnon, A. D., May, P. T., Kovalam, S., and Reid, I. M. Gravity wave generation by convection and momentum deposition in the mesosphere-lower thermosphere. *Journal of Geophysical Research: Atmospheres*, 118(12):6233–6245, 2013. doi: 10.1002/jgrd.50372.

Vlasov, A., Kauristie, K., van de Kamp, M., Luntama, J.-P., and Pogoreltsev, A. A study of Traveling Ionospheric Disturbances and Atmospheric Gravity Waves using EISCAT Svalbard Radar IPY-data. *Annales Geophysicae*, 29(11):2101–2116, 2011. doi: 10.5194/angeo-29-2101-2011.

Wang, L. and Alexander, M. J. Global estimates of gravity wave parameters from GPS radio occultation temperature data. *Journal of Geophysical Research: Atmospheres*, 115(D21), 2010. doi: 10.1029/2010JD013860.

Ware, R., Rocken, C., Solheim, F., Exner, M., Schreiner, W., Anthes, R., Feng, D., Herman, B., Gorbunov, M., Sokolovskiy, S., Hardy, K., Kuo, Y., Zou, X., Trenberth, K., T., Meehan, Melbourne, W., and S., Businger. GPS Sounding of the Atmosphere from Low Earth Orbit: Preliminary Results. *Amer. Meteor. Soc.*, 77:19–40, 1996. doi: 10.1175/1520-0477(1996)077.

Wheeler, M. C. and Hendon, H. H. An All-Season Real-Time Multivariate MJO Index: Development of an Index for Monitoring and Prediction. *Monthly Weather Review*, 132(8):1917–1932, 2004. ISSN 0027-0644. doi: 10.1175/1520-0493(2004)132⟨1917:AARMMI⟩2.0.CO;2.

Wheeler, M. C., Hendon, H. H., Cleland, S., Meinke, H., and Donald, A. Impacts of the Madden-Julian Oscillation on Australian Rainfall and Circulation. *Journal of Climate*, 22(6):1482–1498, 2009. doi: 10.1175/2008JCLI2595.1.

Wickert, J., Reigber, C., Beyerle, G., König, R., Marquardt, C., Schmidt, T., Grunwaldt, L., Galas, R., Meehan, T. K., Melbourne, W. G., and Hocke, K. Atmosphere sounding by GPS radio occultation: First results from CHAMP. *Geophysical Research Letters*, 28(17):3263–3266, 2001. doi: 10.1029/2001GL013117.

Williams, P. J. S., Crowley, G., Schlegel, K., S., Virdi T., McCrea, I., Watkins, G., Wade, N., Hargreaves, J. K., Lachlan-Cope, T., Muller, H., Baldwin, J. E., Warner, P., van Eyken, A. P., Hapgood, M. A., and Rodger, A. S. EISCAT Science The generation and propagation of atmospheric gravity waves observed during the Worldwide Atmospheric Gravity-wave Study (WAGS). *Journal of Atmospheric and Terrestrial Physics*, 50(4):323–338, 1988. doi: 10.1016/0021-9169(88)90018-9.

Wilms, H., Rapp, M., Hoffmann, P., Fiedler, J., and Baumgarten, G. Gravity wave influence on NLC: experimental results from ALOMAR, 69° N. *Atmospheric Chemistry and Physics*, 13(23):11951–11963, 2013. doi: 10.5194/acp-13-11951-2013.

Wright, C. J. and Gille, J. C. HIRDLS observations of gravity wave momentum fluxes over the monsoon regions. *J. Geophys. Res. Atmos.*, 116(D12103), 2011. doi: 10.1029/2011JD015725.

Wright, C. J., Rivas, M. B., and Gille, J. C. Intercomparisons of HIRDLS, COSMIC and SABER for the detection of stratospheric gravity waves. *Atmospheric Measurement Techniques*, 4(8):1581–1591, 2011. doi: 10.5194/amt-4-1581-2011.

Wright, C. J., Scott, R. B., Arbic, B. K., and Furnival, D. F. Bottom dissipation of subinertial currents at the Atlantic zonal boundaries. *Journal of Geophysical Research: Oceans*, 117(C3), 2012. doi: 10.1029/2011JC007702.

Wright, C. J., Osprey, S. M., and Gille, J. C. Global observations of gravity wave intermittency and its impact on the observed momentum flux morphology. *J. Geophys. Res. Atmos.*, 118:10,980–10,993, 2013. doi: 10.1002/jgrd.50869.

Wright, C. J., Hindley, N. P., Moss, A. C., and Mitchell, N. J. Multi-instrument gravity-wave measurements over Tierra del Fuego and the Drake Passage – Part 1: Potential energies and vertical wavelengths from AIRS, COSMIC, HIRDLS, MLS-Aura, SAAMER, SABER and radiosondes. *Atmospheric Measurement Techniques Discussions*, 8(7):6797–6876, 2015. doi: 10.5194/amt-9-877-2016.

Wright, C. J., Hindley, N. P., and Mitchell, N. J. Combining AIRS and MLS observations for three-dimensional gravity wave measurement. *Geophysical Research Letters*, 43(2):884–893, 2016. doi: 10.1002/2015GL067233.

Wu, J. F., Xue, X. H., Hoffmann, L., Dou, X. K., Li, H. M., and Chen, T. D. A case study of typhoon-induced gravity waves and the orographic impacts related to Typhoon Mindulle (2004) over Taiwan. *Journal of Geophysical Research: Atmospheres*, 120(18):9193–9207, 2015. doi: 10.1002/2015JD023517.

Xu, J., Li, Q., Yue, J., Hoffmann, L., Straka, W. C., Wang, C., Liu, M., Yuan, W., Han, S., Miller, S. D., Sun, L., Liu, X., Liu, W., Yang, J., and Ning, B. Concentric gravity waves over northern China observed by an airglow imager network and satellites. *Journal of Geophysical Research: Atmospheres*, 120(21):11,058–11,078, 2015. doi: 10.1002/2015JD023786.

Younger, P. T. and Mitchell, N. J. Waves with period near 3 days in the equatorial mesosphere and lower thermosphere over Ascension Island. *Journal of Atmospheric and Solar-Terrestrial Physics*, 68(3–5):369–378, 2006. doi: 10.1016/j.jastp.2005.05.008.

Yue, J., Hoffmann, L., and Alexander, M. J. Simultaneous observations of convective gravity waves from a ground-based airglow imager and the AIRS satellite experiment. *Journal of Geophysical Research: Atmospheres*, 118(8):3178–3191, 2013. doi: 10.1002/jgrd.50341.

Yunck, T. P., Lindaland, G. F., and Liu, C. H. The role of GPS in precise Earth observation. *paper presented at the Position Location and Navigation Symposium. Record. Navigation into the 21st Century. IEEE PLANS '88., IEEE*, 1988. doi: 10.1109/PLANS.1988.195491.

Zhang, C. Madden-Julian Oscillation. *Reviews of Geophysics*, 43(2004):1–36, 2005. doi: 10.1029/2004RG000158.